

HIGH-PERFORMANCE OPTIMIZATION METHODS FOR EMERGING
POWER SYSTEMS

by

TUNCAY ALTUN

DISSERTATION

Submitted in partial fulfillment of the requirements
for the degree of Doctor of Philosophy at
The University of Texas at Arlington
August, 2020

Arlington, Texas

Supervising Committee:

Ali Davoudi, Supervising Professor

Ramtin Madani, Supervising Professor

Rasool Kenarangui

Jonathan Bredow

David Levine

Copyright by
TUNCAY ALTUN
2020

ACKNOWLEDGEMENTS

I deeply thank my graduate advisors, Dr. Ali Davoudi and Dr. Ramtin Madani, for teachings, guidance and the motivation they provided me during all these years. Dr. Davoudi deserves special thanks for his invaluable support whenever I need. I also want to thank the members of my dissertation committee, Dr. Rasool Kenarangui, Dr. Jonathan Bredow and Dr. David Levine, for their insightful comments that help to improve my research.

With my whole heart I thank all of my friends and collaborators at UTA. I must thank my valuable colleagues Ajay Yadav, Deepak Pullaguram, Shan Zuo for their supports during my educations.

I would also like to extend my appreciation to Republic of Turkey Ministry of National Education for their financial support during my PhD studies. Additionally, this work was supported in part by the U.S. Department of Energy Research under grant DE-AR0001086, and the National Science Foundation under grant ECCS-1809454.

DEDICATION



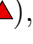
I dedicate this thesis to the people, who inspired me to pursue my dreams. A special feeling of gratitude to my loving parents, Dursun and Emine, and my siblings, Tlay, Kenan, Kadriye and Demet, for their words of advice and encouragement, and the unconditional support I always received from them. It is much easier to move forward when I know they have my back.

My nephews, Efe, Alper, Emir and Abdulkadir, and my nieces Gizem, Ezgi and Aybke deserve special recognition and thanks for their love, humor, and sincerity.

Last, but not least, I send big thanks to all my friends in here and in Turkey as well as the UTA Turkish community for their support and sharing wonderful times with me during my education.

LIST OF ILLUSTRATIONS

Figure	Page
1. A portion of a meshed MTDC grid. The grid is equipped with switching devices to enable line switching decisions, \vec{x} . VSCs couple AC and DC parts by controlling their voltage and power levels on both sides.	11
2. Droop parameters optimized for the load/generation profile at time t_1 violates the safe operating region until the subsequent update that happens at time $t_3 + \Delta t_3$. (a) Load/generation profile and DC side voltage variation. (b) Generalized voltage-droop characteristics.	15
3. The modified CIGRE B4 DC grid equipped with line switches. DC cable resistance for +/-400 kv is 0.0095 Ω /km.	23
4. Topology-cognizant OPF testbed on a real-time HIL platform has hardware emulation (Typhoon HIL), controller implementation (dSPACE), and TCP/IP communication link.	24
5. MTDC operation with droop control under varying load: (a) DC side voltage variation, (b) DC side power variation, and (c) Total power losses. . .	25
6. MTDC operation with static OPF under varying load: (a) DC side voltage variation, (b) DC side power variation, and (c) Total power losses.	26
7. MTDC operation with topology-cognizant OPF disregarding voltage safety constraints in (2.20s). The variations in load/generation have DC voltage at bus 5 violate the safety limit: (a) DC side voltage variation (dotted line shows the safety limit, $v_{\max}^{\text{dc}} = 402.8$ kV), (b) DC side power variation, and (c) Total power losses.	28

8. MTDC operation with topology-cognizant OPF considering the voltage safety constraints in (2.20s): (a) DC side voltage variation (dotted line shows the safety limit, $v_{\max}^{\text{dc}} = 402.8$ kV), (b) DC side power variation, and (c) Total power losses.	29
9. Three bus DC distribution network is equipped with sensors at buses 1 and 2 and the line between buses 1-3 to collect data $(\hat{v}_1, \hat{x}_2, \hat{i}_1, \hat{i}_2)$. Optimizer jointly performs state estimation and topology identification using these limited measurements, and infers unknown voltage, v_2, v_3 , and statuses of the lines, x_1, x_3	36
10. Comparative convergence rates of proposed and generalized state estimation methods for the IEEE (a) 9-bus, (b) 14-bus, and (c) 30 bus systems.	50
11. The modified IEEE 14-bus system populated with 5 DC-DC buck converters (illustrated by ) , and equipped with sensors to monitor voltages (illustrated by ) , line statuses (illustrated by ) , and injected current at bus $k \in \mathcal{N} \setminus \{\mathcal{Z}\}$	51
12. Load power trajectories at selected buses 1, 3, 4, 5, 6, and 9.	51
13. DC network joint observation testbed on a HIL system embodying of controller implementation (dSPACE), real-time hardware emulation (Typhoon HIL), and TCP/IP communication link for data transfer.	52
14. Estimated (v_k) , and ground-truth (\tilde{v}_k) voltage values for unmonitored buses.	53
15. Estimated (x_l) , and ground-truth (\tilde{x}_l) values for the statuses of the lines in response to the removal of one line. x_{a-b} denotes the line status for a line which starts from node a and ends in b.	54
16. The performance of (3.22) to estimate the vector of voltages in the case where the goal is to solve the state estimation problem in the presence of noisy measurements without increasing the number of available sensors.	56

17. Estimated voltage values obtained by (3.22) for the monitored sensor measurements corrupted by %1 additive noise.	57
18. The performance of (3.22) to estimate the vector of voltages when solving the state estimation and topology identification problem, in the presence of noisy measurements, with the help of additional voltage measurements. . .	58
19. Estimated voltage values obtained by (3.22) at selected sensor measurements. Each measurement is corrupted by %1 additive noise.	59
20. The performance of (3.22) to estimate the vector of voltages for the modified IEEE 14-bus system where each measurement is either corrupted by zero-mean Gaussian noises with 1% standard deviation or 100% of the corresponding original value.	60
21. Estimated voltage values obtained by (3.22) at selected sensor measurements. Each measurement is either corrupted by zero-mean Gaussian noises with 1% standard deviation or 100% of the corresponding original value. The voltage measurement at bus 5, \hat{v}_5 , is out of range in Figure as it is entirely corrupted.	61
22. Estimated (x_l) , and ground-truth values, for the line statuses in response to the removal of one line. x_{a-b} denotes the status of a line starting from node a and ending in b.	62
23. Changes on the levels of ground-truth voltage values at bus 4 due to changes in topology and load power trajectories.	62

24. Contingency scenario samples for a portion of power grid. The base case refers to the scenario 0 that means no contingency. The red labels highlight the failure of a generator and a transmission line. In Scenario 1, generator 1 fails while generator 2 readjusts its generation according to weight $\alpha_{1,2}$. Scenario 2 illustrates a transmission line failure, while generator 1 and 2 contribute to power redispatch, Δ_2 69
25. The characteristics of \mathcal{F}_θ and $\mathcal{F}_\theta^{\text{smooth}}$ when $\theta = 0, \theta = \pi/8, \theta = \pi/6, \theta = \pi/4$. 71
26. Generator active power response relation between pre- and post-contingency:
 (a) Actual characteristics: $x = p_{c,g}^{\text{gen}}, y = p_{0,g}^{\text{gen}} + \alpha_{c,g}\Delta_c$, (b) Normalization of the actual characteristics: $\hat{x} = \frac{2p_{c,g}^{\text{gen}} - p_{c,g}^{\text{max}} + p_{c,g}^{\text{min}}}{p_{c,g}^{\text{max}} + p_{c,g}^{\text{min}}}, \hat{y} = \frac{2(p_{0,g}^{\text{gen}} + \alpha_{c,g}\Delta_c) - p_{c,g}^{\text{max}} + p_{c,g}^{\text{min}}}{p_{c,g}^{\text{max}} + p_{c,g}^{\text{min}}}$. 74
27. Generator reactive power response relation between pre- and post-contingency:
 (a) Actual characteristics: $x = q_{c,g}^{\text{gen}}, y = |v_{0,i}| - |v_{c,i}|$, (b) Normalization of the actual characteristics: $\hat{x} = \frac{2q_{c,g}^{\text{gen}} - q_{c,g}^{\text{max}} - q_{c,g}^{\text{min}}}{q_{c,g}^{\text{max}} - q_{c,g}^{\text{min}}}, \hat{y} = |v_{0,i}| - |v_{c,i}|$ 76
28. The characteristics of $(x, y) \in \mathcal{F}_{\pi/4}^{\text{smooth}}$ for different h values with the candidate curves (a) (4.14a), (b) (4.14b), (c) (4.14c), (d) (4.14d), (e) (4.14e). . 80
29. The characteristics of $(x, y) \in \mathcal{F}_0^{\text{smooth}}$ for different h values with the candidate curves (a) (4.14a), (b) (4.14b), (c) (4.14c), (d) (4.14d), (e) (4.14e). . 80

LIST OF TABLES

Table	Page
1. Total Losses with different Approaches (MW)	27
2. List of Contingencies for IEEE 30-bus system	82
3. Active power variations in response to contingency scenarios (pu)	82
4. Reactive power variations in response to contingency scenarios (pu)	82
5. Voltage variations in response to contingency scenarios (pu). Values in red color refer to the PV/PQ switching due to a generator outage.	83
6. Performance Comparison of the Proposed Functions	83

ABSTRACT

HIGH-PERFORMANCE OPTIMIZATION METHODS FOR EMERGING POWER SYSTEMS

TUNCAY ALTUN, Ph.D.

The University of Texas at Arlington, August, 2020

Supervising Professors: Ali Davoudi, Ramtin Madani

This dissertation investigates the applications of high performance optimization techniques for emerging power systems with augmented power electronics devices. One of the main sources of complexity in the analysis of power systems is rooted in the power flow equations modeling steady-state relationship between power injections and voltages. Hence, the present work is in-part focused on addressing the complexity of power flow equations in the presence of power electronic devices. In contrast to the classic optimal power flow (OPF) solution techniques, we employ convex optimization methods to reliably find globally optimal solutions in polynomial time.

The first chapter investigates the optimization of droop control set-points, i.e., voltage and power levels at each bus, and the switching status of transmission lines, in multi-terminal direct current (MTDC) grids. Additional constraints, that ensure a safe operation in response to power fluctuation while updating droop set-points, are integrated into the problem formulation. This problem is expressed as a mixed-integer nonlinear program with three sources of computational difficulty: i) Non-convex power balance and flow equations, (ii) Non-convex converter loss equations,

and iii) Binary variables standing for the on/off status of transmission lines. Second-order cone programming relaxation tackles the non-convexity of converter loss, power flows and power balance equations, and branch-and-bound search determines the optimal switching status of transmission lines. CIGRE B4 DC grid benchmark is emulated in a real-time hardware-in-the-loop environment to corroborate the proposed method.

This dissertation next copes with the long-standing state estimation and topology identification problems in direct current (DC) networks. This problem is challenging due to binary decisions and nonlinear relations between sensor measurements and state variables. We introduce a non-convex nuclear norm estimator whose nonconvexity is addressed by incorporating two inertia terms. In the presence of noise, penalty terms are integrated into the objective function to estimate unknown noise values. Numerical results for the modified IEEE 9-bus, 14-bus, and 30-bus systems corroborate the merits of the proposed technique. Furthermore, this technique is experimentally validated for a converter-augmented 14-bus system in a real-time hardware-in-the-loop platform.

Lastly, this work introduces an enhanced modeling for generator response in the security-constrained optimal power flow (SCOPF) problem, in which every contingency scenario corresponds to the outage of an arbitrary set of generators and lines. Integrating active and reactive power contingency response into SCOPF problem is a major computational challenge. We introduce a family of surrogate models for common-practice power system contingency response decisions such as PV/PQ switching and active power redistribution. The proposed models prevent physical and operational violations by means of optimally, allocating active power imbalances among available generators and determining the most efficient PV/PQ switching de-

cisions. The efficacy and scalability of the proposed method is numerically validated on an IEEE benchmark system.

TABLE OF CONTENTS

ACKNOWLEDGEMENTS	iii
DEDICATION	iv
LIST OF ILLUSTRATIONS	v
LIST OF TABLES	ix
ABSTRACT	x
CHAPTER ONE: INTRODUCTION	1
CHAPTER TWO: TOPOLOGY-COGNIZANT OPTIMAL POWER FLOW IN MULTI-TERMINAL DC GRIDS	6
CHAPTER THREE: OBSERVATION OF STATE AND TOPOLOGY IN DC NETWORKS	32
CHAPTER FOUR: ENHANCED MODELING OF GENERATOR RESPONSE IN SECURITY-CONSTRAINED OPF	66
CHAPTER FIVE: CONCLUSION AND FUTURE WORKS	84
REFERENCES	86
BIOGRAPHICAL STATEMENT	100

CHAPTER 1

INTRODUCTION

The reliability and economic operation of electric power systems is a major concern of power system engineers. The power flow investigation underpins many static or dynamic applications in power systems. These applications include stability analysis, optimal power flow, contingency analysis, etc. The power flow equations amount to nonlinear relationship of voltage and power in a power system. Accurate solution of the power flow problem ensures that generators meet the required power, i.e., total load and transmission losses. Solving power flow equations approximated by linearization techniques falls short of fidelity since physical and operational constraints are not properly respected.

In traditional power systems, electricity is generated in bulk amount at medium voltage level far away from the consumer. Even though traditional power system model is fairly straightforward, it has some serious technical and environmental drawbacks. These drawbacks include high CO_2 emission, complex penetration of renewable energy technologies, and its obsolete structure that does not allow to accommodate ever increasing electricity demand. On the other hand, with help of power electronics devices, distributed generation based future power systems offer improved efficiency, reliability, expandability, and stability. In distributed generation based power systems, generation and consumption happen in a close physical region. This future power system concept also revitalizes the importance of DC distribution/transmission.

Convex relaxation methods, consisting of second-order cone programming (SOCP) and semi-definite programming (SDP), can transform nonlinear power flow optimization into convex surrogates by reformulating it in a high-dimensional space while preserving equivalency with the original non-convex problem [1, 2]. The SDP and SOCP relaxations, and their variations, have manifested notable success in solving OPF problems in AC systems [3, 4]. Static OPF solutions, however, overlook the optimal switching of transmission lines that can help relieve voltage violations and line overloads, protect the grid from abnormal operations, minimize transmission losses, or schedule maintenance [5]. In fact, a transmission line built for a long-term requirement could exhibit dispatch inefficiencies [6]. Lately, mixed-integer cone programming methods have been used to solve AC grid topology problems [7, 8].

These approaches have been extended to deal with state estimation problem that determines the network states based on a limited number of measurements or based on a corrupted sensory information. The state estimation process is conventionally formulated as a nonlinear least-squares problem, and is usually treated by variations of Gauss-Newton algorithms [9]. The weighted least-squares (WLS) estimation criterion has been employed in practice to filter out Gaussian measurement noise with certain statistical properties [10, 11]. As WLS is susceptible to gross measurement errors, other gross error detection and identification methods have been proposed to perform accurate state estimation [12, 13, 14, 15, 11]. Given their non-convex problem formulation, the Gauss-Newton algorithm is sensitive to the initial points, and might converge to local minima [16]. Convex relaxation methods can either directly solve the estimation problem [17] or provide an initial guess for the Newton's method [18]. Convergence guarantees for the estimation process using convex relaxation techniques are given in [19]. With measurement redundancy, incorporating penalty terms

in the formulation of the objective function can help cleansing noise and bad data [20, 21, 22]. These techniques, however, assume a fixed network topology.

Another issue in power systems is that transmission losses cannot be identified in advance. Therefore, required total power generation to supply a known demand is unpredictable [23]. Common practice in power systems is to assume there exist at least one slack bus. In slack bus, power generation can be readjusted to compensate the system power imbalances[24]. To this end, power flow algorithms, such as Gauss, fast decoupled, Gauss-Seidel, Newton-Raphson , backward/forward sweep, and other derivative approaches compute the flow of electrical power based on single slack bus model [25]. However, assuming a conceptual generator that has an infinite capacity or can draw a negative power does not reflect the real behavior of the power systems.

To address aforementioned drawbacks, various modern optimization techniques have transformed nonlinear power flow and balance constraints into convex alternatives while attempting to conserve equivalency to the non-convex original problem. This dissertation discusses high performance optimization for emerging power systems while satisfying physical network constraints and operational limits. Followings categorize the research outcomes:

- Chapter 2 introduces a mixed-integer second-order cone programming (MISOCP) formulation for the topology-cognizant OPF in MTDC grids to minimize both transmission and converter losses. The proposed formulation includes safety constraints that prevent voltage violations caused by power fluctuation in between two droop set-point updates.
- Chapter 3 leverages the physical properties of DC networks to develop a joint estimation and topology identification algorithm using a limited number of measurement. We formulate this as a non-convex mixed-binary problem, develop a non-convex nuclear norm estimator, and address this non-convexity by us-

ing two inertia terms. The presence of zero injection buses (i.e., a bus with no load or converter) is used to strengthen the convex relaxation and decrease the number of required sensors. The devised convex optimization framework is robustified against noise by upgrading to a penalized convex program.

- Chapter 4 presents several equivalent continuously-differentiable security constrained OPF (SCOPF) models that respect high fidelity physical model of generators with respect to extensive list of contingency scenarios. The introduced models prevent physical and operational violations by means of optimally, allocating active power imbalances among available generators and deciding the type of bus, i.e., PV/PQ switching, respectively.

The resulting publications are listed below:

- [J1] T. Altun, R. Madani and A. Davoudi, “Topology-cognizant Optimal Power Flow in Multi-terminal DC Grids,” Under Preparation.
- [J2] T. Altun, R. Madani and A. Davoudi, “Observation of State and Topology in DC networks,” IEEE Transactions on Power Systems, Revision submitted in June 2020, (Manuscript ID: TPWRS-01084-2019.R3).
- [J3] T. Altun, R. Madani and A. Davoudi, “Enhanced Modeling of Generator Response in Security-constrained Optimal Power Flow,” Under Preparation.

TOPOLOGY-COGNIZANT OPTIMAL POWER FLOW IN MULTI-TERMINAL
DC GRIDS

T. Altun, R. Madani and A. Davoudi, "Topology-cognizant Optimal Power Flow in
Multi-terminal DC Grids," Under Preparation.

CHAPTER 2

TOPOLOGY-COGNIZANT OPTIMAL POWER FLOW IN MULTI-TERMINAL DC GRIDS

Multi-terminal direct current (MTDC) grids are becoming popular as they allow efficient power exchange between synchronized or unsynchronized power grids, and are suitable candidates for offshore wind farms integration [26] or power exchange in long-distance (e.g., European supergrid [27]) as its DC grid enjoys a simpler control mechanism and avoids challenges native to AC grids. Moreover, voltage-source converters (VSCs) based MTDC grids allow interconnection with weak AC grids, black start in the case of blackouts, and power flow reversal without switching the voltage polarity [28]. Given their superiority over AC power transmission, there are ongoing efforts to realize bulk power exchange among independent grids using the VSC technology. VSC's DC voltage control is the key measure to proper power dispatch and loss management in a MTDC grid, and is mainly done via master-slave [29], voltage margin [30], or voltage droop [31] mechanisms. Droop control approach is more dependable than voltage margin and master-slave controls if several converters actively participate in the regulation process [32].

The two-tier control hierarchy of MTDC grids [33, 34] includes a faster, lower-level droop controller that locally regulates the VSC voltage at the cost of power sharing objectives. Hence, the upper-level optimizer periodically tunes the set-points of the lower-level droop control to meet predefined optimization objectives, i.e, minimizing generation cost, transmission loss, etc. The optimization involved in tuning droop set-points could become computationally prohibitive for real-time applications

[35]. This delay, or any interruption in the communication between the two control layers, could cause a prescribed droop set-point to violate an operational safety limit, particularly if the load demand or power generation fluctuate noticeably before the subsequent droop set-points update [36, 37]. Preventive measures, while still pursuing optimality in MTDC grids, are rare in the literature, e.g., see [38, 39, 40].

The optimal power flow (OPF) in MTDC grids aims to minimize transmission loss alone [41] or along with conversion loss [42]. Convex relaxation methods can transform nonlinear power flow optimization into convex surrogates by reformulating it in a high-dimensional space while preserving the equivalency with the original non-convex problem [1, 2]. These approaches have been extended to the static OPF problem of MTDC grids that also suffer from non-convex converter loss equations [43, 44, 45].

Static OPF solutions, however, overlook the optimal switching of transmission lines that can help lessen line overloads, minimize transmission losses, address voltage violations, protect the grid from abnormal operations, or schedule maintenance [5]. In fact, a transmission line built for a long-term requirement could exhibit dispatch inefficiencies [6]. Recently, AC grid topology problems have been solved using mixed-integer cone programming approaches [7, 8, 46]. The authors have developed a mixed-integer second-order cone programming (MISOCP) model to reconfigure a DC network to minimize the generational cost in static OPF and secure the operation in response to contingencies [47]. MTDC grid, unlike DC or AC networks, includes operation in high voltage, presence of VSCs, and combination of AC and DC grid constraints that bring additional complexities into its MISOCP formulation. Accordingly, this chapter offers a MISOCP formulation for the topology-cognizant OPF in MTDC grids to minimize both transmission and converter losses while respecting physical and operational constraints including AC part and VSC characteristics.

The proposed formulation involves safety constraints that prevent voltage violations caused by power fluctuation in between two droop set-point updates. The noticeable contributions of this chapter are summarized as:

- Additional constraints that sustain a safe operation by further restricting voltage limits, in response to volatile generation/load profiles in between two droop set-point updates, are integrated into the problem formulation.
- Static OPF is extended to derive a topology-cognizant OPF model when binary variables account for the switching status of transmission lines.
- The proposed mixed-integer nonlinear programming model is transformed into MISOCP surrogate to obtain a tractable topology-cognizant OPF formulation for MTDC grids.
- The proposed static OPF, topology-cognizant OPF without safety constraints, and topology-cognizant OPF with safety constraints are studied on the modified IEEE 14, 30, 57-bus systems and experimentally validated for the CIGRE B4 DC grid benchmark through real-time hardware-in-the-loop (HIL) experiments.

The rest of the chapter has the following organization. Section 2.1 contains preliminary materials. Section 2.2 elaborates the modeling of MTDC grids. Section 2.3 incorporates the switching actions of transmission lines into the OPF problem, and presents its convexified version. In Section 2.4, the OPF and topology-cognizant OPF solutions are experimentally and numerically validated through CIGRE B4 DC grid benchmark and several modified IEEE benchmarks, respectively.

2.1 Notations and Grid Terminologies

2.1.1 Notations

Bold small letter, (\boldsymbol{x}) , and capital letter, (\boldsymbol{X}) , represent vectors and matrices, respectively. $\mathbf{1}$ and $\mathbf{0}$ refer to vectors with all elements as 1 and 0, respectively. The sets of complex and real numbers are symbolized with \mathbb{C} and \mathbb{R} respectively. \mathbb{H}^n and \mathbb{S}^n represent the hermitian and symmetric matrices size of $n \times n$, respectively. $\text{imag}\{\cdot\}$ and $\text{real}\{\cdot\}$ define the imaginary and real parts of a complex number or matrix, respectively. A matrix's i^{th} row and j^{th} column is referred with (i, j) . The transpose and conjugate transpose operators are denoted with $(\cdot)^\top$ and $(\cdot)^*$, respectively. $|\cdot|$ refers the cardinality of a set or the absolute/magnitude value of a vector/scalar. $\text{tr}\{\cdot\}$ refers to the trace of a given matrix. $\|\cdot\|_2$ stands for the euclidean norm of a vector. $\text{diag}\{\cdot\}$ creates a vector using the matrix's diagonal entries. $[\cdot]$ composes a matrix with diagonal entries from a given vector.

2.1.2 Grid Terminologies

Figure 1 demonstrates a schematic for an MTDC grid. Grid buses are connected via DC transmission lines. Terminologies for grid elements are elaborated here:

- **DC Grid:** The DC transmission grid is structured using directed graph $\mathcal{H} = (\mathcal{N}, \mathcal{L})$ where the sets of buses and lines are denoted by \mathcal{N} and \mathcal{L} , respectively. The DC grid *from* and *to* line-incidence matrices are defined with the pairs $\vec{\mathbf{L}}, \vec{\mathbf{L}} \in \{0, 1\}^{|\mathcal{L}| \times |\mathcal{N}|}$, respectively. $\vec{L}_{lk} = 1$ ($\vec{L}_{lk} = 1$) for every $k \in \mathcal{N}$ and $l \in \mathcal{L}$, iff the transmission line l starts(ends) at bus, k . The matrices $\mathbf{Y} \in \mathbb{R}^{|\mathcal{N}| \times |\mathcal{N}|}$, $\vec{\mathbf{Y}}, \vec{\mathbf{Y}} \in \mathbb{R}^{|\mathcal{L}| \times |\mathcal{N}|}$ represent the bus-conductance, and the *from* and *to* line-conductance matrices of the DC grid, respectively. The *from* and *to* vectors of transmission line power flows are defined as $\vec{\mathbf{f}}$ and $\vec{\mathbf{f}} \in \mathbb{R}^{|\mathcal{L}|}$, respectively. The power flow limits is represented with $\vec{\mathbf{f}}^{\max} \in (\mathbb{R} \cup \{\infty\})^{|\mathcal{L}|}$.

Additionally, $\vec{\mathbf{x}} \in \{0, 1\}^{|\mathcal{L}|}$ defines the vector that acts for the switching status of transmission lines. Let $\vec{\mathbf{x}}_{\min}, \vec{\mathbf{x}}_{\max} \in \{0, 1\}^{|\mathcal{L}|}$ encapsulate prior knowledge of the on/off switches, i.e.,

$$\begin{aligned} \vec{x}_{\min_l} = \vec{x}_{\max_l} = 0, & \quad \text{if line } l \in \mathcal{L} \text{ is known to be disconnected,} \\ \vec{x}_{\min_l} = \vec{x}_{\max_l} = 1, & \quad \text{if line } l \in \mathcal{L} \text{ is known to be connected,} \\ \vec{x}_{\min_l} = 0, \quad \vec{x}_{\max_l} = 1, & \quad \text{otherwise.} \end{aligned}$$

Finally, let $\mathbf{v}^{\text{dc}}, \mathbf{p}^{\text{dc}} \in \mathbb{R}^{|\mathcal{N}|}$ represent the vectors of DC bus voltages and active power injections into the DC side.

- **Buses/VSCs:** Each DC bus $k \in \mathcal{N}$ is assumed to accommodate a single voltage-source converter (VSC) which is connected to a set of loads and generators through a phase reactor, modeled as a series impedance $z_k \in \mathbb{C}$. Define $\mathbf{z}, \mathbf{i}^{\text{ac}} \in \mathbb{C}^{|\mathcal{N}|}$ as the vectors of phase-reactor impedance and current values, respectively. Let $\mathbf{v}_c^{\text{ac}}, \mathbf{v}_f^{\text{ac}} \in \mathbb{C}^{|\mathcal{N}|}$ account for the vectors of VSC and load/generation-side AC voltages, respectively. Let $\mathbf{s}^{\text{ac}} \in \mathbb{C}^{|\mathcal{N}|}$, and $\mathbf{p}^{\text{ac}}, \mathbf{q}^{\text{ac}} \in \mathbb{R}^{|\mathcal{N}|}$, respectively, represent the vectors of apparent, active and reactive power injections from VSCs into the AC sides.
- **Generators/Loads:** Let \mathcal{G} be the set for generators and $\mathbf{G} \in \{0, 1\}^{|\mathcal{G}| \times |\mathcal{N}|}$ as the generator incidence matrix, where $G_{gk} = 1$ if and only if the generator $g \in \mathcal{G}$ is located at the AC side of the bus $k \in \mathcal{N}$. $\mathbf{s}^g \in \mathbb{C}^{|\mathcal{G}|}$ and $\mathbf{p}^g, \mathbf{q}^g \in \mathbb{R}^{|\mathcal{G}|}$, respectively, represent the vectors of apparent, active and reactive power generations. Define \mathcal{D} as the set of loads and $\mathbf{D} \in \{0, 1\}^{|\mathcal{D}| \times |\mathcal{N}|}$ as the load incidence matrix where $D_{dk} = 1$ if and only if the load $d \in \mathcal{D}$ is located at the

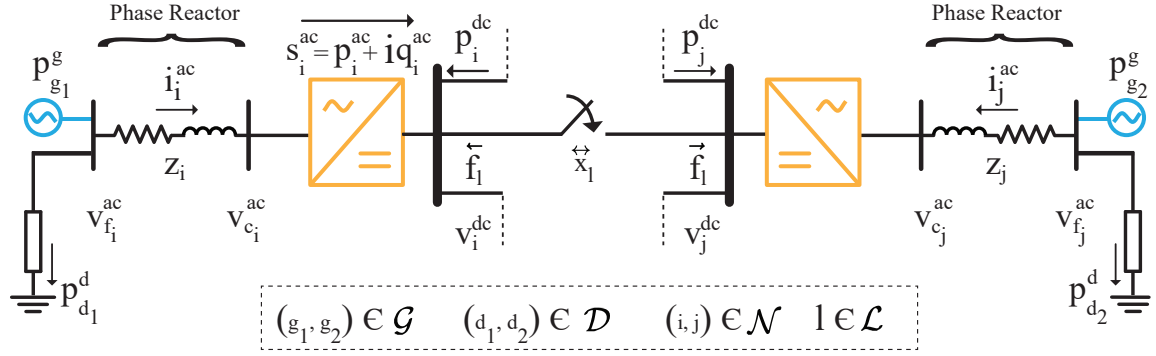


Figure 1: A portion of a meshed MTDC grid. The grid is equipped with switching devices to enable line switching decisions, \vec{x} . VSCs couple AC and DC parts by controlling their voltage and power levels on both sides.

AC side of the bus $k \in \mathcal{N}$. Finally, $\mathbf{p}^d \in \mathbb{R}^{|\mathcal{D}|}$ represents the vectors of active power demand.

2.2 MTDC Grid Model

2.2.1 AC/DC Coupling

VSC losses are approximated by a quadratic polynomial with respect to current magnitude as

$$\mathbf{p}_{\text{loss}}^{\text{conv}} \triangleq -\mathbf{p}^{\text{ac}} - \mathbf{p}^{\text{dc}} = \mathbf{a} + [\mathbf{b}]|\mathbf{i}^{\text{ac}}| + [\mathbf{c}]|\mathbf{i}^{\text{ac}}|^2, \quad (2.1)$$

where $\mathbf{a}, \mathbf{b}, \mathbf{c} \in \mathbb{R}^{|\mathcal{N}|}$ are the vectors of positive coefficients [43], and \mathbf{p}^{ac} and \mathbf{p}^{dc} are the vectors of active power injections by the VSCs into the AC and DC sides, respectively. Additionally, the AC and DC side voltages are related with a modulation factor, m ,

$$|\mathbf{v}_c^{\text{ac}}| \leq \sqrt{\frac{3}{2}} m \mathbf{v}^{\text{dc}}. \quad (2.2)$$

2.2.2 VSC Limits

The AC side complex powers can be calculated as

$$\mathbf{s}^{\text{ac}} = [\mathbf{v}_c^{\text{ac}}] ([\mathbf{z}]^{-1}(\mathbf{v}_c^{\text{ac}} - \mathbf{v}_f^{\text{ac}}))^*, \quad (2.3)$$

with the VSCs active power is bounded as

$$\mathbf{p}_{\min}^{\text{ac}} \leq \mathbf{p}^{\text{ac}} \leq \mathbf{p}_{\max}^{\text{ac}}. \quad (2.4)$$

With no loss of generality, the VSC reactive power limits can be formulated as

$$-m_b |\bar{\mathbf{s}}^{\text{ac}}| \leq \mathbf{q}^{\text{ac}} \leq [|\text{imag}\{\mathbf{z}\}|]^{-1} [\mathbf{v}_{c_{\max}}^{\text{ac}}] (\mathbf{v}_{c_{\max}}^{\text{ac}} - |\mathbf{v}_f^{\text{ac}}|), \quad (2.5)$$

where m_b is a positive constant, and $|\bar{\mathbf{s}}^{\text{ac}}|$ is the vector of nominal VSC apparent power values [42]. The right side of inequality (2.5) is the outcome of the approximation on phase-angle difference between phase reactor buses, $\theta_{c_i} - \theta_{f_i} = 0$ for every $i \in \mathcal{N}$. To further simplify (2.5) while finding the maximum reactive power constraint, one can substitute $|\mathbf{v}_f^{\text{ac}}|$ with $\mathbf{v}_{f_{\min}}^{\text{ac}}$ [43]. Finally, according to Ohm's law,

$$\mathbf{i}^{\text{ac}} = [\mathbf{z}]^{-1}(\mathbf{v}_c^{\text{ac}} - \mathbf{v}_f^{\text{ac}}), \quad (2.6)$$

and the current magnitude $|\mathbf{i}^{\text{ac}}|$, should not exceed an upper limit $|\mathbf{i}_{\max}^{\text{ac}}|$, to be compatible with the limits of phase reactor and controller.

2.2.3 Generator/Load Limits

Active power balance at the generator/load sides of phase reactors can be formulated as

$$\mathbf{G}^\top \mathbf{p}^g - \mathbf{D}^\top \mathbf{p}^d = \text{real}\{[\mathbf{v}_f^{\text{ac}}]([\mathbf{z}]^{-1}(\mathbf{v}_f^{\text{ac}} - \mathbf{v}_c^{\text{ac}}))^*\}, \quad (2.7)$$

with

$$\mathbf{p}_{\min}^g \leq \mathbf{p}^g \leq \mathbf{p}_{\max}^g, \quad (2.8)$$

$$\mathbf{v}_{\min}^{\text{ac}} \leq |\mathbf{v}_f^{\text{ac}}| \leq \mathbf{v}_{\max}^{\text{ac}}, \quad (2.9)$$

enforcing generator/load power and voltage limits.

2.2.4 DC Grid Constraints

Nodal power balance equations of the DC grid can be formulated as

$$\vec{\mathbf{L}}^\top \vec{\mathbf{f}} + \overleftarrow{\mathbf{L}}^\top \overleftarrow{\mathbf{f}} = \mathbf{p}^{\text{dc}}, \quad (2.10)$$

where $\vec{\mathbf{f}}$ and $\overleftarrow{\mathbf{f}}$ are dictated by nodal DC voltages and the status of transmission lines:

$$\vec{\mathbf{f}} = [\vec{\mathbf{x}}] \text{diag}\{\vec{\mathbf{L}}\mathbf{v}^{\text{dc}}\mathbf{v}^{\text{dc}\top}\vec{\mathbf{Y}}^\top\} \leq \vec{\mathbf{f}}_{\max}, \quad (2.11a)$$

$$\overleftarrow{\mathbf{f}} = [\overleftarrow{\mathbf{x}}] \text{diag}\{\overleftarrow{\mathbf{L}}\mathbf{v}^{\text{dc}}\mathbf{v}^{\text{dc}\top}\overleftarrow{\mathbf{Y}}^\top\} \leq \overleftarrow{\mathbf{f}}_{\max}, \quad (2.11b)$$

and constrained by thermal limits of the line. Additionally, nodal voltages and power injections of the DC grid should be bounded as follows:

$$\mathbf{v}_{\min}^{\text{dc}} \leq |\mathbf{v}^{\text{dc}}| \leq \mathbf{v}_{\max}^{\text{dc}}, \quad (2.12)$$

$$\mathbf{p}_{\min}^{\text{dc}} \leq \mathbf{p}^{\text{dc}} \leq \mathbf{p}_{\max}^{\text{dc}}. \quad (2.13)$$

Constraints (2.12)–(2.13) enforce steady-state safety requirements. However, due to transient effects, voltage limits in (2.12) need to be further restricted based on variations in load and generation, as well as the computational time delays in between droop set-point updates. In the following subsection, we formulate complementary voltage constraints that can further improve operational safety.

2.2.5 MTDC Control Strategy

The generalized VSC voltage-droop characteristic [31] can be written as

$$\alpha_k v_k^{\text{dc}} + \beta_k p_k^{\text{dc}} + \gamma_k = 0, \quad \forall k \in \mathcal{N}, \quad (2.14)$$

where p_k^{dc} and v_k^{dc} are the DC power and voltage set-points of the VSC at bus k . α_k , β_k , and γ_k denote the corresponding converter's voltage-droop parameters. In this chapter, we assume that $\alpha_k = 1$. The voltage-droop slope is

$$\kappa_k \triangleq \beta_k = \frac{v_{\max_k}^{\text{dc}} - v_{\min_k}^{\text{dc}}}{p_{\max_k}^{\text{dc}} - p_{\min_k}^{\text{dc}}}, \quad (2.15)$$

and additionally, $\gamma_k = -v_k^{\text{dc}} - \kappa_k p_k^{\text{dc}}$.

Equation (2.14) guarantees the optimal operation as long as updating droop set-points is fast enough compared to power fluctuations. However, due to the limits in computational speed, this assumption remains valid only if changes in load/generation are negligible. The unwanted voltage deviation, caused by rapid changes, can be formulated as

$$\Delta v_k = \kappa_k \Delta p_k, \quad (2.16)$$

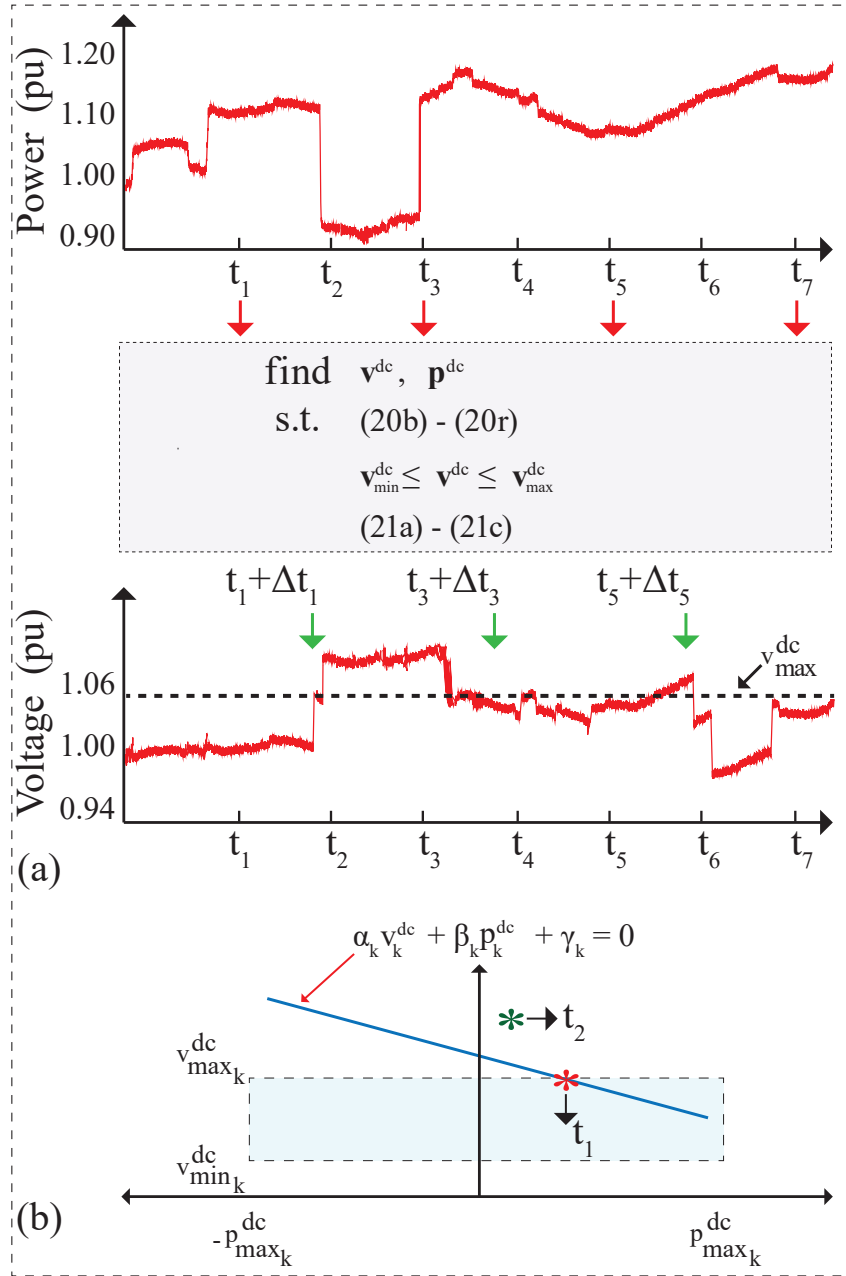


Figure 2: Droop parameters optimized for the load/generation profile at time t_1 violates the safe operating region until the subsequent update that happens at time $t_3 + \Delta t_3$. (a) Load/generation profile and DC side voltage variation. (b) Generalized voltage-droop characteristics.

where $\Delta v_k = |v_k^{\text{dc}}(t_1) - v_k^{\text{dc}}(t_2)|$ and $\Delta p_k = |p_k^{\text{dc}}(t_1) - p_k^{\text{dc}}(t_2)|$. We seek to obtain conservative bounds on changes in DC voltage magnitudes, with the aim of ensuring smooth transition to the next operating point.

An illustrative example is provided in Figure 2 to highlight the necessity of this constraint. In Figure 2 (a), the optimizer collects the load profile at time t_1 . Optimizing droop set-points requires a computational time, Δt_1 . During this time, a noticeable variation in load/generation, as it happens at time t_2 , invalidates obtained droop set-points until the subsequent update (at time $t_3 + \Delta t_3$). Thus, droop set-points found at time $t_1 + \Delta t_1$ become harmful for grid operation, particularly within the interval $[t_2, t_3 + \Delta t_3]$.

To prevent this issue, one can underpin droop control with additional constraints so that the DC voltage remains within the pre-described boundaries. We offer the following additional voltage constraints, instead of (2.12), to guarantee a safe operation under limited load/generation volatility:

$$v_{k_{\min}}^{\text{dc}} + \Delta v_k = v_{k_{\min}}^{\text{dc}} + \kappa_k \Delta p_k \leq v_k^{\text{dc}}, \quad (2.17)$$

$$v_{k_{\max}}^{\text{dc}} - \Delta v_k = v_{k_{\max}}^{\text{dc}} - \kappa_k \Delta p_k \geq v_k^{\text{dc}}, \quad (2.18)$$

where Δp_k denotes the power variation in the DC side. A safe operating region can be devised such that corresponding voltage constraints allow power variation up to a specified level. This level can be decided based on the predefined percentage of an existing power injection, i.e., $\Delta p_k \leq \mu_k p_k^{\text{dc}}$.

2.3 Topology-cognizant OPF

2.3.1 Formulation of the Optimal Grid Topology

In Section 2.2, we have modeled the operational and physical characteristics of a VSC-based MTDC grid. Herein, we devise an objective function that minimizes the total active power loss.

The topology-cognizant OPF can be given as

$$\text{minimize} \quad \mathbf{1}_{|\mathcal{M}|}^\top \left(\mathbf{G}^\top \mathbf{p}^g - \mathbf{D}^\top \mathbf{p}^d \right) \quad (2.19a)$$

$$\text{subject to} \quad \text{real}\{\mathbf{s}^{\text{ac}}\} + \mathbf{p}^{\text{dc}} + \mathbf{a} + [\mathbf{b}]|\mathbf{i}^{\text{ac}}| + [\mathbf{c}]|\mathbf{i}^{\text{ac}}|^2 = \mathbf{0} \quad (2.19b)$$

$$|\mathbf{v}_c^{\text{ac}}| \leq \sqrt{\frac{3}{2}} m v^{\text{dc}} \quad (2.19c)$$

$$\mathbf{s}^{\text{ac}} = [\mathbf{v}_c^{\text{ac}}] \left([\mathbf{z}]^{-1} (\mathbf{v}_c^{\text{ac}} - \mathbf{v}_f^{\text{ac}}) \right)^* \quad (2.19d)$$

$$\mathbf{p}_{\min}^{\text{ac}} \leq \text{real}\{\mathbf{s}^{\text{ac}}\} \leq \mathbf{p}_{\max}^{\text{ac}} \quad (2.19e)$$

$$\mathbf{q}_{\min}^{\text{ac}} \leq \text{imag}\{\mathbf{s}^{\text{ac}}\} \leq \mathbf{q}_{\max}^{\text{ac}} - [\bar{\mathbf{q}}^{\text{ac}}]|\mathbf{v}_f^{\text{ac}}| \quad (2.19f)$$

$$\mathbf{i}^{\text{ac}} = [\mathbf{z}]^{-1} (\mathbf{v}_c^{\text{ac}} - \mathbf{v}_f^{\text{ac}}) \quad (2.19g)$$

$$|\mathbf{i}^{\text{ac}}| \leq \mathbf{i}_{\max}^{\text{ac}} \quad (2.19h)$$

$$\mathbf{G}^\top \mathbf{p}^g - \mathbf{D}^\top \mathbf{p}^d = \text{real}\{[\mathbf{v}_f^{\text{ac}}] \left([\mathbf{z}]^{-1} (\mathbf{v}_f^{\text{ac}} - \mathbf{v}_c^{\text{ac}}) \right)^*\} \quad (2.19i)$$

$$\mathbf{p}_{\min}^g \leq \mathbf{p}^g \leq \mathbf{p}_{\max}^g \quad (2.19j)$$

$$\mathbf{v}_{f_{\min}}^{\text{ac}} \leq |\mathbf{v}_f^{\text{ac}}| \leq \mathbf{v}_{f_{\max}}^{\text{ac}} \quad (2.19k)$$

$$\mathbf{p}^{\text{dc}} = \bar{\mathbf{L}}^\top \bar{\mathbf{f}} + \bar{\mathbf{L}}^\top \bar{\mathbf{f}} \quad (2.19l)$$

$$\mathbf{p}_{\min}^{\text{dc}} \leq \mathbf{p}^{\text{dc}} \leq \mathbf{p}_{\max}^{\text{dc}} \quad (2.19m)$$

$$|\vec{f} - \text{diag}\{\vec{L} \mathbf{v}^{\text{dc}} \mathbf{v}^{\text{dc}\top} \vec{Y}^{\top}\}| \leq M(1 - \vec{x}) \quad (2.19\text{n})$$

$$|\vec{f} - \text{diag}\{\vec{L} \mathbf{v}^{\text{dc}} \mathbf{v}^{\text{dc}\top} \vec{Y}^{\top}\}| \leq M(1 - \vec{x}) \quad (2.19\text{o})$$

$$|\vec{f}| \leq [\vec{f}_{\max}] \vec{x} \quad (2.19\text{p})$$

$$|\vec{f}| \leq [\vec{f}_{\max}] \vec{x} \quad (2.19\text{q})$$

$$\vec{x}_{\min} \leq \vec{x} \leq \vec{x}_{\max} \quad (2.19\text{r})$$

$$\mathbf{v}_{\min}^{\text{dc}} + [\kappa][\mu]\mathbf{p}^{\text{dc}} \leq \mathbf{v}^{\text{dc}} \leq \mathbf{v}_{\max}^{\text{dc}} - [\kappa][\mu]\mathbf{p}^{\text{dc}} \quad (2.19\text{s})$$

$$\begin{aligned} \text{variables} \quad & \mathbf{v}^{\text{dc}}, \mathbf{p}^{\text{dc}} \in \mathbb{R}^{|\mathcal{N}|}; \quad \mathbf{v}_c^{\text{ac}}, \mathbf{v}_f^{\text{ac}}, \mathbf{i}^{\text{ac}}, \mathbf{s}^{\text{ac}} \in \mathbb{C}^{|\mathcal{N}|} \\ & \mathbf{p}^{\text{g}} \in \mathbb{R}^{|\mathcal{G}|} \quad ; \quad \vec{f}, \vec{f} \in \mathbb{R}^{|\mathcal{L}|}; \quad \vec{x} \in \{0, 1\}^{|\mathcal{L}|} \end{aligned}$$

where vectors $\mathbf{q}_{\min}^{\text{ac}}$, $\mathbf{q}_{\max}^{\text{ac}}$, and \vec{q}^{ac} are set such that (2.19f) concludes (2.5). The topology-cognizant OPF formulation (2.19) suffers from (i) non-convex power balance and flow equations (2.19d), (2.19i), (2.19n) and (2.19o), (ii) non-convex converter loss equations (2.19b), and (iii) the existence of binary variables, (2.19r), standing for the lines' statuses. The non-convex power flow equations corresponding to binary variables in (2.11a) and (2.11b) are relaxed using disjunctive inequalities, big-M reformulation, to (2.19n) and (2.19o), respectively. The big-M reformulation requires the determination of a sufficiently large multiplier (the big-M value) to ensure the equivalency to the original formulation when a transmission line is opened, $\vec{x}_l = 0$, [48, 49]. Nonlinear components, namely, $\mathbf{v}^{\text{dc}} \mathbf{v}^{\text{dc}\top}$, $|\mathbf{v}_f^{\text{ac}}|$, $|\mathbf{v}_f^{\text{ac}}|^2$, $|\mathbf{v}_c^{\text{ac}}|^2$, $\text{diag}\{\mathbf{v}_c^{\text{ac}} \mathbf{v}_f^{\text{ac}*}\}$ and $|\mathbf{i}^{\text{ac}}|$ can be convexified via conic and parabolic inequalities.

2.3.2 Formulation of the Lifted Problem

First, we introduce auxiliary variables $\mathbf{W}^{\text{dc}} \in \mathbb{S}^{|\mathcal{M}|}$, ϕ^{ac} , \mathbf{t}^{ac} , $\mathbf{w}_{\text{cc}}^{\text{ac}}$, $\mathbf{w}_{\text{ff}}^{\text{ac}} \in \mathbb{R}^{|\mathcal{M}|}$, and $\mathbf{w}_{\text{cf}}^{\text{ac}} \in \mathbb{C}^{|\mathcal{M}|}$ for nonlinear terms $\mathbf{v}^{\text{dc}}\mathbf{v}^{\text{dc}\top}$, $|\mathbf{i}^{\text{ac}}|$, $|\mathbf{i}^{\text{ac}}|^2$, $|\mathbf{v}_{\text{c}}^{\text{ac}}|^2$, $|\mathbf{v}_{\text{f}}^{\text{ac}}|^2$, and $\text{diag}\{\mathbf{v}_{\text{c}}^{\text{ac}}\mathbf{v}_{\text{f}}^{\text{ac}*}\}$, respectively. The lifted problem can be formulated as

$$\text{minimize} \quad \mathbf{1}_{|\mathcal{M}|}^\top \left(\mathbf{G}^\top \mathbf{p}^{\text{g}} - \mathbf{D}^\top \mathbf{p}^{\text{d}} \right) \quad (2.20\text{a})$$

$$\text{subject to} \quad \text{real}\{\mathbf{s}^{\text{ac}}\} + \mathbf{p}^{\text{dc}} + \mathbf{a} + [\mathbf{b}]\phi^{\text{ac}} + [\mathbf{c}]\mathbf{t}^{\text{ac}} = \mathbf{0} \quad (2.20\text{b})$$

$$0 \leq \mathbf{w}_{\text{cc}}^{\text{ac}} \leq \frac{3}{2} \text{diag}\{\mathbf{W}^{\text{dc}}\} \quad (2.20\text{c})$$

$$\mathbf{s}^{\text{ac}} = ([\mathbf{z}]^{-1})^* (\mathbf{w}_{\text{cc}}^{\text{ac}} - \mathbf{w}_{\text{cf}}^{\text{ac}}) \quad (2.20\text{d})$$

$$\mathbf{p}_{\text{min}}^{\text{ac}} \leq \text{real}\{\mathbf{s}^{\text{ac}}\} \leq \mathbf{p}_{\text{max}}^{\text{ac}} \quad (2.20\text{e})$$

$$\mathbf{q}_{\text{min}}^{\text{ac}} \leq \text{imag}\{\mathbf{s}^{\text{ac}}\} \leq \mathbf{q}_{\text{max}}^{\text{ac}} - [\bar{\mathbf{q}}^{\text{ac}}]|\mathbf{v}_{\text{f}}^{\text{ac}}| \quad (2.20\text{f})$$

$$\mathbf{t}^{\text{ac}} = [|\mathbf{z}|]^{-2} (\mathbf{w}_{\text{cc}}^{\text{ac}} + \mathbf{w}_{\text{ff}}^{\text{ac}} - 2\text{real}\{\mathbf{w}_{\text{cf}}^{\text{ac}}\}) \quad (2.20\text{g})$$

$$\mathbf{t}^{\text{ac}} \leq (\mathbf{i}_{\text{max}}^{\text{ac}})^2 \quad (2.20\text{h})$$

$$\mathbf{G}^\top \mathbf{p}^{\text{g}} - \mathbf{D}^\top \mathbf{p}^{\text{d}} = \text{real}\{[\mathbf{z}]^{-1} (\mathbf{w}_{\text{ff}}^{\text{ac}} - \mathbf{w}_{\text{cf}}^{\text{ac}})^*\} \quad (2.20\text{i})$$

$$\mathbf{p}_{\text{min}}^{\text{g}} \leq \mathbf{p}^{\text{g}} \leq \mathbf{p}_{\text{max}}^{\text{g}} \quad (2.20\text{j})$$

$$(\mathbf{v}_{\text{f}_{\text{min}}}^{\text{ac}})^2 \leq \mathbf{w}_{\text{ff}}^{\text{ac}} \leq (\mathbf{v}_{\text{f}_{\text{max}}}^{\text{ac}})^2 \quad (2.20\text{k})$$

$$\mathbf{p}^{\text{dc}} = \vec{\mathbf{L}}^\top \vec{\mathbf{f}} + \bar{\mathbf{L}}^\top \bar{\mathbf{f}} \quad (2.20\text{l})$$

$$\mathbf{p}_{\text{min}}^{\text{dc}} \leq \mathbf{p}^{\text{dc}} \leq \mathbf{p}_{\text{max}}^{\text{dc}} \quad (2.20\text{m})$$

$$|\vec{\mathbf{f}} - \text{diag}\{\vec{\mathbf{L}} \mathbf{W}^{\text{dc}} \vec{\mathbf{Y}}^\top\}| \leq M(1 - \vec{\mathbf{x}}) \quad (2.20\text{n})$$

$$|\bar{\mathbf{f}} - \text{diag}\{\bar{\mathbf{L}} \mathbf{W}^{\text{dc}} \bar{\mathbf{Y}}^\top\}| \leq M(1 - \vec{\mathbf{x}}) \quad (2.20\text{o})$$

$$|\vec{\mathbf{f}}| \leq [\vec{\mathbf{f}}_{\text{max}}] \vec{\mathbf{x}} \quad (2.20\text{p})$$

$$|\vec{f}| \leq [\vec{f}_{\max}] \vec{x} \quad (2.20q)$$

$$\vec{x}_{\min} \leq \vec{x} \leq \vec{x}_{\max} \quad (2.20r)$$

$$\mathbf{v}_{\min}^{\text{dc}} + [\kappa][\mu]\mathbf{p}^{\text{dc}} \leq \mathbf{v}^{\text{dc}} \leq \mathbf{v}_{\max}^{\text{dc}} - [\kappa][\mu]\mathbf{p}^{\text{dc}} \quad (2.20s)$$

$$\sqrt{t^{\text{ac}}} = \phi^{\text{ac}} = |i^{\text{ac}}| \quad (2.20t)$$

$$\begin{aligned} \sqrt{[\vec{L}\text{diag}\{\mathbf{W}^{\text{dc}}\}] \vec{L}\text{diag}\{\mathbf{W}^{\text{dc}}\}} &= \text{diag}\{\vec{L}\mathbf{W}^{\text{dc}}\vec{L}^\top\} \\ \text{diag}\{(\vec{L} - \bar{\vec{L}})\mathbf{W}^{\text{dc}}(\vec{L} - \bar{\vec{L}})^\top\} &= (\vec{L}\mathbf{v}^{\text{dc}} - \bar{\vec{L}}\mathbf{v}^{\text{dc}})^2 \\ \text{diag}\{(\vec{L} + \bar{\vec{L}})\mathbf{W}^{\text{dc}}(\vec{L} + \bar{\vec{L}})^\top\} &= (\vec{L}\mathbf{v}^{\text{dc}} + \bar{\vec{L}}\mathbf{v}^{\text{dc}})^2 \\ \text{diag}\{\mathbf{W}^{\text{dc}}\} &= (\mathbf{v}^{\text{dc}})^2 \end{aligned} \quad (2.20u)$$

$$\begin{aligned} \sqrt{[\mathbf{w}_{\text{ff}}^{\text{ac}}]\mathbf{w}_{\text{cc}}^{\text{ac}}} &= |\mathbf{w}_{\text{cf}}^{\text{ac}}|, \\ \mathbf{w}_{\text{ff}}^{\text{ac}} + \mathbf{w}_{\text{cc}}^{\text{ac}} - 2 \text{real}\{\mathbf{w}_{\text{cf}}^{\text{ac}}\} &= |\mathbf{v}_{\text{c}}^{\text{ac}} - \mathbf{v}_{\text{f}}^{\text{ac}}|^2, \\ \mathbf{w}_{\text{ff}}^{\text{ac}} + \mathbf{w}_{\text{cc}}^{\text{ac}} + 2 \text{real}\{\mathbf{w}_{\text{cf}}^{\text{ac}}\} &= |\mathbf{v}_{\text{c}}^{\text{ac}} + \mathbf{v}_{\text{f}}^{\text{ac}}|^2, \\ \mathbf{w}_{\text{ff}}^{\text{ac}} + \mathbf{w}_{\text{cc}}^{\text{ac}} - 2 \text{imag}\{\mathbf{w}_{\text{cf}}^{\text{ac}}\} &= |\mathbf{v}_{\text{c}}^{\text{ac}} + i\mathbf{v}_{\text{f}}^{\text{ac}}|^2, \\ \mathbf{w}_{\text{ff}}^{\text{ac}} + \mathbf{w}_{\text{cc}}^{\text{ac}} + 2 \text{imag}\{\mathbf{w}_{\text{cf}}^{\text{ac}}\} &= |\mathbf{v}_{\text{c}}^{\text{ac}} - i\mathbf{v}_{\text{f}}^{\text{ac}}|^2, \\ \mathbf{w}_{\text{ff}}^{\text{ac}} = |\mathbf{v}_{\text{f}}^{\text{ac}}|^2, \quad \mathbf{w}_{\text{cc}}^{\text{ac}} = |\mathbf{v}_{\text{c}}^{\text{ac}}|^2, \end{aligned} \quad (2.20v)$$

variables

$$\begin{aligned} \mathbf{v}_{\text{c}}^{\text{ac}}, \mathbf{v}_{\text{f}}^{\text{ac}}, \mathbf{w}_{\text{cc}}^{\text{ac}}, \mathbf{w}_{\text{ff}}^{\text{ac}}, \mathbf{w}_{\text{cf}}^{\text{ac}}, \mathbf{s}^{\text{ac}}, \mathbf{i}^{\text{ac}} &\in \mathbb{C}^{|\mathcal{N}|}, \\ \mathbf{W}^{\text{dc}} \in \mathbb{S}^{|\mathcal{N}|}; \phi^{\text{ac}}, t^{\text{ac}}, \mathbf{p}^{\text{dc}} \in \mathbb{R}^{|\mathcal{N}|}; \mathbf{p}^{\text{g}} \in \mathbb{R}^{|\mathcal{G}|}, \\ \vec{f}, \bar{\vec{f}} \in \mathbb{R}^{|\mathcal{L}|}; \vec{x} \in \{0, 1\}^{|\mathcal{L}|} \end{aligned}$$

The non-convexity of (2.19) is circumvented by lifting its nonlinear terms into the form of (2.20) while preserving the equivalency between the two formulations, with the help of additional constraints (2.20t)-(2.20v). Herein, (2.20t)-(2.20v) impose $\phi^{\text{ac}} = |\mathbf{i}^{\text{ac}}|$, $\mathbf{t}^{\text{ac}} = |\mathbf{i}^{\text{ac}}|^2$, $\mathbf{W}^{\text{dc}} = \mathbf{v}^{\text{dc}}\mathbf{v}^{\text{dc}\top}$, $\mathbf{w}_{\text{cc}}^{\text{ac}} = |\mathbf{v}_{\text{c}}^{\text{ac}}|^2$, $\mathbf{w}_{\text{ff}}^{\text{ac}} = |\mathbf{v}_{\text{f}}^{\text{ac}}|^2$, and $\mathbf{w}_{\text{cf}}^{\text{ac}} = \text{diag}\{\mathbf{v}_{\text{c}}^{\text{ac}}\mathbf{v}_{\text{f}}^{\text{ac}*}\}$. The main purpose behind these expressions is that it can be immediately convexified via transformation of equalities in (2.20t)-(2.20v) to inequalities.

2.3.3 Convex Relaxation

Motivated by [50], a MISOCP formulation can be readily obtained, by relaxing (2.20t)-(2.20v) into the following conic and parabolic inequalities:

$$\sqrt{\mathbf{t}^{\text{ac}}} \geq \phi^{\text{ac}} \geq |\mathbf{i}^{\text{ac}}| \quad (2.21\text{a})$$

$$\begin{aligned} \sqrt{[\vec{\mathbf{L}}\text{diag}\{\mathbf{W}^{\text{dc}}\}]\vec{\mathbf{L}}\text{diag}\{\mathbf{W}^{\text{dc}}\}} &\geq \text{diag}\{\vec{\mathbf{L}}\mathbf{W}^{\text{dc}}\vec{\mathbf{L}}^\top\} \\ \text{diag}\{(\vec{\mathbf{L}} - \tilde{\mathbf{L}})\mathbf{W}^{\text{dc}}(\vec{\mathbf{L}} - \tilde{\mathbf{L}})^\top\} &\geq (\vec{\mathbf{L}}\mathbf{v}^{\text{dc}} - \tilde{\mathbf{L}}\mathbf{v}^{\text{dc}})^2 \\ \text{diag}\{(\vec{\mathbf{L}} + \tilde{\mathbf{L}})\mathbf{W}^{\text{dc}}(\vec{\mathbf{L}} + \tilde{\mathbf{L}})^\top\} &\geq (\vec{\mathbf{L}}\mathbf{v}^{\text{dc}} + \tilde{\mathbf{L}}\mathbf{v}^{\text{dc}})^2 \\ \text{diag}\{\mathbf{W}^{\text{dc}}\} &\geq (\mathbf{v}^{\text{dc}})^2 \end{aligned} \quad (2.21\text{b})$$

$$\begin{aligned} \sqrt{[\mathbf{w}_{\text{ff}}^{\text{ac}}]\mathbf{w}_{\text{cc}}^{\text{ac}}} &\geq |\mathbf{w}_{\text{cf}}^{\text{ac}}|, \\ \mathbf{w}_{\text{ff}}^{\text{ac}} + \mathbf{w}_{\text{cc}}^{\text{ac}} - 2\text{real}\{\mathbf{w}_{\text{cf}}^{\text{ac}}\} &\geq |\mathbf{v}_{\text{c}}^{\text{ac}} - \mathbf{v}_{\text{f}}^{\text{ac}}|^2, \\ \mathbf{w}_{\text{ff}}^{\text{ac}} + \mathbf{w}_{\text{cc}}^{\text{ac}} + 2\text{real}\{\mathbf{w}_{\text{cf}}^{\text{ac}}\} &\geq |\mathbf{v}_{\text{c}}^{\text{ac}} + \mathbf{v}_{\text{f}}^{\text{ac}}|^2, \\ \mathbf{w}_{\text{ff}}^{\text{ac}} + \mathbf{w}_{\text{cc}}^{\text{ac}} - 2\text{imag}\{\mathbf{w}_{\text{cf}}^{\text{ac}}\} &\geq |\mathbf{v}_{\text{c}}^{\text{ac}} + i\mathbf{v}_{\text{f}}^{\text{ac}}|^2, \\ \mathbf{w}_{\text{ff}}^{\text{ac}} + \mathbf{w}_{\text{cc}}^{\text{ac}} + 2\text{imag}\{\mathbf{w}_{\text{cf}}^{\text{ac}}\} &\geq |\mathbf{v}_{\text{c}}^{\text{ac}} - i\mathbf{v}_{\text{f}}^{\text{ac}}|^2, \\ \mathbf{w}_{\text{ff}}^{\text{ac}} &\geq |\mathbf{v}_{\text{f}}^{\text{ac}}|^2, \quad \mathbf{w}_{\text{cc}}^{\text{ac}} \geq |\mathbf{v}_{\text{c}}^{\text{ac}}|^2, \end{aligned} \quad (2.21\text{c})$$

The resulting MISOCP-relaxed topology-cognizant OPF problem (2.20) with relaxed constraints (2.21a)-(2.21c) is compatible with the state-of-the-art branch-and-bound solvers which enables the search for binary variables.

2.3.4 Penalization

The convex relaxation given in (2.21a)-(2.21c) may sometimes lead to an inexact solution with infeasible points for the original nonconvex formulation. In order to ensure that (2.20t)-(2.20v) are satisfied, we incorporate a penalty function of the form

$$\rho_{\check{\mathbf{v}}^{\text{dc}}, \check{\mathbf{v}}_c^{\text{ac}}, \check{\mathbf{v}}_f^{\text{ac}}, \check{\mathbf{i}}^{\text{ac}}}(\mathbf{W}^{\text{dc}}, \mathbf{v}^{\text{dc}}, \mathbf{w}_{\text{cc}}^{\text{ac}}, \mathbf{v}_c^{\text{ac}}, \mathbf{w}_{\text{ff}}^{\text{ac}}, \mathbf{v}_f^{\text{ac}}, \mathbf{t}^{\text{ac}}, \mathbf{i}^{\text{ac}}) = \eta^{\text{dc}}(\text{tr}\{\mathbf{W}^{\text{dc}}\} - 2(\check{\mathbf{v}}^{\text{dc}})^\top \mathbf{v}^{\text{dc}} + \|\check{\mathbf{v}}^{\text{dc}}\|_2^2) + \quad (2.22a)$$

$$\eta_c^{\text{ac}}(\mathbf{1}_{|\mathcal{N}|}^\top \mathbf{w}_{\text{cc}}^{\text{ac}} - (\check{\mathbf{v}}_c^{\text{ac}})^* \mathbf{v}_c^{\text{ac}} - (\mathbf{v}_c^{\text{ac}})^* \check{\mathbf{v}}_c^{\text{ac}} + \|\check{\mathbf{v}}_c^{\text{ac}}\|_2^2) + \quad (2.22b)$$

$$\eta_f^{\text{ac}}(\mathbf{1}_{|\mathcal{N}|}^\top \mathbf{w}_{\text{ff}}^{\text{ac}} - (\check{\mathbf{v}}_f^{\text{ac}})^* \mathbf{v}_f^{\text{ac}} - (\mathbf{v}_f^{\text{ac}})^* \check{\mathbf{v}}_f^{\text{ac}} + \|\check{\mathbf{v}}_f^{\text{ac}}\|_2^2) + \quad (2.22c)$$

$$\eta_i^{\text{ac}}(\mathbf{1}_{|\mathcal{N}|}^\top \mathbf{t}^{\text{ac}} - (\check{\mathbf{i}}^{\text{ac}})^* \mathbf{i}^{\text{ac}} - (\mathbf{i}^{\text{ac}})^* \check{\mathbf{i}}^{\text{ac}} + \|\check{\mathbf{i}}^{\text{ac}}\|_2^2) \quad (2.22d)$$

into the objective of convex relaxation, where $(\check{\mathbf{v}}^{\text{dc}}, \check{\mathbf{v}}_c^{\text{ac}}, \check{\mathbf{v}}_f^{\text{ac}}, \check{\mathbf{i}}^{\text{ac}}) \in \mathbb{R}^{|\mathcal{N}|} \times \mathbb{R}^{|\mathcal{C}|} \times \mathbb{R}^{|\mathcal{C}|} \times \mathbb{R}^{|\mathcal{C}|}$ can be any arbitrary initial point. As shown in [50, 51], the proper selection of penalty coefficients $\eta^{\text{dc}}, \eta_c^{\text{ac}}, \eta_f^{\text{ac}}, \eta_i^{\text{ac}} \geq 0$ guarantees the recovery of near-optimal feasible points. In the following section, we show that the simple choice of parameters

$$\check{\mathbf{v}}^{\text{dc}} = \check{\mathbf{v}}_c^{\text{ac}} = \check{\mathbf{v}}_f^{\text{ac}} = \check{\mathbf{i}}^{\text{ac}} = 0, \quad (2.23a)$$

$$\eta^{\text{dc}} = 10^{-4}, \quad \eta_i^{\text{ac}} = 10^{-5}, \quad \eta_c^{\text{ac}} = \eta_f^{\text{ac}} = 0, \quad (2.23b)$$

can reliably solve the original non-convex problem in practice.

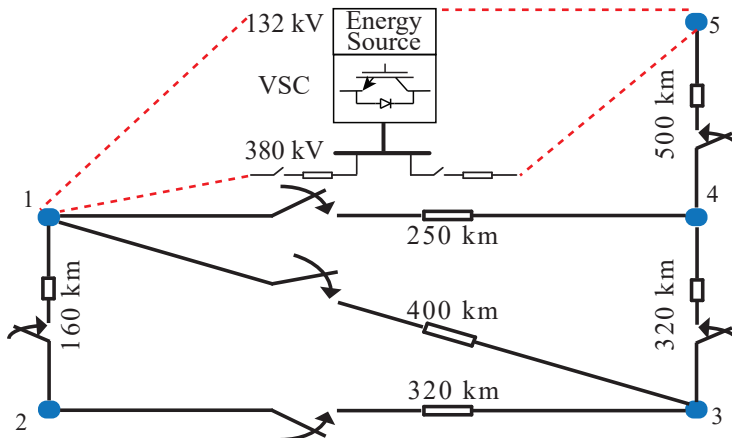


Figure 3: The modified CIGRE B4 DC grid equipped with line switches. DC cable resistance for $\pm/400$ kv is $0.0095 \Omega/\text{km}$.

2.4 Case Studies

2.4.1 System Setup

The modified CIGRE B4 DC grid benchmark [52], equipped with switches to open/close transmission lines, is illustrated in Figure 3. This MTDC grid is emulated in a HIL platform, with two dSPACE DS1202 MicroLabBoxes to implement droop controllers for individual VSCs, and two Typhoon HIL604 units to emulate transmission lines and VSCs, as depicted in Figure 4. The TCP/IP link between Typhoon HIL/MATLAB/dSPACE MicroLabBoxes shares the load, set-point information, and the status of switching devices at every five second. A PC with 16-core, Xeon processor, and 256 GB RAM solves the proposed algorithm using the CVX v2.1 [53], and the optimization solver GUROBI v8.0.1 [54]. In the following studies, four time intervals, $[0\text{s}, 120\text{s}]$, $[120\text{s}, 220\text{s}]$, $[220\text{s}, 320\text{s}]$, and $[320\text{s}, 420\text{s}]$, are considered.

The rated power of each VSC is 1200 MW. Variable loads are attached to bus 1 and bus 4. The bounds on power constraints for AC and DC sides are $p_{\min_k}^{\text{dc}} = p_{\min_k}^{\text{ac}} = -1200$ MW and $p_{\max_k}^{\text{dc}} = p_{\max_k}^{\text{ac}} = 1200$ MW for every VSC at bus $k \in \mathcal{N}$. The loss coefficients in (2.1) are $a_k = 2.65 \times 10^{-5}$, $b_k = 3.7 \times 10^{-5}$, and $c_k = 3.6 \times 10^{-5}$

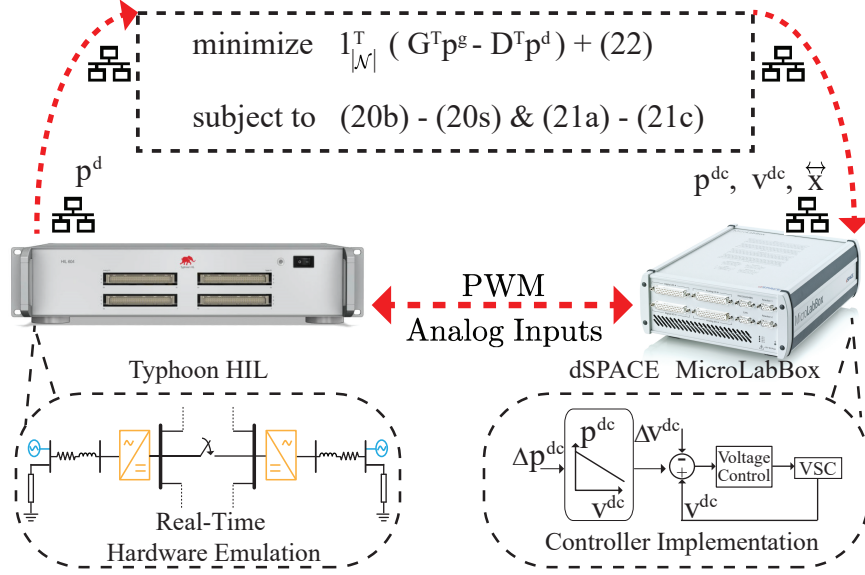


Figure 4: Topology-cognizant OPF testbed on a real-time HIL platform has hardware emulation (Typhoon HIL), controller implementation (dSPACE), and TCP/IP communication link.

for every VSC at bus $k \in \mathcal{N}$. The converter constant and nominal apparent power in (2.5) are $m_b = 0.6$ and $|\bar{s}^{ac}| = 1.2$ pu, respectively. Phase-reactor parameters in (2.5) are $r_k = 2.5 \times 10^{-6}$ and $x_k = 4 \times 10^{-4}$ for every $k \in \mathcal{N}$. VSC parameters are $i_{c_{\max}}^{ac} = 1.0526$ and $v_{c_{\max}}^{ac} = 1.05$. The maximum modulation factor in (2.2) is $m = 1$. The voltage bounds are 0.94 pu (352.7 kV) and 1.06 pu (402.8 kV). The lines are rated at $\vec{f}_{l_{\max}} = 0.3$ pu (300 MW) for every $l \in \mathcal{L}$. The big-M value in (2.19) and (2.20) is $M = 500$. Safety constraint coefficients in (2.20s) are $\mu_k = 10\%$ and $\kappa_k = 5\%$ for every VSC at bus $k \in \mathcal{N}$. Penalty coefficients in (2.22) are chosen from (2.23). A solution is regarded feasible when the maximum mismatch between the right and left sides of inequalities in (2.21a)-(2.21c) is less than 10^{-6} .

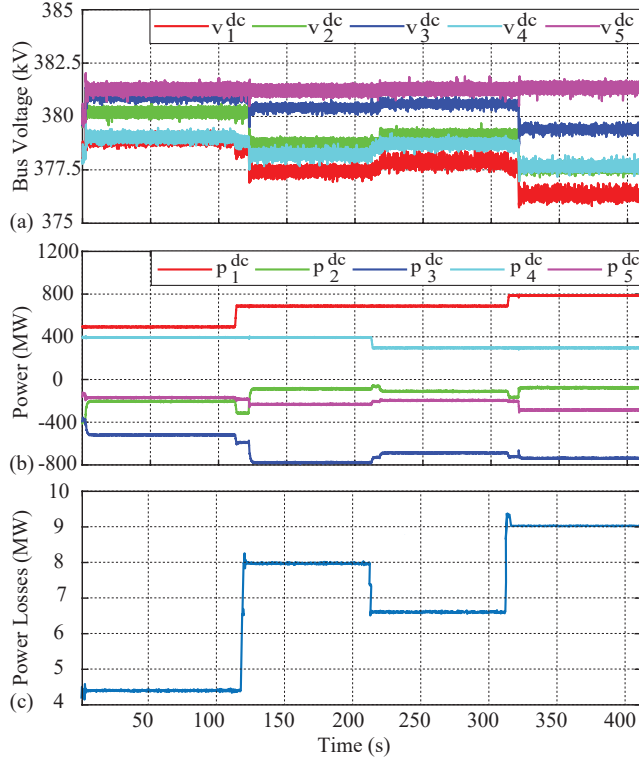


Figure 5: MTDC operation with droop control under varying load: (a) DC side voltage variation, (b) DC side power variation, and (c) Total power losses.

2.4.2 MTDC Grid Operation with Static OPF

Static OPF refers to the problem (2.20) with a connected grid, $\vec{x}_{l_{\min}} = \vec{x}_{l_{\max}} = 1$ for every $l \in \mathcal{L}$. If OPF results do not update the set-points of the local droop controller, they arrive at a feasible operating condition shown in Figure 5. The primary aim of a local controller is to maintain stable operation of a VSC in meeting the load demand as well as voltage-power tracking. Optimal operation of the MTDC grid cannot be accomplished with the local controllers alone and requires upper-level optimizer to reduce the total loss. The total loss obtained via local controllers and static OPF, Figure 6, are given in Table 1. With the implementation of the static OPF result, around 10% reduction in loss is reported compared to results obtained

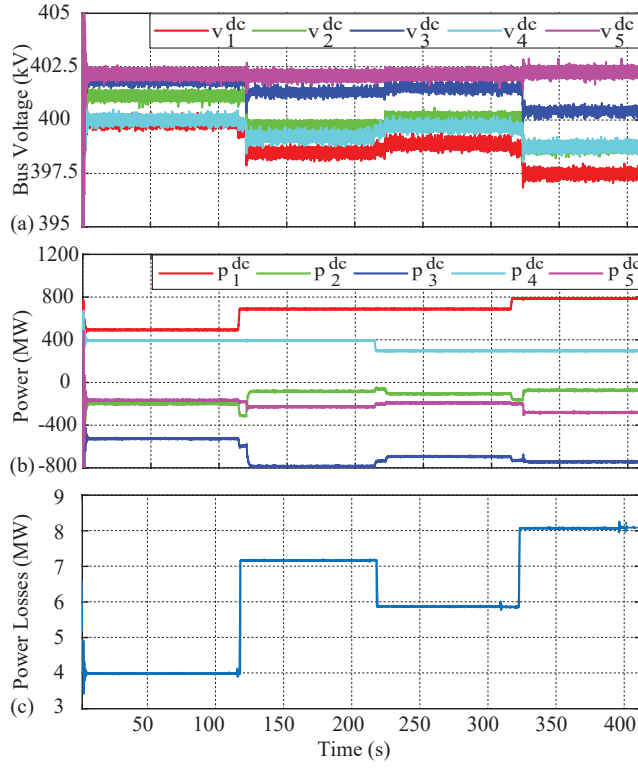


Figure 6: MTDC operation with static OPF under varying load: (a) DC side voltage variation, (b) DC side power variation, and (c) Total power losses.

via local droop controllers alone. The average computation time to solve the static OPF and update droop set-points is 1.4 s.

2.4.3 MTDC Grid Operation with Topology-cognizant OPF

The formulation (2.20), with and without the constraints in (2.20s), finds the optimal grid topology with the goal of reducing the total loss. The outcome of topology-cognizant OPF problem without voltage safety limits in (2.20s) further reduces the total loss by 4.79%, 13.54%, 12.80%, and 12.00% for the four time intervals as compared to the static OPF scenarios. Based on the outcome of (2.20) (except (2.20s)), \vec{x}_{2-3} is always disconnected, while \vec{x}_{1-4} is disconnected only during [0s, 120s] time interval. Even though the total loss is further reduced, the voltage safety limits are violated at

Table 1: Total Losses with different Approaches (MW)

Time interval (s) \ Method	0-120	120-220	220-320	320-420
Local droop controller	4.40	8.00	6.50	9.00
Static OPF	3.97	7.16	5.86	8.08
Topology-cognizant OPF without the safety constraints (2.20) without (2.20s)	3.78	6.19	5.11	7.11
Topology-cognizant OPF with the safety constraints (2.20) with (2.20s)	3.80	6.22	5.14	7.13

bus 5 due to load fluctuations and the computation time involved in updating droop set-points, see Figure 7 (a). Additional safety constraints in (2.20s) mitigate any voltage violation in response to power fluctuations in between two droop set-points updates as shown in Figure 8 (a). This safer operation comes with a slightly higher total loss compared to the case ignoring (2.20s); Nevertheless, it still offers remarkable reduction in total loss as compared to the static OPF. The total loss obtained by the topology-cognizant OPF with and without the constraints in (2.20s) are given in Table 1. Total losses for different loading profiles are about 0.42%, 0.57%, 0.52%, and 0.65% of the total load demand for the four time intervals, respectively. The converter losses obtained from convex relaxation approach are about 7.31%, 4.71%, 5.65%, and 4.18% of the total loss in corresponding intervals. Updating droop set-points, that are sent to VSCs every five second, takes around 2.5 s.

2.4.4 Deployment on Larger Networks

The proposed algorithm in (2.20) is applied to several modified IEEE benchmarks of various sizes. First, we study the static OPF problem, where $\vec{x}_{l_{\min}} = \vec{x}_{l_{\max}} = 1$

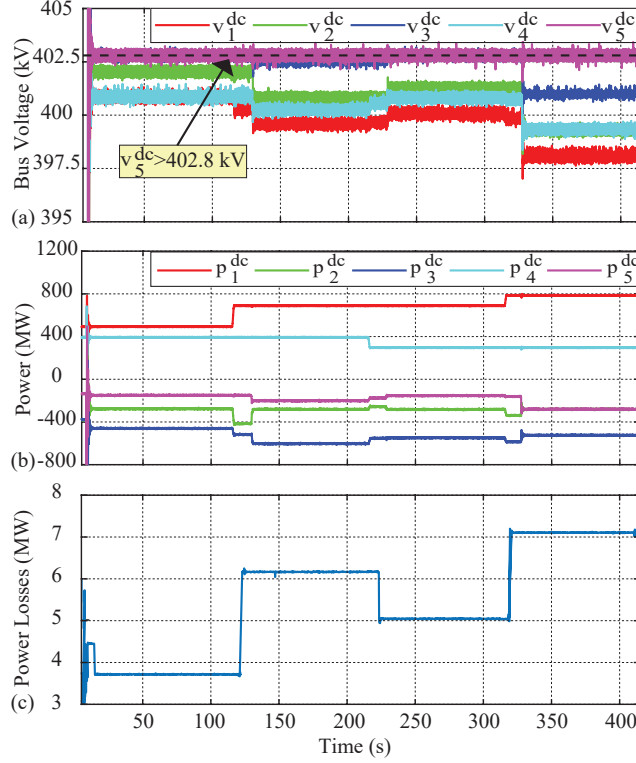


Figure 7: MTDC operation with topology-cognizant OPF disregarding voltage safety constraints in (2.20s). The variations in load/generation have DC voltage at bus 5 violate the safety limit: (a) DC side voltage variation (dotted line shows the safety limit, $v_{\max}^{\text{dc}} = 402.8 \text{ kV}$), (b) DC side power variation, and (c) Total power losses.

for every $l \in \mathcal{L}$, for IEEE 14, 30, and 57-bus benchmarks, that have been modified to MTDC networks by adding VSCs to every bus and switches to every transmission line, and making these lines resistive. Total losses obtained are 0.00550 pu, 0.00860 pu, and 0.02030 pu, respectively. The computation times are roughly 1.59, 3.92, and 10.21 s, respectively. We then study the topology-cognizant problem where, for the modified IEEE 14, 30, and 57-bus benchmarks, 4 out of 20, 13 out of 41, and 14 out of 80 transmission lines are disconnected, respectively. The total losses, respectively, are reduced to 0.00538 pu, 0.00813 pu, and 0.0168 pu, which are 2.18%, 5.46%, 17.24% less compared to those acquired using the static OPF. The status of transmission

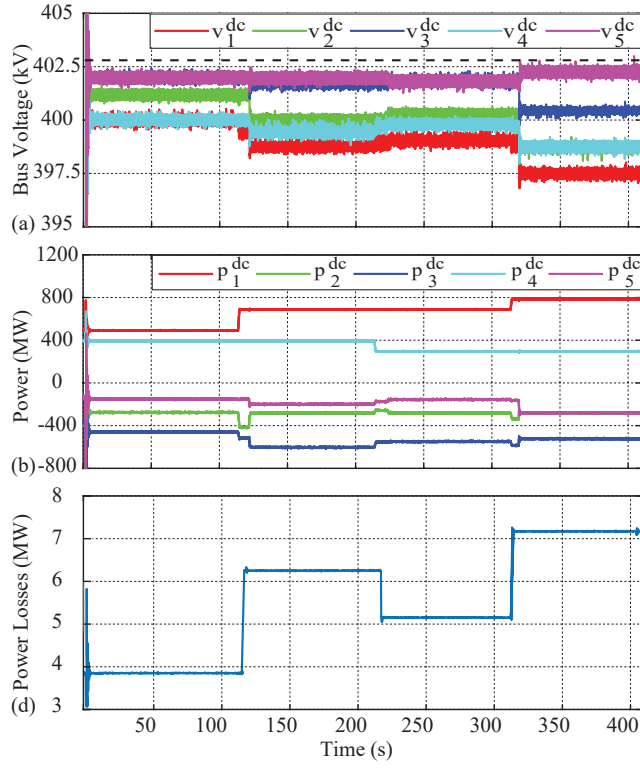


Figure 8: MTDC operation with topology-cognizant OPF considering the voltage safety constraints in (2.20s): (a) DC side voltage variation (dotted line shows the safety limit, $v_{\max}^{dc} = 402.8$ kV), (b) DC side power variation, and (c) Total power losses.

lines, voltage and power levels at each bus for the modified IEEE 14, 30, and 57-bus benchmarks take 18, 42, and 136s, respectively, on average, to be determined.

2.5 Summary

This chapter offers a convex optimization framework to solve the grid topology-cognizant OPF problem for MTDC grids. It provides local voltage and power set-points for droop controllers of VSCs as well as the operational status of transmission lines. Additional constraints, that sustain safe operation in response to the power fluctuation in between two droop updates, are integrated into the proposed formulation. The resulting formulation has computational difficulties due to the non-convex

power balance, flow and converter loss equations as well as the inclusion of binary decision variables. Convex relaxation methods are utilized to transform this problem into a tractable model so that it can be executed with off-the-shelf solvers. Experimental and numerical results validate the practicability and efficacy of the proposed approach.

OBSERVATION OF STATE AND TOPOLOGY IN DC NETWORKS

T. Altun, R. Madani and A. Davoudi, "Observation of State and Topology in DC networks," IEEE Transactions on Power Systems, Revision submitted in June 2020, (Manuscript ID: TPWRS-01084-2019.R3).

CHAPTER 3

OBSERVATION OF STATE AND TOPOLOGY IN DC NETWORKS

Direct current (DC) networks are gaining prominence with the increasing penetration of DC loads, storages, and sources, since they offer improved efficiency in conversion/distribution over alternating current (AC) networks. For static distribution topologies, estimation techniques can extract the system state to be used in network analysis, control, optimization, or diagnostic under normal, emergency, or restorative operations [55]. The most recent topology information is needed to meaningfully carry out the state estimation process; any error or misconfiguration in the assumed topology could result in inappropriate control decisions [56, 57]. Incorporating statuses of the lines, that collectively describe the overall network topology, into the state estimation process is challenging as they introduce binary variables [58, 59]. Moreover, converter-populated DC networks might employ fewer sensors due to cost, security, or privacy concerns, leading to low-observability conditions.

The state estimation process is conventionally expressed as a nonlinear least-squares problem [9]. The weighted least-squares (WLS) estimation criterion has been employed in practice to filter out Gaussian measurement noise with certain statistical properties [10, 11]. As WLS is susceptible to gross measurement errors, other gross error detection and identification methods have been proposed to perform accurate state estimation [12, 13, 14, 15, 11]. Given their non-convex problem formulation, the Gauss-Newton algorithm is sensitive to the initial points, and might converge to local minima [16]. Convex relaxation methods can either directly solve the estimation problem [17] or provide an initial guess for the Newton's method [18]. Convergence

guarantees for the estimation process using convex relaxation techniques are given in [19]. With measurement redundancy, incorporating penalty terms in the formulation of the objective function can help cleansing noise and bad data [20, 21, 22]. These techniques, however, assume a fixed network topology.

Topology identification is either a prerequisite to the estimation process, or should be considered concurrently. The combined problem can be handled using a Gauss-Newton, e.g., generalized state estimation (GSE) [58], or convex relaxation methods[59]. Inverse power flow formulation can describe the network topology through a nodal admittance matrix[60]. These studies usually assume imperfect but highly-redundant measurement. Low-observability condition refers to the sparse sensor that results in an under-determined system. With proper placement, fewer sensors might be needed to observe the network [61, 62]. [63] finds the required minimal set of measurement so that an unobservable network can become observable. Alternative non-iterative numerical solutions are proposed in [64, 65]. However, even an observable network may temporarily become unobservable due to topological changes or failure in the communication. The sensor placement procedures, considering topology changes or communication failures, are developed in [66, 67, 68]. Additional sensors placement [69] or pseudo measurements from existing sensors data [70] come with an additional cost, computational burden, or estimation errors [71].

The matrix completion method, that offers a solution to an under-determined system, has been applied to distribution networks with poor sensors installation [72, 73]. While the joint state estimation and topology identification problem has been studied for AC networks [59], its solution has not yet been elaborated under low-observability conditions [74, 75, 76, 71, 77]. Moreover, state estimation and topology identification of DC networks are rare in the literature [78, 79, 80], and have not even considered the observability conditions.

We leverage the physical properties of DC networks to develop a joint estimation and topology identification algorithm using a limited number of measurement. We formulate this as a non-convex mixed-binary problem, develop a non-convex nuclear norm estimator, and address this non-convexity by using two inertia terms. The presence of zero injection buses (i.e., a bus with no load or converter) is used to strengthen the convex relaxation and decrease the number of required sensors. The resulting formulation does not rely on prior knowledge of unmonitored line-statuses, current, or power flow measurements that could infer topology information. The devised convex optimization framework is robustified against noise by upgrading to a penalized convex program. This formulation is in a generic form, and can be solved with various numerical solvers.

The rest of this chapter has the following organization: Section 3.1 discusses the preliminaries. Section 3.2 presents the joint state estimation and topology identification problem for noiseless measurements. This non-convex problem is transformed into convex surrogate using two inertia terms and, then, extended to accommodate noisy measurements. In Section 3.3, the resulting state estimation and topology identification solution is verified through numerical and experimental benchmarks. Section 3.4 finalizes the chapter.

3.1 Notations and Terminologies

3.1.1 Notations

Throughout this chapter, bold uppercase (\mathbf{A}) and lowercase letters (\mathbf{a}) refer to the matrices and vectors, respectively. The symbols $\mathbf{1}_n$ and $\mathbf{0}_n$ represent $n \times 1$ vectors of ones and zeros, respectively. $\mathbf{0}_{n \times m}$ refers to a zero matrix of size $n \times m$. $\mathbf{I}_{n \times n}$ indicates an identity matrix of size $n \times n$. The symbol \mathbb{R} defines the sets of real

numbers. The entries of a matrix are presented by indices (i, j) . $(\cdot)^\top$ indicates the transpose of a matrix. $|\cdot|$ refers the cardinality of a set or the absolute value of a vector/scalar. $Tr(\cdot)$ shows to the trace of a matrix. $\|\cdot\|_2$ stands for the euclidean norm of its argument vector. $\|\cdot\|_*$ represents the nuclear norm of its argument matrix. A vector composed from diagonal entries of a matrix is shown by $\text{diag}\{\cdot\}$. $\mathbf{X} \succeq 0$ indicates a positive semi-definite matrix.

3.1.2 Terminologies

On a DC network, distribution lines are resistive and DC-DC power electronics converters interface energy resources to the distribution network as demonstrated in Figure 9. DC network can be articulated using a directed graph, $\mathcal{H} = (\mathcal{N}, \mathcal{L})$ with \mathcal{N} and \mathcal{L} sets, respectively, representing buses and lines. Every bus can accommodate a DC-DC converter, a resistive load, and/or a constant power load.

Define the pair $\vec{\mathbf{L}}, \tilde{\mathbf{L}} \in \{0, 1\}^{|\mathcal{L}| \times |\mathcal{N}|}$, respectively, as the *from* and *to* line incidence matrices. $\vec{\mathbf{L}}_{l,i} = 1$ if the line l starts at bus i . $\tilde{\mathbf{L}}_{l,i} = 1$ implies that the line l ends at bus i . The conductance of a line $l \in \mathcal{L}$ is g_l , with $\mathbf{g} \in \mathbb{R}^{|\mathcal{L}|}$ as the line conductance vector. $\mathbf{G} \in \mathbb{R}^{|\mathcal{N}| \times |\mathcal{N}|}$ is the bus conductance matrix. $\vec{\mathbf{G}}$ and $\tilde{\mathbf{G}} \in \mathbb{R}^{|\mathcal{L}| \times |\mathcal{N}|}$ are, respectively, the *from* and *to* line conductance matrices.

Let n define the number of buses, i.e., $n = |\mathcal{N}|$. $\mathbf{v} = [v_1, v_2, \dots, v_n]^\top$ is the vector of voltages with $v_k \in \mathbb{R}$ as the voltage at bus $k \in \mathcal{N}$. Let $i_k \in \mathbb{R}$ refer to the current-injection at bus $k \in \mathcal{N}$, while $\mathbf{i} = [i_1, i_2, \dots, i_n]^\top$ is the corresponding vector. Given a line $l \in \mathcal{L}$, there are two current signals, $\vec{i}_l \in \mathbb{R}$ and $\tilde{i}_l \in \mathbb{R}$, entering the line via its *from* and *to* ends, respectively. $\vec{\mathbf{i}} = [\vec{i}_1, \vec{i}_2, \dots, \vec{i}_{|\mathcal{L}|}]^\top$ and $\tilde{\mathbf{i}} = [\tilde{i}_1, \tilde{i}_2, \dots, \tilde{i}_{|\mathcal{L}|}]^\top$ are the vectors of corresponding composites. We assume there is no interlinking converter in the network; hence $\vec{\mathbf{i}} = -\tilde{\mathbf{i}}$. \hat{v}_k , \hat{i}_k , and \hat{x}_l denote the measured voltage as well as the current-injection at bus $k \in \mathcal{N}$, and the status of line $l \in \mathcal{L}$, respectively. v_k and

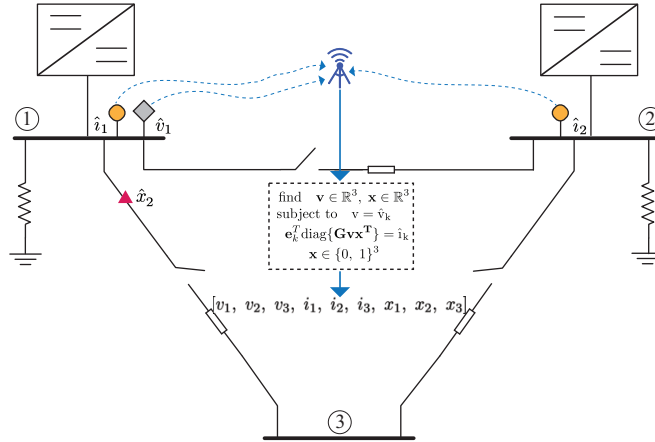


Figure 9: Three bus DC distribution network is equipped with sensors at buses 1 and 2 and the line between buses 1-3 to collect data $(\hat{v}_1, \hat{x}_2, \hat{i}_1, \hat{i}_2)$. Optimizer jointly performs state estimation and topology identification using these limited measurements, and infers unknown voltage, v_2, v_3 , and statuses of the lines, x_1, x_3 .

x_l refer to the estimated voltage at bus $k \in \mathcal{N}$, and the identified status of the line $l \in \mathcal{L}$, respectively.

3.2 Joint State Estimation and Topology Identification

3.2.1 Problem Formulation

We will exploit the power flow equations of a DC network to express this problem as a constrained minimization program. The available measurements are: (i) voltage values at some of the randomly-chosen buses, (ii) current-injection values at some of the randomly-chosen buses, and (iii) some of the line statuses. The Ohm's law dictates that the current flow from both sides of each line, and the current-injection at each bus, can be respectively represented as

$$\vec{i} = \text{diag}\{\vec{G} \mathbf{v} \mathbf{x}^\top\}, \quad \vec{\bar{i}} = -\vec{i}, \quad (3.1)$$

$$\mathbf{i} = \vec{\mathbf{L}}^\top \vec{i} + \vec{\mathbf{L}}^\top \vec{\bar{i}}. \quad (3.2)$$

Note that (3.1) and (3.2) hold true unless there is an interlinking converter on the line.

The state estimation and topology identification algorithm simultaneously finds the voltage vector, \mathbf{v} , and the line-status vector, \mathbf{x} , while satisfying all the measurement equations

$$\text{find} \quad \mathbf{v} \in \mathbb{R}^{|\mathcal{N}|}, \mathbf{x} \in \mathbb{R}^{|\mathcal{L}|} \quad (3.3a)$$

$$\text{subject to} \quad v_k = \hat{v}_k \quad \forall k \in \mathcal{S}_v \quad (3.3b)$$

$$\mathbf{e}_k^\top \text{diag}\{\mathbf{G}\mathbf{v}\mathbf{x}^\top\} = \hat{i}_k \quad \forall k \in \mathcal{S}_i \quad (3.3c)$$

$$\mathbf{x}^{\text{lb}} \leq \mathbf{x} \leq \mathbf{x}^{\text{ub}} \quad (3.3d)$$

$$\mathbf{x} \in \{0, 1\}^{|\mathcal{L}|} \quad (3.3e)$$

where $\{\mathbf{e}_1, \dots, \mathbf{e}_N\}$ are the basis vectors in \mathbb{R}^n . Here, measurement equations refer to the nonlinear relations between sensor outputs and state variables as in (3.3c). For x^{lb} and x^{ub} , the conditional expressions can be given as

$$\begin{aligned} x_l^{\text{lb}} = x_l^{\text{ub}} = 1, & \quad \text{if line } l \in \mathcal{L} \text{ is known to be connected,} \\ x_l^{\text{lb}} = x_l^{\text{ub}} = 0, & \quad \text{if line } l \in \mathcal{L} \text{ is known to be disconnected,} \\ x_l^{\text{lb}} = 0, \quad x_l^{\text{ub}} = 1, & \quad \text{if the status of line } l \text{ is undetermined.} \end{aligned}$$

Here, x_l^{lb} and x_l^{ub} refer to the lower and upper bound of line statuses.

Equation (3.3b) enforces the voltage value to be equal to the sensor measurement if the corresponding bus is equipped with a voltage sensor (i.e., *a monitored bus*). v_k and \hat{v}_k denote voltage values to be estimated and to be measured for every bus

$k \in \mathcal{S}_v$, respectively. \mathcal{S}_v denotes the set of voltage measurements. Equality constraint (3.3c) aims to find the voltage value and line status that fit the corresponding input value, \hat{i}_k , from a set of current-injection measurements, \mathcal{S}_i . Problem (3.3) is non-convex because of vector multiplication in $\mathbf{v}\mathbf{x}^\top$ and the binary variables accounting for the statuses of the lines. Next, we offer a convex reformulation alternative.

3.2.2 Convexification of the Problem Formulation

We introduce the following convex optimization problem using the auxiliary variable \mathbf{A} accounting for $\mathbf{v}\mathbf{x}^\top$

$$\begin{aligned} \underset{\substack{\mathbf{A} \in \mathbb{R}^{|\mathcal{N}| \times |\mathcal{L}|} \\ \mathbf{v} \in \mathbb{R}^{|\mathcal{N}|} \\ \mathbf{x} \in \mathbb{R}^{|\mathcal{L}|}}}{\text{minimize}} \quad & \|\mathbf{M}^{\frac{1}{2}}(\mathbf{A} - \mathbf{v}\mathbf{x}^\top)\mathbf{N}^{\frac{1}{2}}\|_* + \|\mathbf{v} - \mathbf{v}_0\|_M^2 + \|\mathbf{x} - \mathbf{x}_0\|_N^2 \end{aligned} \quad (3.4a)$$

$$\text{subject to} \quad v_k = \hat{v}_k \quad \forall k \in \mathcal{S}_v \quad (3.4b)$$

$$\mathbf{e}_k^\top \text{diag}\{\mathbf{G}\mathbf{A}\} = \hat{i}_k \quad \forall k \in \mathcal{S}_i \quad (3.4c)$$

$$\mathbf{e}_k^\top \mathbf{A} = \hat{v}_k \mathbf{x}^\top \quad \forall k \in \mathcal{S}_v \quad (3.4d)$$

$$\mathbf{A}\mathbf{d}_l^\top = \mathbf{v}\hat{x}_l \quad \forall l \in \mathcal{S}_x \quad (3.4e)$$

$$\mathbf{x}^{\text{lb}} \leq \mathbf{x} \leq \mathbf{x}^{\text{ub}} \quad (3.4f)$$

$$\mathbf{v}(\mathbf{x}^{\text{lb}})^\top \leq \mathbf{A} \leq \mathbf{v}(\mathbf{x}^{\text{ub}})^\top \quad (3.4g)$$

where $\mathbf{M} \succ 0$ and $\mathbf{N} \succ 0$ are arbitrary basis matrices to be designed later. $\{\mathbf{d}_1, \dots, \mathbf{d}_L\}$ are the standard basis vectors in $\mathbb{R}^{|\mathcal{L}|}$. \mathbf{v}_0 and \mathbf{x}_0 are the initial guesses for the elements of the voltage and the line-status vectors. They are chosen as the nominal voltage value, $\mathbf{1}$ per-unit and $\mathbf{1}_n$, respectively, to satisfy flat start operating conditions and imply a fully-connected network.

Notice that the bi-linear term $\mathbf{v}\mathbf{x}^\top$ in (3.3c) is replaced by \mathbf{A} in (3.4c) and, therefore, we are dealing with a linear constraint. The nuclear norm term, $\|\mathbf{A}-\mathbf{v}\mathbf{x}^\top\|_*$, implicitly imposes the non-convex equality $\mathbf{A} \triangleq \mathbf{v}\mathbf{x}^\top$ by penalizing the difference.

Proposition 1. *Let \mathbf{v}^* and \mathbf{x}^* be the solution to (3.3), and define $\mathbf{A}^* \triangleq \mathbf{v}^*\mathbf{x}^{*\top}$. The constraints in (3.4d), (3.4e), and (3.4g) are valid for \mathbf{A} , \mathbf{v} , and \mathbf{x}^\top .*

Proof. Consider arbitrary voltage and line-status vectors \mathbf{v} and \mathbf{x} , respectively. Let \mathbf{v}^* and \mathbf{x}^* be the solutions to (3.3), when voltage and current-injection measurements are chosen from the sets \mathcal{S}_v and \mathcal{S}_i , respectively. Constraint (3.4d) becomes

$$\mathbf{e}_k^\top \mathbf{A}^* = \mathbf{e}_k^\top \mathbf{v}^* \mathbf{x}^{*\top} = v_k \mathbf{x}^{*\top} \quad \forall k \in \mathcal{S}_v. \quad (3.5)$$

This implies that the constraint (3.4d) holds for any given $k \in \mathcal{N}$. For every $l \in \mathcal{L}$, (3.4e) leads to the following equality

$$\mathbf{A}^* \mathbf{d}_l^\top = \mathbf{v}^* \mathbf{x}^{*\top} \mathbf{d}_l^\top = v x_l \quad \forall l \in \mathcal{S}_x, \quad (3.6)$$

where it shows that $v x_l$ becomes equivalent to (3.4e). Similarly, for every $k \in \mathcal{N}$ and $l \in \mathcal{L}$, (3.4g) becomes

$$x_l^{\text{lb}} \leq x_l^* \leq x_l^{\text{ub}}, \quad (3.7a)$$

$$\Rightarrow v_k^* x_l^{\text{lb}} \leq v_k^* x_l^* \leq v_k^* x_l^{\text{ub}}, \quad (3.7b)$$

$$\Rightarrow v_k^* x_l^{\text{lb}} \leq A_{kl}^* \leq v_k^* x_l^{\text{ub}}. \quad (3.7c)$$

Note that (3.4g), (3.7b), and (3.7c) are equivalent. Equations (3.5), (3.6), and (3.7) complete the proof for the valid inequalities in (3.4).

□

Remark 1. Observe that the nuclear norm term in (3.4a), $\|\mathbf{A}-\mathbf{v}\mathbf{x}^\top\|_*$ is non-convex. The inertia terms $\|\mathbf{v}-\mathbf{v}_0\|_{\mathbf{M}}^2$ and $\|\mathbf{x}-\mathbf{x}_0\|_{\mathbf{N}}^2$ are added to convexify the overall objective function. This is formally stated by the following theorem.

Remark 2. The presence of matrices \mathbf{M} and \mathbf{N} indicates that the choice of basis can be arbitrary. We will demonstrate how \mathbf{M} and \mathbf{N} can boost the convergence rate of the proposed approach. A penalty term induced by a physical quantity, such as loss, can help address the non-convexity.

Theorem 1. The function $f : \mathbb{R}^{n \times l} \times \mathbb{R}^n \times \mathbb{R}^l \rightarrow \mathbb{R}$, defined as

$$f(\mathbf{A}, \mathbf{v}, \mathbf{x}) \triangleq \|\mathbf{M}^{\frac{1}{2}}(\mathbf{A}-\mathbf{v}\mathbf{x}^\top)\mathbf{N}^{\frac{1}{2}}\|_* + \|\mathbf{v}-\mathbf{v}_0\|_{\mathbf{M}}^2 + \|\mathbf{x}-\mathbf{x}_0\|_{\mathbf{N}}^2, \quad (3.8)$$

is convex.

Proof. Define new variables $\mathbf{B} \triangleq \mathbf{M}^{\frac{1}{2}}\mathbf{A}\mathbf{N}^{\frac{1}{2}}$, $\mathbf{s} \triangleq \mathbf{M}^{\frac{1}{2}}\mathbf{v}$, and $\mathbf{r} \triangleq \mathbf{N}^{\frac{1}{2}}\mathbf{x}$. It suffices to show that the following function is convex:

$$g(\mathbf{B}, \mathbf{s}, \mathbf{r}) \triangleq \|\mathbf{B}-\mathbf{s}\mathbf{r}^\top\|_* + \|\mathbf{s}\|_2^2 + \|\mathbf{r}\|_2^2. \quad (3.9)$$

According to triangle inequality we have:

$$g(\mathbf{A}, \boldsymbol{\nu}, \boldsymbol{\xi}) - \theta g(\mathbf{B}_1, \mathbf{s}_1, \mathbf{r}_1) - (1-\theta)g(\mathbf{B}_2, \mathbf{s}_2, \mathbf{r}_2) \leq 0, \quad (3.10)$$

where \mathbf{A} , $\boldsymbol{\nu}$, and $\boldsymbol{\xi}$ are

$$\mathbf{A} = \theta\mathbf{B}_1 + (1-\theta)\mathbf{B}_2, \quad (3.11a)$$

$$\boldsymbol{\nu} = \theta\mathbf{s}_1 + (1-\theta)\mathbf{s}_2, \quad (3.11b)$$

$$\boldsymbol{\xi} = \theta\mathbf{r}_1 + (1-\theta)\mathbf{r}_2. \quad (3.11c)$$

The inequality in (3.10) can be expanded as

$$\begin{aligned}
& \|\mathbf{A} - [\boldsymbol{\nu}][\boldsymbol{\xi}]^\top\|_* - \theta \|\mathbf{B}_1 - \mathbf{s}_1 \mathbf{r}_1^\top\|_* - (1 - \theta) \|\mathbf{B}_2 - \mathbf{s}_2 \mathbf{r}_2^\top\|_* \\
& \leq \|\theta \mathbf{s}_1 \mathbf{r}_1^\top + (1 - \theta) \mathbf{s}_2 \mathbf{r}_2^\top - [\boldsymbol{\nu}][\boldsymbol{\xi}]^\top\|_* \\
& = \theta(1 - \theta) \|\mathbf{s}_1 - \mathbf{s}_2\|_2 \|\mathbf{r}_1 - \mathbf{r}_2\|_2.
\end{aligned} \tag{3.12}$$

Further simplification of (3.12) leads to

$$\begin{aligned}
& \|\boldsymbol{\nu}\|_2^2 + \|\boldsymbol{\xi}\|_2^2 - \theta(\|\mathbf{s}_1\|_2^2 + \|\mathbf{r}_1\|_2^2) - (1 - \theta)(\|\mathbf{s}_2\|_2^2 + \|\mathbf{r}_2\|_2^2) \\
& = -\theta(1 - \theta)[\|\mathbf{s}_1 - \mathbf{s}_2\|_2^2 + \|\mathbf{r}_1 - \mathbf{r}_2\|_2^2],
\end{aligned} \tag{3.13}$$

which completes the proof of *Theorem 1*. \square

3.2.3 The Choice of Basis Matrices

The original problem in (3.3) has been expressed as a convex optimization problem (3.4) with basis matrices \mathbf{M} and \mathbf{N} . These basis matrices should be chosen properly such that the solution to (3.4) satisfies the problem in (3.3). Inspired by [22], matrix \mathbf{M} is chosen to represent the network's total power loss.

Power flow on a line $l \in \mathcal{L}$ can be calculated for the two neighboring buses $(i, j) \in \mathcal{N}$ as

$$\vec{p}_l = v_i(v_i - v_j)g_l x_l, \tag{3.14a}$$

$$\tilde{p}_l = v_j(v_j - v_i)g_l x_l, \tag{3.14b}$$

where \vec{p}_l and \tilde{p}_l denote the power flow from the starting and ending sides of each line $l \in \mathcal{L}$. Power loss on a line is

$$\vec{p}_l + \tilde{p}_l = v_i(v_i - v_j)g_l x_l + v_j(v_j - v_i)g_l x_l \quad (3.15a)$$

$$= (v_i^2 - v_i v_j + v_j^2 - v_i v_j)g_l x_l \quad (3.15b)$$

$$= (v_i^2 + v_j^2 - 2v_i v_j)g_l x_l \quad (3.15c)$$

$$= (v_i - v_j)(g_l x_l)(v_i - v_j)^\top. \quad (3.15d)$$

The total power loss is the sum of power flows entering the lines through their starting and ending buses as

$$\vec{\mathbf{p}} = \text{diag}\{\vec{\mathbf{L}} \mathbf{v} \mathbf{v}^\top \vec{\mathbf{G}}^\top\}, \quad \tilde{\mathbf{p}} = \text{diag}\{\tilde{\mathbf{L}} \mathbf{v} \mathbf{v}^\top \tilde{\mathbf{G}}^\top\} \quad (3.16a)$$

$$\sum(\vec{\mathbf{p}} + \tilde{\mathbf{p}}) = \text{Tr}(\mathbf{v} \mathbf{v}^\top (\vec{\mathbf{G}}^\top \vec{\mathbf{L}} + \tilde{\mathbf{G}}^\top \tilde{\mathbf{L}})) \quad (3.16b)$$

$$= \mathbf{v}^\top (\vec{\mathbf{G}}^\top \vec{\mathbf{L}} + \tilde{\mathbf{G}}^\top \tilde{\mathbf{L}}) \mathbf{v}. \quad (3.16c)$$

Using (3.16c), we can chose \mathbf{M} as

$$\mathbf{M} = (\vec{\mathbf{G}}^\top \vec{\mathbf{L}} + \tilde{\mathbf{G}}^\top \tilde{\mathbf{L}}). \quad (3.17)$$

Notice that if \mathbf{M} is chosen as in (3.17), which is actually equal to the conductance matrix \mathbf{G} , loss minimization will be indirectly embedded in the objective function (3.4a) with a proper choice of \mathbf{N} . $\mathbf{N} = \mathbf{I}_{l \times l}$ implicitly penalizes the power loss over all the lines as given in (3.15).

3.2.4 Strengthening the Convex Relaxation

Power networks usually have intermediate buses (or hidden nodes [60]) that do not demand/supply power or current with any external source or load, e.g., see bus 3 in Figure 9. These intermediate buses are referred to as *zero injection buses*[81]. We exploit their presence to define a number of valid inequality and strengthen the convex relaxation in (3.4).

Definition 1. *A bus $k \in \mathcal{N}$ is regarded as a zero injection bus if both power and current injections at bus k are zero, i.e., if no load or source is located at the bus [22]. The set of zero injection buses are presented by \mathcal{Z} .*

Define \mathbf{v}^* and \mathbf{x}^* be the solutions to the original problem (3.3). Then,

$$\mathbf{e}_k^\top \text{diag}\{\mathbf{G}\mathbf{v}^*\mathbf{x}^{*\top}\} = \mathbf{0}_n \quad (3.18)$$

holds for every $k \in \mathcal{Z}$, where $n = |\mathcal{Z}|$.

For zero injection buses, the sum of the currents absorbed from the distribution network is equal to the sum of the currents they supply to the distribution network. This feature can be expressed as

$$\begin{aligned} \mathbf{e}_k^\top \text{diag}\{\mathbf{G}\mathbf{v}^*\mathbf{x}^{*\top}\} = \\ \sum_{l=1}^{|\mathcal{K}|} d_l^\top (\vec{\mathbf{L}} \text{diag}\{\vec{\mathbf{G}}\mathbf{v}^*\mathbf{x}^{*\top}\} + \tilde{\mathbf{L}} \text{diag}\{\tilde{\mathbf{G}}\mathbf{v}^*\mathbf{x}^{*\top}\}), \end{aligned} \quad (3.19)$$

where \mathcal{K} is the set of neighbor buses of the zero injection bus k . The following formulation can be inferred from (3.19)

$$\sum_{l=1}^{|\mathcal{K}|} d_l^\top (\vec{\mathbf{L}} \text{diag}\{\vec{\mathbf{G}}\mathbf{v}^*\mathbf{x}^{*\top}\}) =$$

$$- \sum_{l=1}^{|\mathcal{K}|} d_l^\top (\bar{\mathbf{L}} \text{diag}\{\bar{\mathbf{G}}\mathbf{v}^* \mathbf{x}^{*\top}\}), \quad (3.20)$$

concluding that (3.18) is valid for any $k \in \mathcal{Z}$.

According to (3.20), the set of additional constraints

$$\mathbf{e}_k^\top \text{diag}\{\mathbf{G}\mathbf{A}\} = \mathbf{0}_n \quad (3.21)$$

can be added in (3.4) to strengthen its relaxation.

3.2.5 Joint Observation in the Presence of Noisy Measurements

The convex problem (3.4) can become infeasible, or result in a poor approximate, if available measurements become noisy. In this case, solving the state estimation problem requires tackling two concerns: (i) how to address non-linear relation between sensor measurements and state variables, (ii) how to address corrupted sensor measurements. We introduce auxiliary variables $\mathbf{v}^g, \mathbf{i}^g \in \mathbb{R}^{|\mathcal{M}|}$, $\vec{\mathbf{i}}^g, \bar{\mathbf{i}}^g \in \mathbb{R}^{|\mathcal{L}|}$ and $\mathbf{v}^s, \mathbf{i}^s \in \mathbb{R}^{|\mathcal{M}|}$, $\vec{\mathbf{i}}^s, \bar{\mathbf{i}}^s \in \mathbb{R}^{|\mathcal{L}|}$ to handle measurement noise where they account for Gaussian and sparse noise estimations, respectively. New variables $\mathbf{u} \in \mathbb{R}^{|\mathcal{M}|}$ and $\mathbf{S} \in \mathbb{R}^{|\mathcal{M}| \times |\mathcal{L}|}$ account for the \mathbf{v}^{g^2} and $\mathbf{v}^s \mathbf{x}^\top$, respectively. Unknown measurement noise can be estimated by incorporating these auxiliary variables as convex regularization terms into the objective function (3.4a). The joint state estimation and topology identification problem, that is robust to noisy and entirely corrupted measurements, can be formulated as

$$\begin{aligned}
& \underset{\substack{\mathbf{A} \in \mathbb{R}^{|\mathcal{N}| \times |\mathcal{L}|} \\ \mathbf{S} \in \mathbb{R}^{|\mathcal{N}| \times |\mathcal{L}|} \\ \mathbf{i}^g, \mathbf{i}^s \in \mathbb{R}^{|\mathcal{N}|} \\ \mathbf{u}, \mathbf{v}, \mathbf{v}^g, \mathbf{v}^s \in \mathbb{R}^{|\mathcal{N}|} \\ \mathbf{x}, \vec{\mathbf{i}}^g, \vec{\mathbf{i}}^s, \bar{\mathbf{i}}^g, \bar{\mathbf{i}}^s \in \mathbb{R}^{|\mathcal{L}|}}}{\text{minimize}} & \quad \|\mathbf{M}^{\frac{1}{2}}(\mathbf{A} - \mathbf{v}\mathbf{x}^\top)\mathbf{N}^{\frac{1}{2}}\|_* + \|\mathbf{v} - \mathbf{v}_0\|_M^2 + \|\mathbf{x} - \mathbf{x}_0\|_N^2 \\
& + \mu_1(\mathbf{1}^\top \mathbf{u}) + \mu_2 \|\mathbf{i}^g\|_2^2 + \mu_3 \|\mathbf{v}^s\|_2^2 \\
& + \mu_4 \|\mathbf{i}^s\|_2^2 + \mu_5 \|\mathbf{S}\|_* \\
& + \mu_6 \|\vec{\mathbf{i}}^g\|_2^2 + \mu_7 \|\vec{\mathbf{i}}^s\|_2^2 \\
& + \mu_8 \|\bar{\mathbf{i}}^g\|_2^2 + \mu_9 \|\bar{\mathbf{i}}^s\|_2^2
\end{aligned} \tag{3.22a}$$

$$\text{subject to} \quad v_k = \hat{v}_k - v_k^g - v_k^s \quad \forall k \in \mathcal{S}_v \tag{3.22b}$$

$$\mathbf{e}_k^\top \text{diag}\{\mathbf{G}\mathbf{A}\} = \hat{v}_k - i_k^g - i_k^s \quad \forall k \in \mathcal{S}_i \tag{3.22c}$$

$$\mathbf{d}_l \text{diag}\{\vec{\mathbf{G}}\mathbf{A}\} = \vec{\hat{i}}_l - \vec{i}_l^g - \vec{i}_l^s \quad \forall l \in \mathcal{S}_{\vec{i}} \tag{3.22d}$$

$$\mathbf{d}_l \text{diag}\{\bar{\mathbf{G}}\mathbf{A}\} = \bar{\hat{i}}_l - \bar{i}_l^g - \bar{i}_l^s \quad \forall l \in \mathcal{S}_{\bar{i}} \tag{3.22e}$$

$$\mathbf{A} \mathbf{d}_l^\top = \mathbf{v} \hat{x}_l \quad \forall l \in \mathcal{S}_x \tag{3.22f}$$

$$\mathbf{S} \mathbf{d}_l^\top = \mathbf{v}^s \hat{x}_l \quad \forall l \in \mathcal{S}_x \tag{3.22g}$$

$$\mathbf{x}^{\text{lb}} \leq \mathbf{x} \leq \mathbf{x}^{\text{ub}} \tag{3.22h}$$

$$\mathbf{v}(\mathbf{x}^{\text{lb}})^\top \leq \mathbf{A} \leq \mathbf{v}(\mathbf{x}^{\text{ub}})^\top \tag{3.22i}$$

$$\mathbf{v}^s(\mathbf{x}^{\text{lb}})^\top \leq \mathbf{S} \leq \mathbf{v}^s(\mathbf{x}^{\text{ub}})^\top \tag{3.22j}$$

$$v_k^{g2} \leq u_k \quad \forall k \in \mathcal{S}_v \tag{3.22k}$$

$$\begin{bmatrix} x_l & \hat{v}_k x_l - A_{kl} - S_{kl} \\ \hat{v}_k x_l - A_{kl} - S_{kl} & u_k \end{bmatrix} \succeq 0 \quad \forall k \in \mathcal{S}_v, \forall l \in \mathcal{L} \tag{3.22l}$$

where $\mu_n \geq 0$ are pre-selected coefficients for every $n = \{1, 2, \dots, 9\}$ that balance the data fitting cost $\mu_1(\mathbf{1}^\top \mathbf{u}) + \mu_2 \|\mathbf{i}^g\|_2^2 + \mu_3 \|\mathbf{v}^s\|_2^2 + \mu_4 \|\mathbf{i}^s\|_2^2 + \mu_5 \|\mathbf{S}\|_* + \mu_6 \|\vec{\mathbf{i}}^g\|_2^2 + \mu_7 \|\vec{\mathbf{i}}^s\|_2^2 + \mu_8 \|\overleftarrow{\mathbf{i}}^g\|_2^2 + \mu_9 \|\overleftarrow{\mathbf{i}}^s\|_2^2$ with the remaining elements of the objective function in (3.22a). $\mathcal{S}_{\vec{i}}$ and $\mathcal{S}_{\overleftarrow{i}}$ denote the set of current flow measurements from both sides of each line. The objective function (3.4a) aims to handle the non-linearity of the measurement equation, while the convex regularization term added in (3.22a) deals with the noisy and corrupted measurements.

Proposition 2. *Let \mathbf{v}^* , \mathbf{x}^* , \mathbf{v}^{g*} , \mathbf{i}^{s*} , $\vec{\mathbf{i}}^{s*}$, $\overleftarrow{\mathbf{i}}^{s*}$, \mathbf{v}^{s*} , \mathbf{i}^{g*} , $\vec{\mathbf{i}}^{g*}$, $\overleftarrow{\mathbf{i}}^{g*}$, and \mathbf{u}^* be the ground-truth values for the original problem (3.3). Let $\mathbf{u}^* \triangleq \mathbf{v}^{s*2}$, $\mathbf{S}^* \triangleq \mathbf{v}^s \mathbf{x}^\top$, and $\mathbf{A}^* \triangleq \mathbf{v}^* \mathbf{x}^{*\top}$. Then, the constraint (3.22l) is satisfied.*

Proof. Since v_k^* and x_l^* are positive, one can write

$$A_{kl}^* = v_k^* x_l^* \Leftrightarrow A_{kl}^* = (\hat{v}_k - v_k^{g*} - v_k^{s*}) x_l^* \quad (3.23a)$$

$$\Rightarrow \hat{v}_k x_l^* - A_{kl}^* = (v_k^{g*} + v_k^{s*}) x_l^*$$

$$\Rightarrow \hat{v}_k x_l^* - A_{kl}^* - S_{kl}^* = v_k^{g*} x_l^*$$

$$\Leftrightarrow (\hat{v}_k x_l^* - A_{kl}^* - S_{kl}^*)^2 = (v_k^{g*})^2 x_l^{*2} \quad (3.23b)$$

$$\Rightarrow (\hat{v}_k x_l^* - A_{kl}^* - S_{kl}^*)^2 = u_k^* x_l^* \text{ or } 0$$

$$\Leftrightarrow (\hat{v}_k x_l^* - A_{kl}^* - S_{kl}^*)^2 \leq u_k^* x_l^* \text{ or } 0 \quad (3.23c)$$

As seen, (3.23) is equivalent to (3.22l) under the proposition 2. This completes the proof. \square

If pre-selected coefficients are chosen as $\mu_n = 0$, the objective function (3.22a) is reduced to the objective function (3.4a), which can only contrive the non-convexity of the measurement equations in noiseless scenarios. If $\mu_n = +\infty$, then the objective

function (3.22a) prioritizes estimating the unknown noise values while ignoring the remaining elements.

Remark 3. *If the relaxation is exact, then we have $\mathbf{A}^* = \mathbf{v}^* \mathbf{x}^{*\top}$, in which case the solver only minimizes the error values, $\mu_1(\mathbf{1}^\top \mathbf{u}) + \mu_2 \|\mathbf{i}^g\|_2^2 + \mu_3 \|\mathbf{v}^s\|_2^2 + \mu_4 \|\mathbf{i}^s\|_2^2 + \mu_5 \|\mathbf{S}\|_* + \mu_6 \|\vec{\mathbf{i}}^g\|_2^2 + \mu_7 \|\vec{\mathbf{i}}^s\|_2^2 + \mu_8 \|\overleftarrow{\mathbf{i}}^g\|_2^2 + \mu_9 \|\overleftarrow{\mathbf{i}}^s\|_2^2$, within the space of zero residual points (i.e., the set of all points that satisfy $\mathbf{A} = \mathbf{v} \mathbf{x}^\top$). Observe that $\mathbf{A} = \mathbf{v} \mathbf{x}^\top$ cannot be imposed as a constraint due to its non-convexity. This is the motivation behind incorporating its surrogate into the objective. However, this surrogate will ultimately serve as a hard constraint.*

The goal of (3.22) is to determine an approximate solution for the state estimation problem in the presence of noisy measurements without increasing the number of available sensor, or for the joint state estimation and topology identification problem despite noisy and entirely corrupted measurements with the help of additional set of measurements. It should be noted that corrupted measurements can make the network unobservable, and the number of available sensors should be relatively high (i.e., $\Theta \geq 4\mathcal{Y}-4$, where Θ and \mathcal{Y} denote the total number of available sensors and the state variables to be found, respectively) for a robust estimation [10]. If one considers a joint state estimation and topology identification problem in the presence of noise and severely corrupted measurements, the number of unknown parameters could grow beyond the number of possible measurements. This makes the problem unsolvable due to information-theoretic limitations [10].

3.3 Case Studies

In the following, standard IEEE AC benchmarks are transformed into DC benchmarks by substituting AC generators with DC sources coupled with buck converters, and having distribution lines purely resistive. While the standardization of

future DC networks is under development, IEEE [82], European standard ETSI [83], EMerge Alliance [84], and IEC SG4 [85] have suggested 380V DC as a suitable rated voltage level for distribution systems. Herein, the DC distribution line parameters are adjusted according to the rated voltage level [86, 87]. All lines are equipped with switches to control the network topology. If monitored, a bus is equipped with a sensor to measure voltage and/or a sensor to measure current injection. Monitored lines refer to the lines with a sensor. The optimization problem is run using the conic interior-point solver, MOSEK [88], in the CVX [53] optimization package.

3.3.1 Numerical Studies

The joint state estimation and topology identification problem is examined for the modified IEEE 9-bus [89], 14-bus [90], and 30-bus systems [91] when measurements are assumed noiseless. We compare our method in (3.4), using proper basis \mathbf{M} and \mathbf{N} values in (3.17) and the set of additional constraints in (3.21), with the conventional GSE method [58]. Herein, the total number of sensors is initially determined such that the jacobian matrix of estimation equations [58] is surely not full rank while initial configuration of sensors is randomly chosen. Then, the number of sensors is gradually increasing to observe the performances of both proposed method and the method in [58] for varying numbers and locations of sensors.

For a specified number of sensors, the sensors are randomly deployed. This configuration is simulated for a time horizon with 100 steps while random changes in voltage levels and an arbitrary line removal happen at every time-step and every fifth time-step, respectively. Afterward, the sensor configuration is randomly rearranged without increasing the number of sensors, and then the simulation is run again. To provide more reliable statistical results, for a given number of sensors, this process is repeated 250 times. Each approach has a flat start with 10^{-6} as the mismatch

threshold to conclude a successful run. The success rate percentage is computed as $\nu^i = \frac{1}{c} \sum_1^c \frac{h_c^i - f_c^i}{h_c^i} \times 100$, where h_c^i , and f_c^i , are the number of steps in a horizon, and the number of steps failed to satisfy the mismatch threshold in a horizon, respectively. c , and i denote the number of random attempts for sensor reconfiguration, and the total number of sensors, respectively. In this study, $h_c^i = 100$ for every $c \in \{1, 2, \dots, 250\}$.

It should be noted that the network observability is ascertained by both the location of sensors and its total number. The success of the GSE method hinges on a full observability condition that would require highly-redundant sensor allocation. As seen in Figures 10 (a)-(c), the proposed method significantly outperforms the GSE approach.

3.3.2 Experimental Studies

In the modified 14-bus system, the input voltage of DC-DC buck converters is 500 V, while the distribution network is rated for 380 V. The ratings of the power converters located at buses 1, 2, 3, 6, and 8 are 150 kW, 50 kW, 100 kW, 100 kW, and 50 kW, respectively. Sample consumption trajectories for the six out of eleven loads are given in Figure 12. The consumption profiles intentionally mimic a 24-hour load pattern, and are generated using poisson distribution. This distribution assumes that the sudden load changes occur randomly with the probability mass function, $P(k) = e^{-\lambda} \frac{\lambda^k}{k!}$. Here, k and λ denote the type and average number of load changes. The voltage sensors are placed on the buses with a power converter. The current injection values are measured for buses $(\mathcal{N} \setminus \mathcal{Z})$ that are not zero-injection buses. It should be observed that bus 7 and bus 14 of the IEEE-14 bus system are zero injection buses. The statuses of ten lines are monitored as illustrated in Figure 11. The internal droop mechanism of power converters regulate their output voltage in response to output power variations due to the changes in the load profile or network topology.

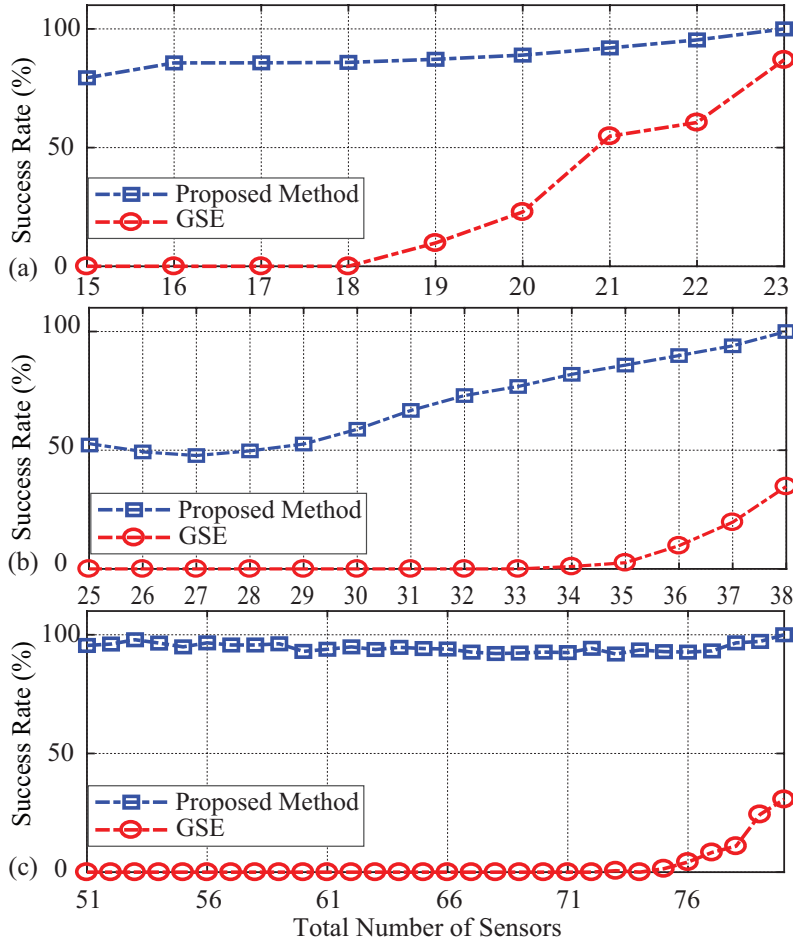


Figure 10: Comparative convergence rates of proposed and generalized state estimation methods for the IEEE (a) 9-bus, (b) 14-bus, and (c) 30 bus systems.

HIL platform with a dSPACE DS1202 MicroLabBox to perform droop controllers for each converters, and a Typhoon HIL604 unit to emulate power converters and the distribution network is used to emulate this network. The proposed optimization algorithm runs on a PC with 16-core, Xeon processor and 256 GB RAM.

3.3.2.1 Noiseless measurements

We consider a time horizon, where the statuses of unmonitored lines change randomly and load profiles are dynamic. The proposed formulation in (3.4), with

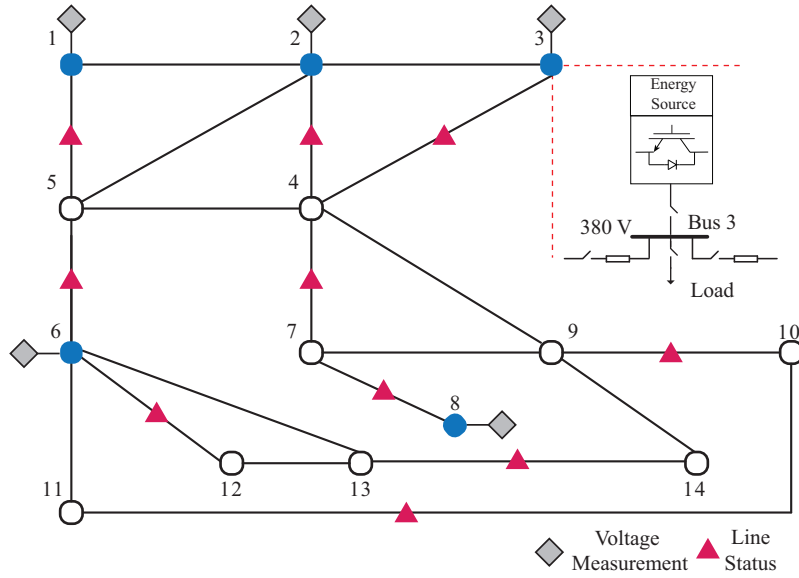


Figure 11: The modified IEEE 14-bus system populated with 5 DC-DC buck converters (illustrated by ●), and equipped with sensors to monitor voltages (illustrated by ◆), line statuses (illustrated by ▲), and injected current at bus $k \in \mathcal{N} \setminus \{\mathcal{Z}\}$.

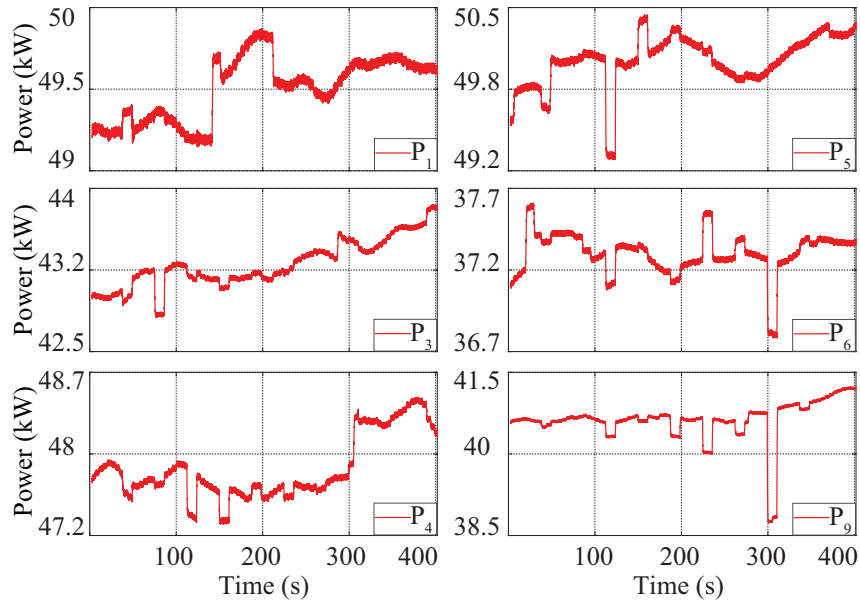


Figure 12: Load power trajectories at selected buses 1, 3, 4, 5, 6, and 9.

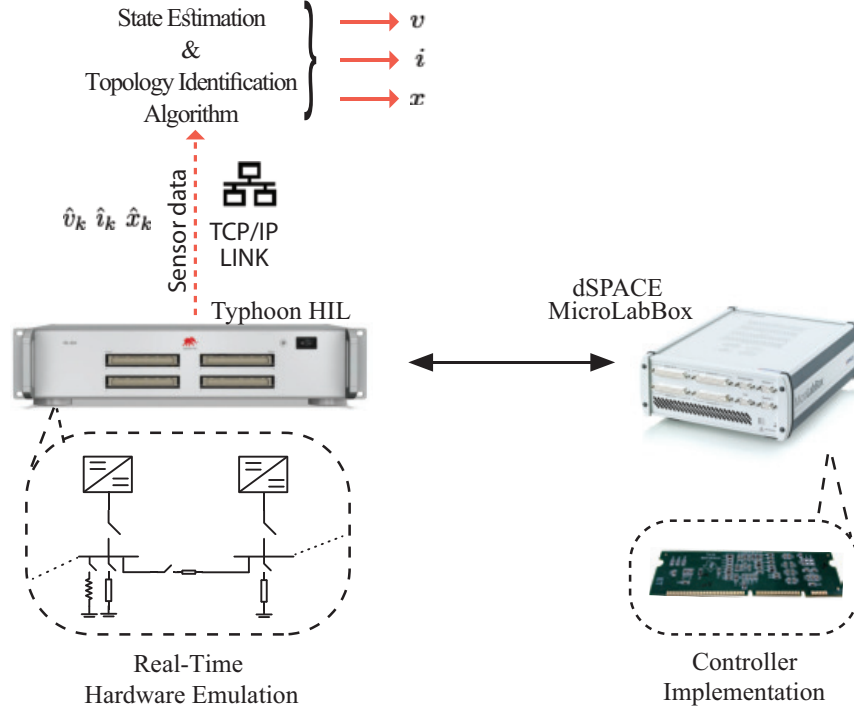


Figure 13: DC network joint observation testbed on a HIL system embodying of controller implementation (dSPACE), real-time hardware emulation (Typhoon HIL), and TCP/IP communication link for data transfer.

$\mathbf{M} = \mathbf{G}$, $\mathbf{N} = \mathbf{I}_{l \times l}$, and the set of additional constraints in (3.21), finds states and topology configurations every five seconds. Figure 14 shows the recovered (v) and the ground-truth (\tilde{v}) voltage values for the unmonitored buses. Figure 15 presents the recovered (x) and the ground-truth (\tilde{x}) values for the statuses of unmonitored lines in response to the removal of an arbitrary line. It is observed that the maximum errors in terms of percentage for recovered voltage values and statuses of lines are always less than 10^{-6} . Consequently, the proposed method yields a very good pursuit of ground-truth values for voltages and statuses of the lines when measurements are assumed noiseless. So far, we haven't used any penalty term or tuning parameter in the convex program (3.4). The average time for finding states and topology configurations is 2.208 s.

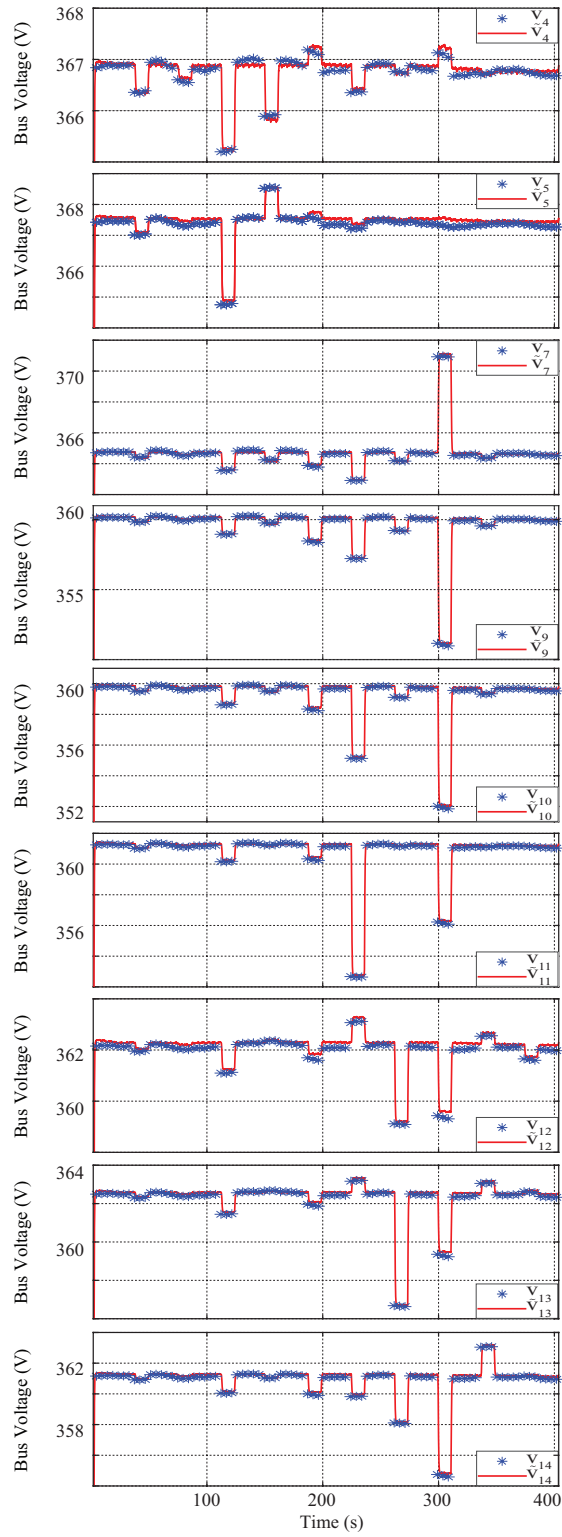


Figure 14: Estimated (v_k), and ground-truth (\tilde{v}_k) voltage values for unmonitored buses.

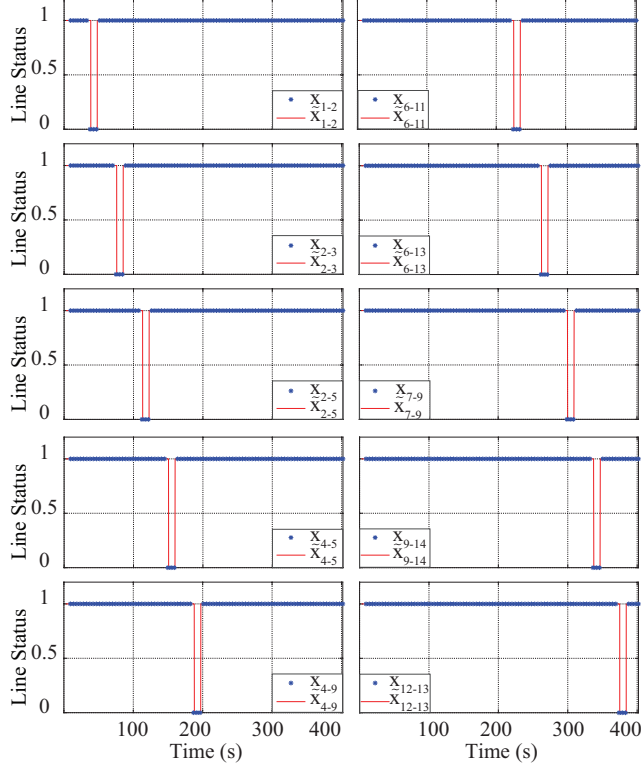


Figure 15: Estimated (x_l), and ground-truth (\tilde{x}_l) values for the statuses of the lines in response to the removal of one line. x_{a-b} denotes the line status for a line which starts from node a and ends in b.

3.3.2.2 Noisy measurements

In this section, we verify that proposed algorithm is capable of finding an approximate solution in the presence of noisy measurements. All the voltage and current measurements are assumed corrupted by zero-mean Gaussian noises with 1% standard deviation of the corresponding noiseless value. The proposed formulation in (3.22), with $\mathbf{M} = \mathbf{G}$ and $\mathbf{N} = \mathbf{I}_{l \times l}$, finds system states every five seconds. Root-mean-square error (RMSE) is considered to assess the estimated voltages \mathbf{v} under the zero-mean Gaussian noise that has 1% standard deviation for all the measurements. The RMSE of the \mathbf{v} is formalized as $\psi(\mathbf{v}) := \|\mathbf{v} - \tilde{\mathbf{v}}\|_2 / \|\tilde{\mathbf{v}}\|_2^2$. The pre-selected coefficients in (3.22), that balance the data fitting cost, are set to $\mu_1 = \mu_2 = 10^2$ and

$\mu_3 = \mu_4 = \mu_5 = \mu_6 = \mu_7 = \mu_8 = \mu_9 = 1$. It should be observed that the coefficients for the current flow measurements, μ_6 , μ_7 , μ_8 , and μ_9 , are redundant since $\mathcal{S}_{\tilde{r}} = \mathcal{S}_{\tilde{r}} = \emptyset$.

3.3.2.2.1 State estimation Herein, we demonstrate an approximate solution in the case measurements are noisy, and the number of available sensors remains the same. The network topology is assumed to be either static or completely monitored due to existing noisy measurements that do not allow both state estimation and topology identification simultaneously with the same number and configuration of sensors as they are in Section 3.3.2.1. We consider a time horizon with a dynamic load profile and a fully-monitored network topology. The RMSE of the estimated voltages for the buses with sensors, i.e., $\psi(v_k) := \|v_k - \tilde{v}_k\|_2 / \|\tilde{v}_k\|_2^2$ for every $k \in \mathcal{S}_v$, shown in Figure 16 demonstrates that an approximate solution is recoverable with 99.95% accuracy. It is observed that the maximum RMSE values for buses with and without sensors are 0.024% and 0.001%, respectively. Moreover, the maximum voltage errors, in terms of percentage for buses with and without sensors, are 0.011% and 0.0002%, respectively. Figure 17 depicts the corrupted (\hat{v}), recovered (v), and the ground-truth (\tilde{v}) voltage values where bus measurements are corrupted by 1%. The proposed method yields a very close pursuit of ground-truth voltage values when all the voltage and current measurements are subject to noise. Determination of states in the presence of noisy measurements takes 2.648 s on average.

3.3.2.2.2 State estimation and topology identification We aim to show an approximate solution for the joint state estimation and topology identification problem with the help of additional voltage measurements. We assume measurement of voltage values are available from all the buses while rest of the measurements and their configurations remain the same as they are in Section 3.3.2.1. The experiment

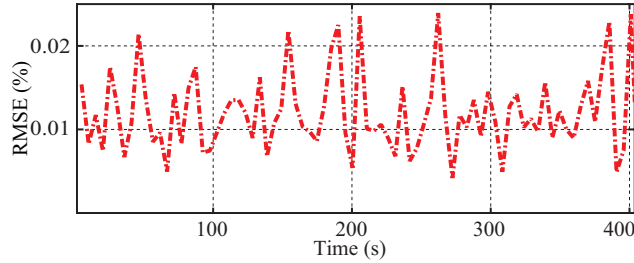


Figure 16: The performance of (3.22) to estimate the vector of voltages in the case where the goal is to solve the state estimation problem in the presence of noisy measurements without increasing the number of available sensors.

time horizon is considered with a random change in the statuses of unmonitored lines and dynamic load profiles. The RMSE of the estimated voltages shown in Figure 18 demonstrates that an approximate solution is recoverable with more than 99.4% accuracy. It is observed that the maximum RMSE value for the estimated voltages is 0.543%. The maximum percentage errors for recovered voltage values and statuses of lines are less than 0.098% and 10^{-6} , respectively. Figure 19 shows the corrupted (\hat{v}), recovered (v), and the ground-truth (\tilde{v}) voltage values for some of the selected buses. The proposed method also yields a very good pursuit of ground-truth values for line statuses same as the results shown in Figures 15 or 22. The average time needed to find states and topology configurations in the presence of noisy measurements is 3.617 s.

3.3.2.3 Severely corrupted measurements

Herein, we aim to show that the proposed method, with the help of additional set of measurements, i.e., $\mathcal{S}_{\tilde{v}}$, $\mathcal{S}_{\tilde{i}}$, can handle the case where each measurement is corrupted either by zero-mean Gaussian noises with 1% standard deviation or 100% of the corresponding original value. We consider a time horizon with a random change in the statuses of unmonitored lines and dynamic load profiles. The proposed

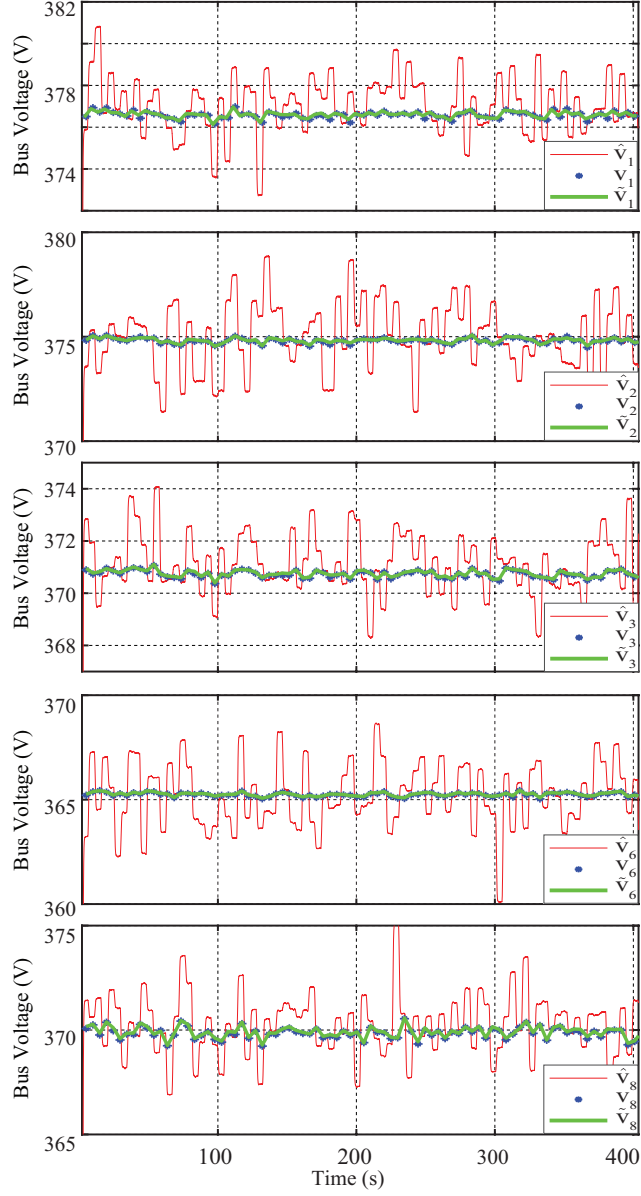


Figure 17: Estimated voltage values obtained by (3.22) for the monitored sensor measurements corrupted by %1 additive noise.

formulation in (3.22), with $\mathbf{M} = \mathbf{G}$ and $\mathbf{N} = \mathbf{I}_{l \times l}$, finds system states every five seconds. Randomly-chosen two of the sensor measurements are severely corrupted, while the rest of them are under 1% Gaussian noise. These two entirely-corrupted sensors measure the voltage at bus 5 and the current injection at bus 1. Herein, the

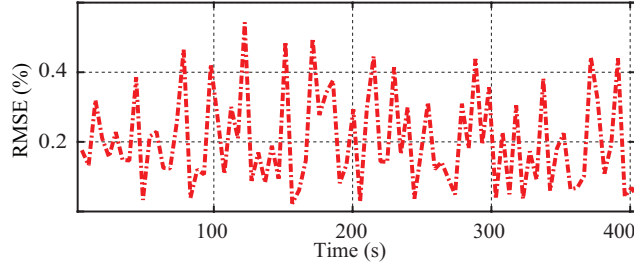


Figure 18: The performance of (3.22) to estimate the vector of voltages when solving the state estimation and topology identification problem, in the presence of noisy measurements, with the help of additional voltage measurements.

pre-selected coefficients are set to $\mu_1 = \mu_2 = 10^2$ and $\mu_3 = \mu_4 = \mu_5 = \mu_6 = \mu_7 = \mu_8 = \mu_9 = 1$. Figure 20 demonstrates that an approximate solution is recoverable with more than 99.3% accuracy. It is observed that the maximum RMSE and the voltage error values for the estimated voltages are 0.660% and 0.288%, respectively. Figure 21 shows the corrupted (\hat{v}), recovered (v), and the ground-truth (\tilde{v}) voltage values for selected buses. Maximum percentage error for estimated statuses of lines is less than 10^{-6} , leading to a very good pursuit of ground-truth values as shown in Figure 22. It should be observed here that, in the case of a line removal, $x_l = 0$ for every $l = (a, b) \in \mathcal{L}$, the direct voltage correlation between buses a and b disappears. The internal droop mechanism of power converters regulates their output voltage such that physical laws, presented in (3.1)-(3.2) and (3.14a)-(3.14b), are conserved independent of the line status. Figure 23 highlights the variations on ground-truth voltage levels at bus 4, which has the highest connectivity with neighboring buses, due to changes in topology and load power trajectories. The determination of the states and topology configurations in the presence of measurement gross errors takes 4.645 s on average.

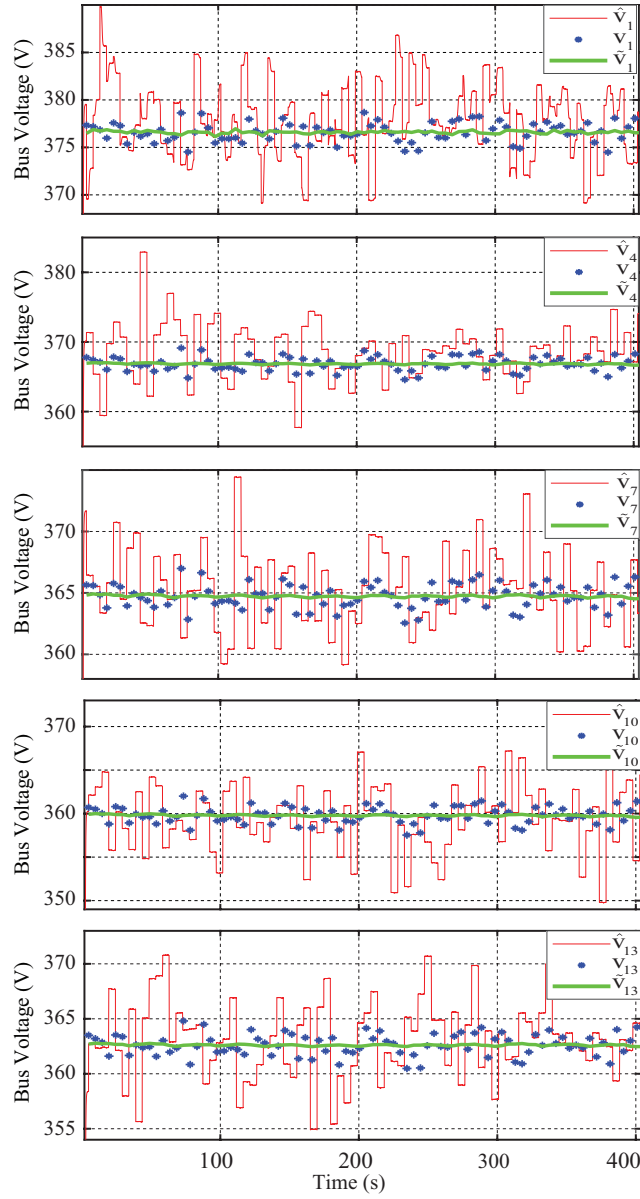


Figure 19: Estimated voltage values obtained by (3.22) at selected sensor measurements. Each measurement is corrupted by %1 additive noise.

3.4 Summary

This chapter offers a convex optimization framework to solve the state estimation and topology identification problems using only a limited number of measurement for converter-augmented DC networks. This problem is formulated as a constrained

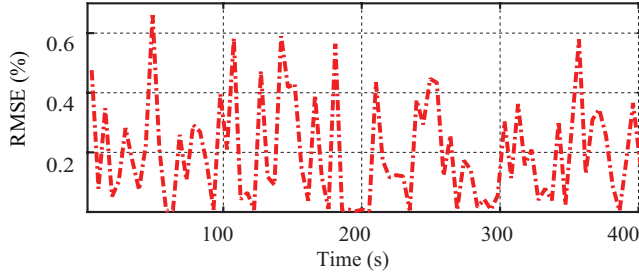


Figure 20: The performance of (3.22) to estimate the vector of voltages for the modified IEEE 14-bus system where each measurement is either corrupted by zero-mean Gaussian noises with 1% standard deviation or 100% of the corresponding original value.

minimization problem, where a proper choice of objective function obviates any tuning coefficient in the absence of measurement noise. The problem formulation is then extended for the noisy measurements by adding auxiliary variables to account for convex regularization terms in the objective function. The proposed method is studied where the set of measurements are: (i) voltage values at some of the randomly-chosen buses, (ii) current-injection values at some of the randomly-chosen buses, and (iii) some of the line statuses. The convex formulation in the absence of measurement noise is validated through numerical tests using IEEE 9-bus, 14-bus, and 30-bus benchmarks, and HIL experimentation using modified IEEE 14-bus system. Furthermore, the solution in the presence of 1% measurement noise is verified through HIL experimentation on the IEEE 14-bus system. With the help of an additional set of measurements, this solution can handle scenarios where each measurement is corrupted either by zero-mean Gaussian noises with 1% standard deviation or 100% of the corresponding original values.

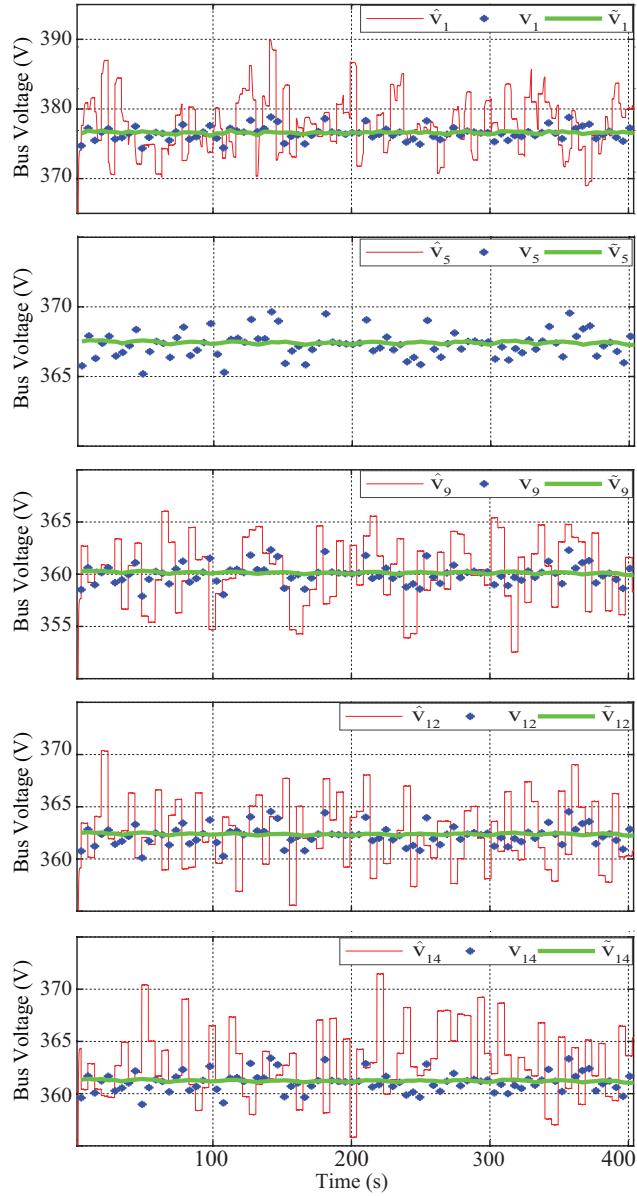


Figure 21: Estimated voltage values obtained by (3.22) at selected sensor measurements. Each measurement is either corrupted by zero-mean Gaussian noises with 1% standard deviation or 100% of the corresponding original value. The voltage measurement at bus 5, \hat{v}_5 , is out of range in Figure as it is entirely corrupted.

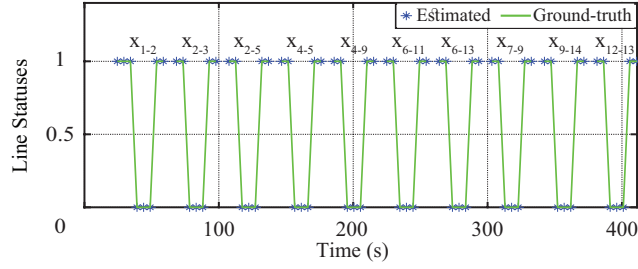


Figure 22: Estimated (x_l), and ground-truth values, for the line statuses in response to the removal of one line. x_{a-b} denotes the status of a line starting from node a and ending in b.

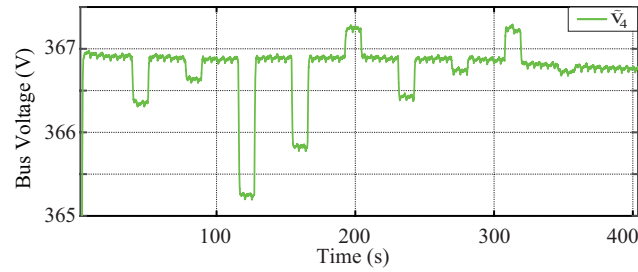


Figure 23: Changes on the levels of ground-truth voltage values at bus 4 due to changes in topology and load power trajectories.

3.5 Appendix

This section presents model matrices and vectors from network characteristics using the example of 3-bus network in Figure 9. The bus conductance matrix of 3-bus network is calculated as

$$\mathbf{G} = \begin{bmatrix} g_{12} + g_{13} & -g_{12} & -g_{13} \\ -g_{21} & g_{21} + g_{23} & -g_{23} \\ -g_{31} & -g_{32} & g_{31} + g_{32} \end{bmatrix}. \quad (3.24)$$

The line conductance matrices, *from* and *to*, can be formed as

$$\vec{\mathbf{G}} = \begin{bmatrix} g_{12} & -g_{12} & 0 \\ g_{13} & 0 & -g_{13} \\ 0 & g_{23} & -g_{23} \end{bmatrix}, \quad \vec{\mathbf{G}} = \begin{bmatrix} -g_{12} & g_{12} & 0 \\ -g_{13} & 0 & g_{13} \\ 0 & -g_{23} & g_{23} \end{bmatrix}. \quad (3.25)$$

The network *from* and *to* bus-line incidence matrices for 3-bus network are

$$\vec{\mathbf{L}} = \begin{bmatrix} 1 & 0 & 0 \\ 1 & 0 & 0 \\ 0 & 1 & 0 \end{bmatrix}, \quad \vec{\mathbf{L}} = \begin{bmatrix} 0 & 1 & 0 \\ 0 & 0 & 1 \\ 0 & 0 & 1 \end{bmatrix}. \quad (3.26)$$

It can be observed that \mathbf{G} can be derived from $(\vec{\mathbf{G}}^\top \vec{\mathbf{L}} + \vec{\mathbf{G}}^\top \vec{\mathbf{L}})$ that is also chosen as the basis matrix \mathbf{M} . The basis matrix \mathbf{N} , that is designed to penalize power loss over all the lines, is formed as

$$\mathbf{N} = \begin{bmatrix} 1 & 0 & 0 \\ 0 & 1 & 0 \\ 0 & 0 & 1 \end{bmatrix}. \quad (3.27)$$

The vectors of voltages, currents, and statuses of lines can be formed based on the sensors positioning shown in Figure 9

$$\mathbf{v} = \begin{bmatrix} \hat{v}_1 \\ v_2 \\ v_3 \end{bmatrix}, \quad \mathbf{x} = \begin{bmatrix} x_1 \\ \hat{x}_2 \\ x_3 \end{bmatrix}, \quad \mathbf{i} = \begin{bmatrix} \hat{i}_1 \\ \hat{i}_2 \\ i_3 \end{bmatrix}. \quad (3.28)$$

Herein, measured values are utilized to infer unknown voltages v_2, v_3 , and statuses of the unmonitored lines, x_1, x_3 . It should be noted that the bus 3 is a zero-injection

bus, and it can facilitate the performance of (3.4) by using $i_3 = 0$ as an additional constraint.

Finally, the auxiliary variable matrix \mathbf{A} , accounting for $\mathbf{v}\mathbf{x}^\top$, takes the following form

$$\mathbf{A} = \begin{bmatrix} \hat{v}_1 x_1 & \hat{v}_1 \hat{x}_2 & \hat{v}_1 x_3 \\ v_2 x_1 & v_2 \hat{x}_2 & v_2 x_3 \\ v_3 x_1 & v_3 \hat{x}_2 & v_3 x_3 \end{bmatrix}. \quad (3.29)$$

ENHANCED MODELING OF GENERATOR RESPONSE IN
SECURITY-CONSTRAINED OPF

T. Altun, R. Madani and A. Davoudi, "Enhanced Modeling of Generator Response
in Security-constrained Optimal Power Flow," Under Preparation.

CHAPTER 4
ENHANCED MODELING OF GENERATOR RESPONSE IN
SECURITY-CONSTRAINED OPF

Power flow investigation underpins many static or dynamic applications in power systems. These applications include stability analysis, optimal power flow, contingency analysis, etc. An accurate power flow solution ensures that generators meet the required power, i.e., total load and transmission losses. However, transmission losses cannot be identified in advance. Therefore, required total power generation to supply a known demand is unpredictable [23]. Common practice in power systems is to assume there exist at least one slack bus, where active power generation can be readjusted to compensate the system power imbalances[24]. To this end, power flow algorithms, such as Gauss, fast decoupled, Gauss-Seidel, Newton-Raphson, backward/forward sweep, and other derivative approaches compute the flow of electrical power based on single slack bus model [25]. Assuming a virtual generator with an infinite capacity or negative power does not reflect the physical behavior of the power systems.

Power flow models that are based on multiple slack bus concepts alleviate the burden of a pre-specified single slack bus by dispatching the imbalance among participating sources. [92]. This approach better mimics the operation of power systems provided that participation factors of generators are accurately determined. These factors can be appointed based on machine inertias [93], governor droop characteristics [94, 95], frequency control [96], and economic dispatch [97, 98, 99]. These studies usually ignore the relation between reactive power and voltage magnitude, as well as

the generator reactive power limits [100]. However, when reactive power generation limit is reached, the generator cannot maintain predefined voltage settings, and its bus type needs to be switched from PV bus to PQ bus [101]. The active and reactive power limits are handled via controller design [102], [103] by sacrificing the optimal operation. Moreover, possible component outage, i.e. generator or line, are rarely studied in the literature [104].

SCOPF formulation focuses on the optimization of robust power dispatch with respect to the outage of a random number of generators or lines [105, 25]. Preventive model of SCOPF finds a minimum operational cost that is identical, i.e., no redispatch, for both pre- and post-contingency scenarios [106]. Preventive SCOPF usually ignores generator failures in contingency scenarios [107]. Corrective model of SCOPF allows the limited exchanges in certain decision variables, i.e., redispatch, in post-contingency scenarios [108]. Corrective SCOPF considers both the generator and transmission line contingencies. To encapsulate the realistic behavior of generator in the case of a random number of contingency scenarios, additional constraints have to be incorporated into corrective models of SCOPF formulation [109]. These additional constraints are based on a piecewise-discontinuous model of real and reactive power responses that prevent both active and reactive power violations [110]. However, piecewise-discontinuous models prevent the use of power flow algorithms due to their undifferentiability [111]. This problem, and its possible adverse consequences, such as increased iteration count and convergence to a unstable region, have been discussed in [110].

Alternative differentiable power flow models using hyperbolic and sigmoid functions [109], patching functions with complementary homotopy methods [111], and discrete and continuous auxiliary variables are discussed [101]. These studies, however, did not validate their methods in the case of a random outage, i.e. a generator

or a line, and their performance depends on a specific numerical solver. In this chapter, we introduce several equivalent continuously-differentiable models that respect high-fidelity physical models of generators considering extensive list of contingency scenarios. These models prevent physical and operational violations by means of optimally, allocating active power imbalances among available generators and deciding the type of bus, i.e., PV/PQ switching, respectively. The proposed SCOPF formulation is in a generic form, and can be solved with various numerical solvers.

The rest of this chapter has the following organization. Section 4.1 discusses the preliminary materials. Section 4.2 elaborates the enhanced modeling of generator response including distributed slack bus representation, and generator active and reactive power contingency response models. Section 4.3 introduces several equivalent continuously-differentiable models that account for active and reactive power contingency responses in the SCOPF formulation. In Section 4.4, the resulting enhanced modeling of generator response in SCOPF solution is verified through a numerical benchmark system. Section 4.5 draws the conclusion.

4.1 Notations and Power Grid Terminologies

4.1.1 Notations

Bold lowercase and uppercase letters (e.g., \mathbf{a} , \mathbf{A}) represent vectors and matrices, respectively. $\mathbf{1}$ and $\mathbf{0}$ refer to vectors with all elements as 1 and 0, respectively. The sets of complex and real numbers are shown with \mathbb{C} and \mathbb{R} , respectively. \mathbb{H}^n and \mathbb{S}^n represent the hermitian and symmetric matrices of size $n \times n$, respectively. $\text{imag}\{\cdot\}$ and $\text{real}\{\cdot\}$ define the imaginary and real parts of a complex matrix or number, respectively. Superscripts $(\cdot)^\top$ and $(\cdot)^*$ stand for the transpose and conjugate transpose operator, respectively. $|\cdot|$ represents the cardinality of a set or the absolute/magni-

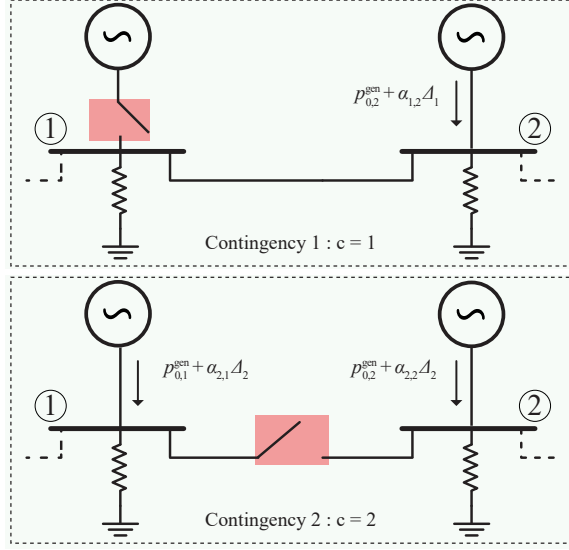


Figure 24: Contingency scenario samples for a portion of power grid. The base case refers to the scenario 0 that means no contingency. The red labels highlight the failure of a generator and a transmission line. In Scenario 1, generator 1 fails while generator 2 readjusts its generation according to weight $\alpha_{1,2}$. Scenario 2 illustrates a transmission line failure, while generator 1 and 2 contribute to power redistribution, Δ_2 .

tude value of a vector/scalar. $\text{diag}\{\cdot\}$ forms a vector using diagonal entries of a given matrix. $[\cdot]$ composes a matrix with diagonal entries from a given vector.

4.1.2 Power Grid Terminologies

Figure 24 represents a diagram for a power grid, where every single bus can accommodate an arbitrary set of generators and loads. The set of contingency scenarios is referred to as \mathcal{C} , and includes a network component outage, e.g., a generator or a transmission line. Herein, the *base case scenario*, i.e., normal operation with no outage, is indicated by $0 \in \mathcal{C}$. For the rest of the scenarios $c \in \mathcal{C}$, terminologies for grid elements are elaborated here:

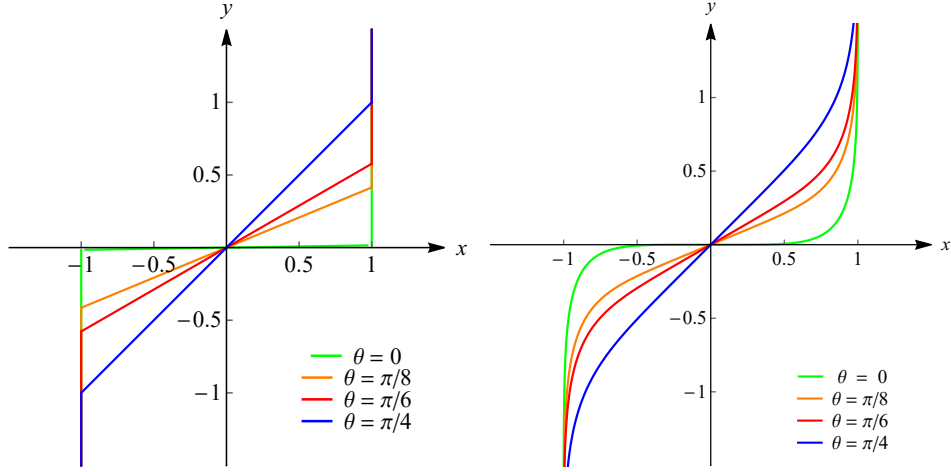
- **Buses and Lines:** The transmission grid is structured using a directed graph $\mathcal{H} = (\mathcal{N}, \mathcal{L})$, where the sets of buses and lines are denoted by \mathcal{N} and \mathcal{L} , respectively. Let $\vec{\mathbf{L}}_c, \bar{\mathbf{L}}_c \in \{0, 1\}^{|\mathcal{L}| \times |\mathcal{N}|}$ be the pairs for the *from* and *to* line-incidence

matrices in a contingency case, respectively. $\vec{L}_{c,li} = 1$ and $\vec{L}_{c,li} = 1$ for every $l \in \mathcal{L}$, iff the transmission line l starts at bus i , and vice versa, respectively. Matrices $\mathbf{Y}_c \in \mathbb{C}^{|\mathcal{N}| \times |\mathcal{N}|}$, $\vec{\mathbf{Y}}_c, \vec{\mathbf{Y}}_c \in \mathbb{C}^{|\mathcal{L}| \times |\mathcal{N}|}$ respectively denote the bus-admittance, and the *from* and *to* line-admittance matrices. Let $\mathbf{s}_c^{\max} \in (\mathbb{C} \cup \{\infty\})^{|\mathcal{L}|}$ be the vector of apparent power flow limits on transmission lines. Define $\mathbf{v}_0, \mathbf{v}_c \in \mathbb{C}^{|\mathcal{N}|}$ as the vectors of complex nodal voltages in the base and contingency case, respectively.

- **Generators/Loads:** Let \mathcal{G} be the set of generators and $\mathbf{G}_c \in \{0, 1\}^{|\mathcal{G}| \times |\mathcal{N}|}$ as the generator incidence matrix in a contingency case, where $G_{c,gi} = 1$ if generator $g \in \mathcal{G}$ is attached at the bus $i \in \mathcal{N}$ and not outed in a contingency scenario c . $G_{c,gi} = 0$ if and only if there is no generator $g \in \mathcal{G}$ located at the bus $i \in \mathcal{N}$ or it is outed in the contingency scenario c . $\mathbf{C}_c \in \{0, 1\}^{|\mathcal{G}| \times |\mathcal{N}|}$ denotes the incidence matrix to define whether a particular generator is effected by a given contingency c . $\mathbf{s}_c^{\text{dem}} \in \mathbb{C}$ represents the vectors of apparent power demand. Let $\mathbf{s}_0^{\text{gen}} \in \mathbb{C}^{|\mathcal{G}|}$, and $\mathbf{p}_0^{\text{gen}}, \mathbf{q}_0^{\text{gen}} \in \mathbb{R}^{|\mathcal{G}|}$, respectively, represent the vectors of apparent, active, and reactive power generations in the base case, while $\mathbf{s}_c^{\text{gen}} \in \mathbb{C}^{|\mathcal{G}|}$, and $\mathbf{p}_c^{\text{gen}}, \mathbf{q}_c^{\text{gen}} \in \mathbb{R}^{|\mathcal{G}|}$ represent the corresponding power generations in a contingency case. Define $\mathbf{p}_c^{\max}, \mathbf{q}_c^{\max} \in \mathbb{R}^{|\mathcal{G}|}$ and $\mathbf{p}_c^{\min}, \mathbf{q}_c^{\min} \in \mathbb{R}^{|\mathcal{G}|}$ as the vectors of the maximum and minimum active and reactive power generations allowed, respectively.

4.2 Enhanced Modeling of Generator Response

In order to capture nonlinear characteristics of power system, such as PV/PQ switching and generator contingency responses, and streamline these response policies, we define the following set.



(a) The characteristics of a pair, $(x, y) \in \mathcal{F}_\theta$, for different slope values. (b) The characteristics of a pair, $(x, y) \in \mathcal{F}_\theta^{\text{smooth}}$, for different slope values.

Figure 25: The characteristics of \mathcal{F}_θ and $\mathcal{F}_\theta^{\text{smooth}}$ when $\theta = 0$, $\theta = \pi/8$, $\theta = \pi/6$, $\theta = \pi/4$.

Definition 2. For every $\theta \in [0, \pi/4)$, define $\mathcal{F}_\theta \in \mathbb{R}^2$ as follows:

$$\begin{aligned}
\mathcal{F}_\theta \triangleq & \left\{ (x, y) \in \mathbb{R}^2 \mid -1 \leq x \leq 1 \right. \\
& \wedge \min\{\max\{0, y - \tan(\theta)x\}, \max\{0, 1 - x\}\} = 0 \\
& \left. \wedge \min\{\max\{0, \tan(\theta)x - y\}, \max\{0, 1 + x\}\} = 0 \right\}, \quad (4.1)
\end{aligned}$$

where θ denotes the slope for a line within the interval $[-1, 1]$. Herein, each pair, (x, y) , represents the coordinates on a piecewise-discontinuous function. In the following section, we will provide a smooth version of \mathcal{F}_θ in order to facilitate a local search algorithm.

4.2.1 Generator Active Power Contingency Response

The active power imbalance due to changes in network configuration, transmission losses, or load profile is supposed to be distributed among other generators within the same area as

$$p_{c,g}^{\text{gen}} = p_{0,g}^{\text{gen}} + \alpha_{c,g} \Delta_c, \quad (4.2)$$

where $p_{c,g}^{\text{gen}}$ is the active power generation of a contingency case, while $p_{0,g}^{\text{gen}}$ is the base case active power generation at generator $g \in \mathcal{G}$. Δ_c represents the amount of redispatch in the contingency case. $\alpha_{c,g}$ denotes weight of contribution to this redispatch by generator $g \in \mathcal{G}$. Herein, if a generator is failed in the contingency, the contingency case active power generation and its contribution to redispatch will be $p_{c,g}^{\text{gen}} = 0$ and $\alpha_{c,g} = 0$, respectively. If a generator is operational but not selected to contribute to redispatch, it maintains its active power generation from the base case, $p_{c,g}^{\text{gen}} = p_{0,g}^{\text{gen}}$.

A generator that contributes to a given contingency readjusts its active power generation as much as its capacity limits permit according to a predefined weight, $\alpha_{c,g}$. In this situation, the active power generation of a corresponding generator will be $p_{c,g}^{\text{gen}} = p_{0,g}^{\text{gen}} + \alpha_{c,g} \Delta_c$. If generator g is about to violate its minimum production or maximum capacity with contribution weight $\alpha_{c,g}$, it must operate at its lower or upper limits based on the contribution requirement. A generator active power contingency response can be expressed using logical functions, mixed-integer programming formulation, and Min-Max operators. The logical functions represent generator active power contingency response using a disjunction of linear constraints as

$$p_{c,g}^{\min} \leq p_{c,g}^{\text{gen}} \leq p_{c,g}^{\max}, \quad p_{c,g}^{\text{gen}} = p_{0,g}^{\text{gen}} + \alpha_{c,g} \Delta_c \quad \forall c \in \mathcal{C}, g \in \mathcal{G}, \quad (4.3a)$$

$$p_{c,g}^{\text{gen}} = p_{c,g}^{\text{max}}, \quad p_{c,g}^{\text{gen}} \leq p_{0,g}^{\text{gen}} + \alpha_{c,g} \Delta_c \quad \forall c \in \mathcal{C}, g \in \mathcal{G}, \quad (4.3b)$$

$$p_{c,g}^{\text{gen}} = p_{c,g}^{\text{min}}, \quad p_{c,g}^{\text{gen}} \geq p_{0,g}^{\text{gen}} + \alpha_{c,g} \Delta_c \quad \forall c \in \mathcal{C}, g \in \mathcal{G}. \quad (4.3c)$$

Another way of formulating (4.3) is to use a mixed-integer programming formulation. Binary variables are introduced to determine the chosen case among logical constraints given in (4.3a)-(4.3c). These three conditions in (4.3) can be expressed as

$$p_{0,g}^{\text{gen}} + \alpha_{c,g} \Delta_c - p_{c,g}^{\text{gen}} \leq M(1 - x_{c,g}^{P^+}) \quad \forall c \in \mathcal{C}, g \in \mathcal{G}, \quad (4.4a)$$

$$p_{c,g}^{\text{gen}} - p_{0,g}^{\text{gen}} - \alpha_{c,g} \Delta_c \leq M(1 - x_{c,g}^{P^-}) \quad \forall c \in \mathcal{C}, g \in \mathcal{G}, \quad (4.4b)$$

$$p_{c,g}^{\text{max}} - p_{c,g}^{\text{gen}} \leq M^P x_{c,g}^{P^+} \quad \forall c \in \mathcal{C}, g \in \mathcal{G}, \quad (4.4c)$$

$$p_{c,g}^{\text{gen}} - p_{c,g}^{\text{min}} \leq M^P x_{c,g}^{P^-} \quad \forall c \in \mathcal{C}, g \in \mathcal{G}. \quad (4.4d)$$

The mixed-integer programming formulation employs big- M method that requires multipliers, M and M^P , to be sufficiently large enough to ensure that (4.4) is equivalent to (4.3). For every $c \in \mathcal{C}$ and $g \in \mathcal{G}$, $x_{c,g}^{P^+}, x_{c,g}^{P^-} \in \{0, 1\}$ denote the introduced binary variables.

Equations (4.4a) and (4.4b), when $x_{c,g}^{P^+} = x_{c,g}^{P^-} = 1$, force $p_{c,g}^{\text{gen}}$ to be equal to or greater than the desired active power response, $p_{0,g}^{\text{gen}} + \alpha_{c,g} \Delta_c$, as represented in (4.3a). Similarly, (4.4c) and (4.4d), when $x_{c,g}^{P^+} = x_{c,g}^{P^-} = 0$, respectively, force $p_{c,g}^{\text{gen}}$ to be equal to $p_{c,g}^{\text{max}}$ and $p_{c,g}^{\text{min}}$.

In addition to (4.3) and (4.4), generator active power contingency response can be expressed using Min and Max operators as

$$p_c^{\text{gen}} = \max\{p_c^{\text{min}}, \min\{C_c(p_0^{\text{gen}} + \alpha_c \Delta_c), p_c^{\text{max}}\}\} \quad \forall c \in \mathcal{C}. \quad (4.5)$$

which can be equivalently formulated based on the defined set (4.1), for every $c \in \mathcal{C}$ and $g \in \mathcal{G}$, as

$$\left(\left(\frac{2p_{c,g}^{\text{gen}} - p_{c,g}^{\text{max}} + p_{c,g}^{\text{min}}}{p_{c,g}^{\text{max}} + p_{c,g}^{\text{min}}} \right), \left(\frac{2(p_{0,g}^{\text{gen}} + \alpha_{c,g}\Delta_c) - p_{c,g}^{\text{max}} + p_{c,g}^{\text{min}}}{p_{c,g}^{\text{max}} + p_{c,g}^{\text{min}}} \right) \right) \in \mathcal{F}_{\frac{\pi}{4}}. \quad (4.6)$$

(4.3)-(4.6) imply a piecewise-discontinuous model as shown in Figure 26(a).

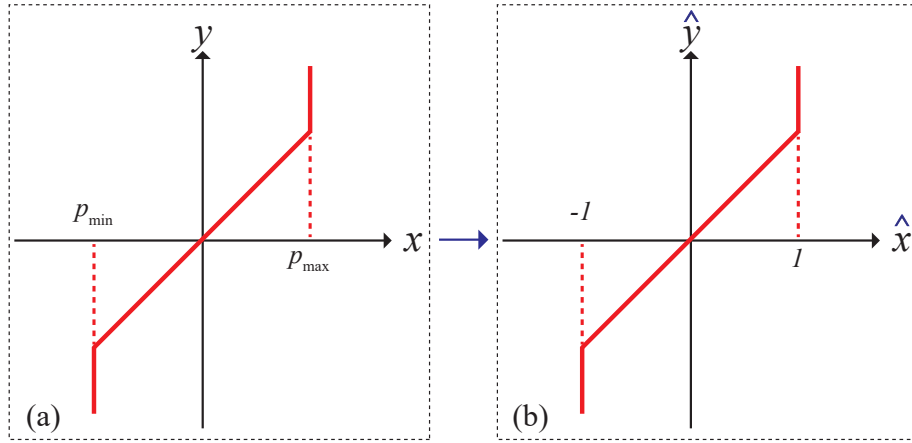


Figure 26: Generator active power response relation between pre- and post-contingency: (a) Actual characteristics: $x = p_{c,g}^{\text{gen}}$, $y = p_{0,g}^{\text{gen}} + \alpha_{c,g}\Delta_c$, (b) Normalization of the actual characteristics: $\hat{x} = \frac{2p_{c,g}^{\text{gen}} - p_{c,g}^{\text{max}} + p_{c,g}^{\text{min}}}{p_{c,g}^{\text{max}} + p_{c,g}^{\text{min}}}$, $\hat{y} = \frac{2(p_{0,g}^{\text{gen}} + \alpha_{c,g}\Delta_c) - p_{c,g}^{\text{max}} + p_{c,g}^{\text{min}}}{p_{c,g}^{\text{max}} + p_{c,g}^{\text{min}}}$.

4.2.2 Generator Reactive Power Contingency Response

A generator that contributes to a given contingency readjusts its reactive power generation to retain the base case voltage magnitude, $|v_0| = |v_c|$, in the contingency case. If the bus voltage magnitude drops below its base-case level, then the generator must operate to provide maximum reactive power. Similarly, if the bus voltage mag-

nitude becomes greater than the base-case level, the generator is supposed to provide minimum reactive power. These can be summarized with logical constraints as

$$q_{c,g}^{\min} \leq q_{c,g}^{\text{gen}} \leq q_{c,g}^{\max}, \quad |v_{c,i}| = |v_{0,i}| \quad \forall c \in \mathcal{C}, g \in \mathcal{G}, i \in \mathcal{N}, \quad (4.7a)$$

$$q_{c,g}^{\text{gen}} = q_{c,g}^{\max}, \quad |v_{c,i}| \leq |v_{0,i}| \quad \forall c \in \mathcal{C}, g \in \mathcal{G}, i \in \mathcal{N}, \quad (4.7b)$$

$$q_{c,g}^{\text{gen}} = q_{c,g}^{\min}, \quad |v_{c,i}| \geq |v_{0,i}| \quad \forall c \in \mathcal{C}, g \in \mathcal{G}, i \in \mathcal{N}. \quad (4.7c)$$

We can formulate (4.7) using mixed-integer programming formulation

$$|v_{0,i}| - |v_{c,i}| \leq M^v(1 - x_{c,g}^{Q^+}) \quad \forall c \in \mathcal{C}, g \in \mathcal{G}, i \in \mathcal{N}, \quad (4.8a)$$

$$|v_{c,i}| - |v_{0,i}| \leq M^v(1 - x_{c,g}^{Q^-}) \quad \forall c \in \mathcal{C}, g \in \mathcal{G}, i \in \mathcal{N}, \quad (4.8b)$$

$$q_{c,g}^{\max} - q_{c,g}^{\text{gen}} \leq M^Q x_{c,g}^{Q^+} \quad \forall c \in \mathcal{C}, g \in \mathcal{G}, i \in \mathcal{N}, \quad (4.8c)$$

$$q_{c,g}^{\text{gen}} - q_{c,g}^{\min} \leq M^Q x_{c,g}^{Q^-} \quad \forall c \in \mathcal{C}, g \in \mathcal{G}, i \in \mathcal{N}. \quad (4.8d)$$

Herein, we have multipliers, M^v and M^Q , to be sufficiently large enough to ensure (4.8) is equivalent to (4.7). For every $c \in \mathcal{C}$ and $g \in \mathcal{G}$, $x_{c,g}^{Q^+}, x_{c,g}^{Q^-} \in \{0, 1\}$ denote the introduced binary variables.

Equations (4.8a) and (4.8b), when $x_{c,g}^{Q^+} = x_{c,g}^{Q^-} = 1$, ensure equality, $|v_{c,i}| = |v_{0,i}|$, as represented in (4.7a). Similarly, (4.8c) and (4.8d), when $x_{c,g}^{Q^+} = x_{c,g}^{Q^-} = 0$, respectively, ensure $q_{c,g}^{\text{gen}}$ to be equal to $q_{c,g}^{\max}$ and $q_{c,g}^{\min}$.

In addition to representation in (4.7) and (4.8), generator reactive power contingency response can be expressed using Min and Max operators as

$$\begin{aligned} & \min \{ \max\{0, \mathbf{G}_c(|\mathbf{v}_0| - |\mathbf{v}_c|)\}, \max\{0, \mathbf{q}_c^{\max} - \mathbf{q}_c^{\text{gen}}\} \} = \\ & \min \{ \max\{0, \mathbf{G}_c(|\mathbf{v}_c| - |\mathbf{v}_0|)\}, \max\{0, \mathbf{q}_c^{\text{gen}} - \mathbf{q}_c^{\min}\} \} = 0 \quad \forall c \in \mathcal{C}. \end{aligned} \quad (4.9)$$

Equation (4.7) can be equivalently formulated based on the defined set (4.1) for every $c \in \mathcal{C}$, $g \in \mathcal{G}$ and $i \in \mathcal{N}$ as

$$\left(\left(\frac{2q_{c,g}^{\text{gen}} - q_{c,g}^{\text{max}} - q_{c,g}^{\text{min}}}{q_{c,g}^{\text{max}} - q_{c,g}^{\text{min}}} \right), (|v_{0,i}| - |v_{c,i}|) \right) \in \mathcal{F}_0. \quad (4.10)$$

These representations, (4.7)-(4.10), refer to the PV/PQ switching as demonstrated in Figure 27(a). Herein, PV bus means that the bus voltage magnitude and the generation level of active power are fixed whereas its voltage phase angle and reactive power generation are varying. When it hits to reactive power capacity limits to sustain the value of voltage magnitude in the base case, the bus type needs to become PQ. This bus type means that the power generations, e.g., real and reactive, are constant, whereas the voltage magnitude and phase angle are varying. Similar to the characteristic of active power, reactive power contingency response implies a piecewise-discontinuous model where its solution space is not only highly nonlinear, but also disconnected.

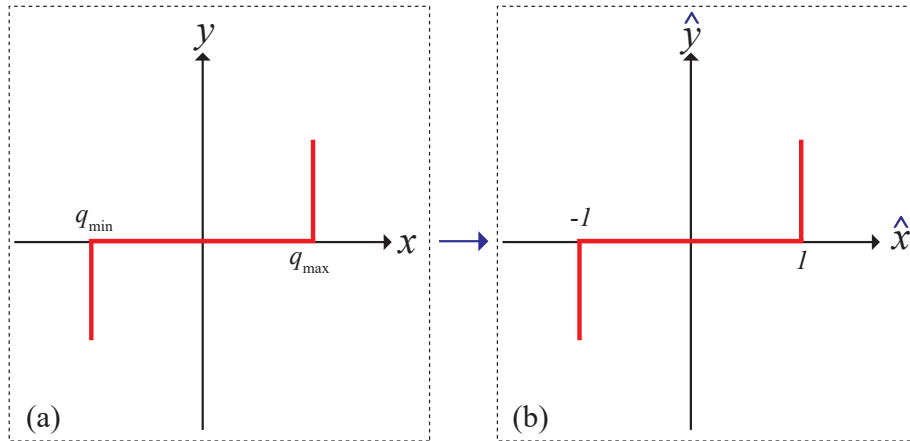


Figure 27: Generator reactive power response relation between pre- and post-contingency: (a) Actual characteristics: $x = q_{c,g}^{\text{gen}}$, $y = |v_{0,i}| - |v_{c,i}|$, (b) Normalization of the actual characteristics: $\hat{x} = \frac{2q_{c,g}^{\text{gen}} - q_{c,g}^{\text{max}} - q_{c,g}^{\text{min}}}{q_{c,g}^{\text{max}} - q_{c,g}^{\text{min}}}$, $\hat{y} = |v_{0,i}| - |v_{c,i}|$.

4.3 Security-constrained Optimal Power Flow

This section elaborates the active and reactive power contingency response models. Herein, devised objective function minimizes the generational cost in the base case and provides immunity to the power grid in response to contingency scenarios.

4.3.1 Undifferentiable Problem Formulation

SCOPF with respect to outage of a random number of generators or lines can be formulated as

$$\text{minimize} \quad h(\mathbf{p}_0^{\text{gen}}) \quad (4.11\text{a})$$

$$\begin{aligned} \text{subject to} \quad & \mathbf{s}_c^{\text{dem}} + \text{diag}\{\mathbf{v}_c \mathbf{v}_c^* \mathbf{Y}_c^*\} \\ & = \mathbf{G}_c^\top (\mathbf{p}_c^{\text{gen}} + i \mathbf{q}_c^{\text{gen}}) \quad \forall c \in \mathcal{C} \end{aligned} \quad (4.11\text{b})$$

$$|\text{diag}\{\tilde{\mathbf{L}}_c \mathbf{v}_c \mathbf{v}_c^* \tilde{\mathbf{Y}}_c^*\}| \leq \mathbf{s}_c^{\text{max}} \quad \forall c \in \mathcal{C} \quad (4.11\text{c})$$

$$|\text{diag}\{\tilde{\mathbf{L}}_c \mathbf{v}_c \mathbf{v}_c^* \tilde{\mathbf{Y}}_c^*\}| \leq \mathbf{s}_c^{\text{max}} \quad \forall c \in \mathcal{C} \quad (4.11\text{d})$$

$$\mathbf{p}_c^{\text{min}} \leq \mathbf{p}_c^{\text{gen}} \leq \mathbf{p}_c^{\text{max}} \quad \forall c \in \mathcal{C} \quad (4.11\text{e})$$

$$\mathbf{q}_c^{\text{min}} \leq \mathbf{q}_c^{\text{gen}} \leq \mathbf{q}_c^{\text{max}} \quad \forall c \in \mathcal{C} \quad (4.11\text{f})$$

$$\mathbf{v}^{\text{min}} \leq |\mathbf{v}_c| \leq \mathbf{v}^{\text{max}} \quad \forall c \in \mathcal{C} \quad (4.11\text{g})$$

$$\left(\left(\frac{2\mathbf{p}_c^{\text{gen}} - \mathbf{p}_c^{\text{max}} + \mathbf{p}_c^{\text{min}}}{\mathbf{p}_c^{\text{max}} + \mathbf{p}_c^{\text{min}}} \right), \left(\frac{2\mathbf{C}_c(\mathbf{p}_0^{\text{gen}} + \boldsymbol{\alpha}_c \Delta_c) - \mathbf{p}_c^{\text{max}} + \mathbf{p}_c^{\text{min}}}{\mathbf{p}_c^{\text{max}} + \mathbf{p}_c^{\text{min}}} \right) \right) \in \mathcal{F}_{\frac{\pi}{4}}, \forall c \in \mathcal{C} \quad (4.11\text{h})$$

$$\left(\left(\frac{2\mathbf{q}_c^{\text{gen}} - \mathbf{q}_c^{\text{max}} - \mathbf{q}_c^{\text{min}}}{\mathbf{q}_c^{\text{max}} - \mathbf{q}_c^{\text{min}}} \right), (\mathbf{G}_c(|\mathbf{v}_0| - |\mathbf{v}_c|)) \right) \in \mathcal{F}_0, \forall c \in \mathcal{C} \quad (4.11\text{i})$$

$$\text{variables} \quad \mathbf{p}_0^{\text{gen}}, \mathbf{p}_c^{\text{gen}}, \mathbf{q}_c^{\text{gen}}, \boldsymbol{\alpha}_c \in \mathbb{R}^{|\mathcal{G}|}; \mathbf{v}_0, \mathbf{v}_c \in \mathbb{C}^{|\mathcal{N}|}; \Delta_c \in \mathbb{R}$$

where (4.11a) represents the cost of producing power in the base case. (4.11b) fulfills the apparent power balances in the network, whereas (4.11c)–(4.11d) enforce the apparent power flow limits for transmission lines. (4.11e)–(4.11f) represent the generation boundaries for active and reactive power. The inequality (4.11g) limits the nodal voltage magnitude. Equation (4.11h) represents coupling constraints on generators that relate pre- and post-contingency active power dispatch, while (4.11i) stands for the coupling constraints that relate pre- and post-contingency reactive power dispatch with respect to generator capacity limits. It should be noted that (4.11h) and (4.11i) are the normalized versions of (4.3) and (4.7), respectively. (4.11h) and (4.11i) have made the solution to eh SCOPF problem challenging since they are not differentiable. The main reason behind the normalizations is to make use of sigmoid functions that transform values on $(-\infty, \infty)$ into numbers $(-1, 1)$ so that (4.11h) and (4.11i) can be represented in a differentiable model. Accordingly, inverse sigmoid functions transfer values on $(-1, 1)$ into numbers on $(-\infty, \infty)$. Figures 26(b) and 27(b) visualize these normalizations. In the following part, we will introduce several equivalent continuously-differentiable models using inverse sigmoid functions instead of (4.11h) and (4.11i).

4.3.2 Smoothed Version of the Problem Formulation

The set defined in (4.1) implies a nondifferentiable model. We define $\mathcal{F}_\theta^{\text{smooth}}$ to obtain a continuously-differentiable model of generator contingency responses. To this end, the piecewise-discontinuous functions, (4.11h) and (4.11i), can be approximated with continuously-differentiable curves whose coordinates satisfy the smoothed set $\mathcal{F}_\theta^{\text{smooth}}$ as

$$\left(\left(\frac{2p_{c,g}^{\text{gen}} - p_{c,g}^{\text{max}} + p_{c,g}^{\text{min}}}{p_{c,g}^{\text{max}} + p_{c,g}^{\text{min}}} \right), \left(\frac{2(p_{0,g}^{\text{gen}} + \alpha_{c,g}\Delta_c) - p_{c,g}^{\text{max}} + p_{c,g}^{\text{min}}}{p_{c,g}^{\text{max}} + p_{c,g}^{\text{min}}} \right) \right) \in \mathcal{F}_{\frac{\pi}{4}}^{\text{smooth}}, \quad (4.12a)$$

$$\left(\left(\frac{2q_{c,g}^{\text{gen}} - q_{c,g}^{\text{max}} - q_{c,g}^{\text{min}}}{q_{c,g}^{\text{max}} - q_{c,g}^{\text{min}}} \right), (|v_{0,i}| - |v_{c,i}|) \right) \in \mathcal{F}_0^{\text{smooth}}. \quad (4.12b)$$

Equation (4.13) introduces an activation function to integrate approximated curves instead of piecewise-discontinuous functions.

$$f_{\theta}(x) = h^{-1}(a(x) - x)x^{2k} + \tan(\theta) x, \quad (4.13)$$

where h denotes a smoothing factor that regulates the closeness of a candidate curve to the actual function, while θ is the angle of curve at the origin. k denotes the order of approximation. The effects of different h values, while $\theta = \pi/4$ and $\theta = 0$, on (4.14a)-(4.14e) are shown in Figures 28 and 29, respectively. This function, (4.13), approximates discrete characteristic of a nerve cell operation by a continuous function. The candidate curve, $a(x)$, chosen among (4.14a) and (4.14e) replaces piecewise-discontinuous functions, (4.11h) and (4.11i), with continuously-differentiable functions.

$$a(x) = \frac{\log(1+x) - \log(1-x)}{2} \quad (4.14a)$$

$$a(x) = \frac{2}{\pi} \tan\left(\frac{\pi x}{2}\right) \quad (4.14b)$$

$$a(x) = \frac{x}{\sqrt{1-x^2}} \quad (4.14c)$$

$$a(x) = \frac{2\text{ierf}(x)}{\sqrt{\pi}} \quad (4.14d)$$

$$a(x) = \frac{x}{1-|x|} \quad (4.14e)$$

The candidate curves given in (4.14) include inverse hyperbolic tangent (4.14a), inverse arctangent (4.14b), inverse algebraic (4.14c), inverse error (4.14d), and inverse absolute value functions.

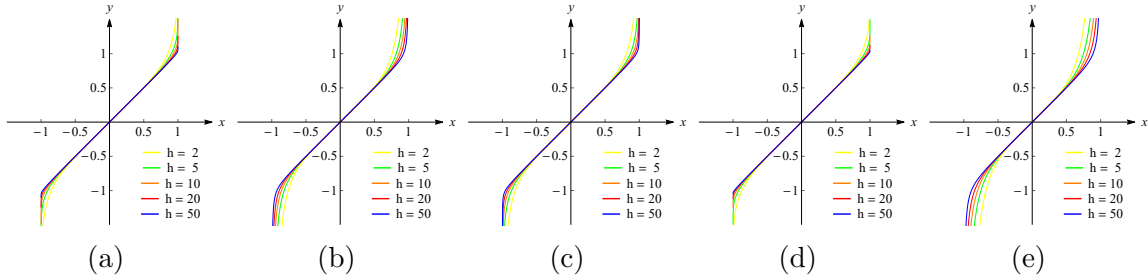


Figure 28: The characteristics of $(x, y) \in \mathcal{F}_{\pi/4}^{\text{smooth}}$ for different h values with the candidate curves (a) (4.14a), (b) (4.14b), (c) (4.14c), (d) (4.14d), (e) (4.14e).

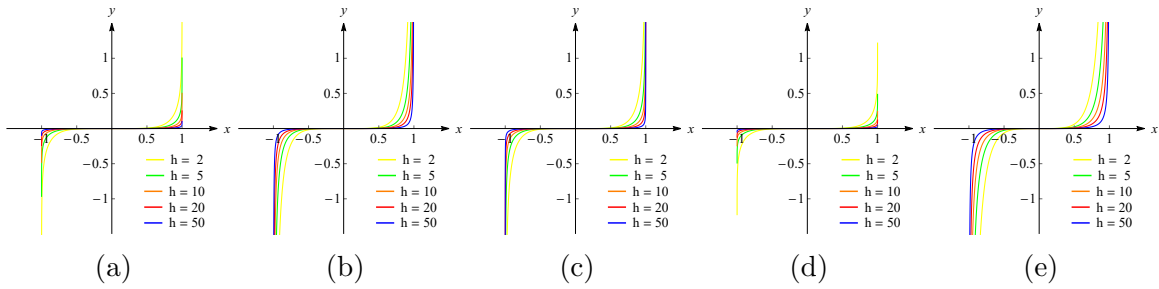


Figure 29: The characteristics of $(x, y) \in \mathcal{F}_0^{\text{smooth}}$ for different h values with the candidate curves (a) (4.14a), (b) (4.14b), (c) (4.14c), (d) (4.14d), (e) (4.14e).

4.4 Case Studies

Numerical studies on an IEEE 30-bus system study the efficacy of the continuously-differentiable SCOPF model. The main purpose is to minimize pre-contingency power generation cost while ensuring the secure post-contingency operation. The secure operation prevents physical and operational violations by means of optimally, allocating active power imbalances among available generators and deciding the type of bus, i.e., PV/PQ switching, respectively. To this end, we consider several numerical experiments on the IEEE benchmark under an extensive list of contingency scenarios, each representing the outage of randomly chosen components, e.g., generator or line. Herein, it is ensured that randomly-chosen lines do not lead to an islanding in the power grid. These studies are examined on a PC with 16-core, Xeon processor, and

256 GB RAM using Matpower interior point solver (MIPS) [112]. The allowable feasibility violation is set to 10^{-6} for the obtained solution of given scenarios in Table 2.

The IEEE benchmark considered has 30 buses connected with 41 transmission lines, 6 generators, and 20 loads. Herein, bus 1 is assigned as the slack bus; buses 2, 13, 22, 23, 27 are PV buses, and the rest are PQ buses. Consider this IEEE 30-bus system under 12 contingency scenarios as described in Table 2. To maintain system reliability under certain contingencies, the benchmark data is changed by reducing the load demand in half. Hence, solution to the OPF problem with no contingency results in a minimum generation cost of 2847.8. Considering contingency cases in Table 2 using (4.14a) increases the cost during normal conditions by 11.24% to 3167.9. Tables 3-5 represent active power, reactive power, and voltage variations of the power grid in response to given contingencies. The proposed method distributes network's active power imbalance complying with (4.3), which is due to the outage of a network component, among available generators given in Table 3. It can be observed from Table 3 that the outage of a transmission line, scenarios 7-12, does not cause a considerable power redispatch. Table 4 and 5 represent the reactive power and voltage relations in the case of a network component outage. It is expected that the PV buses maintain their base case voltage levels during contingencies as much as their capacity limits permit. The highlighted values in red color, for the scenarios 1-6, in the Table 5 refer to the PV/PQ switching due to a generator outage. It should be noted that the outage of a transmission line, for the scenarios 7-12, does not require PV/PQ switching as reported in the Table 5.

Table 6 reports the performance comparison in terms of the objective value and required time to solve the proposed continuously-differentiable functions (4.14a)-(4.14e). It can be inferred that (4.14a) and (4.14d) offer the most promising approximations in terms of objective values while others, (4.14b), (4.14c), (4.14e) successfully

recover the feasible solution considering the generator response in the case of a randomly chosen component outage.

Table 2: List of Contingencies for IEEE 30-bus system

Contingency Number	Generator Number	Line Number
1	5	-
2	6	-
3	1	-
4	4	-
5	3	-
6	2	-
7	-	2
8	-	25
9	-	20
10	-	35
11	-	9
12	-	1

Table 3: Active power variations in response to contingency scenarios (pu)

Sc. Nr. Bus Nr.	0	1	2	3	4	5	6	7	8	9	10	11	12
1	0.2880	0.2946	0.2945	0	0.2894	0.3152	0.3541	0.2878	0.2875	0.2874	0.2874	0.2874	0.2875
2	0.4073	0.4131	0.4130	0.4488	0.4085	0.4311	0	0.4072	0.4069	0.4068	0.4068	0.4068	0.4069
22	0.1755	0.1788	0.1788	0.1992	0.1762	0	0.2086	0.1755	0.1753	0.1752	0.1752	0.1752	0.1753
27	0.0077	0.0208	0.0206	0.0850	0	0.0528	0.1152	0.0109	0.0105	0.0102	0.0103	0.0103	0.0105
23	0.0386	0	0.0484	0.1096	0.0408	0.0794	0.1376	0.0385	0.0381	0.0379	0.0379	0.0379	0.0381
13	0.0375	0.0478	0	0.1085	0.0401	0.0783	0.1365	0.0378	0.0374	0.0371	0.0371	0.0371	0.0374

Table 4: Reactive power variations in response to contingency scenarios (pu)

Sc. Nr. Bus Nr.	0	1	2	3	4	5	6	7	8	9	10	11	12
1	-0.0888	-0.0298	-0.0216	0	-0.0257	-0.0245	0.0243	-0.0599	-0.0296	-0.0298	-0.0299	-0.0316	-0.0306
2	0.1016	0.0500	0.0861	0.0345	0.0743	0.1011	0	0.0795	0.0454	0.0463	0.0459	0.0674	0.0886
22	0.1358	0.1554	0.1736	0.1425	0.1603	0	0.1587	0.1447	0.1164	0.1340	0.1470	0.1301	0.1337
27	0.0748	0.0762	0.0750	0.0604	0	0.0905	0.0628	0.0789	0.0729	0.0732	0.0509	0.0709	0.0728
23	0.0356	0	0.0817	0.0024	0.0498	0.0812	-0.0074	0.0392	0.0520	0.0361	0.0465	0.0354	0.0355
13	0.1360	0.1450	0	0.1375	0.1371	0.1569	0.1443	0.1428	0.1399	0.1345	0.1339	0.1333	0.1336

Table 5: Voltage variations in response to contingency scenarios (pu). Values in red color refer to the PV/PQ switching due to a generator outage.

Sc. Nr. Bus Nr.	0	1	2	3	4	5	6	7	8	9	10	11	12
1	1.0462	1.0490	1.0488	1.0469	1.0489	1.0489	1.0479	1.0500	1.0490	1.0490	1.0490	1.0491	1.0491
2	1.0471	1.0472	1.0471	1.0472	1.0471	1.0471	1.0471	1.0471	1.0472	1.0472	1.0472	1.0471	1.0471
22	1.0488	1.0488	1.0488	1.0488	1.0488	1.0488	1.0488	1.0488	1.0488	1.0488	1.0488	1.0488	1.0488
27	1.0489	1.0489	1.0489	1.0490	1.0273	1.0489	1.0490	1.0489	1.0489	1.0489	1.0490	1.0489	1.0489
23	1.0470	1.0374	1.0470	1.0471	1.0471	1.0470	1.0471	1.0471	1.0471	1.0471	1.0471	1.0471	1.0471
13	1.0665	1.0665	1.0326	1.0665	1.0665	1.0665	1.0665	1.0665	1.0665	1.0665	1.0665	1.0665	1.0665

Table 6: Performance Comparison of the Proposed Functions

Continuously-differentiable Function	Objective Value	Required Time (s)
Inverse hyperbolic tangent (4.14a)	3167.9	6.32
Inverse arctangent (4.14b)	3168.6	6.25
Inverse algebraic (4.14c)	3168.1	6.44
Inverse error (4.14d)	3167.8	6.86
Inverse absolute value (4.14e)	3169.1	7.60

4.5 Summary

This chapter tackles the SCOPF problem with piecewise-discontinuous model of generator active and reactive power contingency responses by means of several equivalent continuously-differentiable models. The proposed approach provides state and decision variables to ensure continuity of power grid operation even under contingencies. The problem is resulted in a nonlinear programming formulation, and involves piecewise-discontinuous models due to the active and reactive power contingency characteristics. We replace these undifferentiable functions with several equivalent continuously-differentiable surrogates that are tractable and can be solved with various numerical solvers. The solution of the proposed models are verified via numerical studies on an IEEE benchmark.

CHAPTER 5

CONCLUSION AND FUTURE WORKS

This work offers a variety of applications for high performance optimization in the context of emerging power systems. The research outcomes are outlined below:

- A convex optimization framework is proposed to solve the grid topology-cognizant OPF problem for MTDC grids. It provides local voltage and power set-points for droop controllers of VSCs as well as the operational status of transmission lines. Additional constraints, that sustain safe operation in response to the power fluctuation in between two droop updates, are integrated into the proposed formulation. The resulting formulation has computational difficulties due to the non-convex power balance, flow and converter loss equations as well as the inclusion of binary decision variables. Convex relaxation methods are utilized to transform this problem into a tractable model so that it can be executed with off-the-shelf solvers.
- The convex optimization approach is developed to solve the state estimation and topology identification problems using only a limited number of measurement for converter-augmented DC networks. This problem is formulated as a constrained minimization problem, where a proper choice of objective function obviates any tuning coefficient in the absence of measurement noise. The problem formulation is then extended for the noisy measurements by adding auxiliary variables to account for convex regularization terms in the objective

function. The proposed method is studied where the set of measurements are: (i) voltage values at some of the randomly-chosen buses, (ii) current-injection values at some of the randomly-chosen buses, and (iii) some of the line statuses. With the help of an additional set of measurements, this solution can handle scenarios where each measurement is corrupted either by zero-mean Gaussian noises with 1% standard deviation or 100% of the corresponding original values.

- SCOPF problem that considers piecewise-discontinuous model of generator active and reactive power contingency responses by means of several equivalent continuously-differentiable models is studied. The proposed approach provides state and decision variables to ensure continuity of power grid operation even under contingencies. The problem is expressed as a nonlinear programming formulation and involves piecewise-discontinuous models due to the active and reactive power contingency characteristics. We replace this undifferentiable functions with several equivalent continuously-differentiable surrogates that are tractable and can be solved with various numerical solvers.

Future works may focus on developing distributed optimization framework for ensuring secure and cost-efficient solutions in DC and/or AC network reconfiguration problems.

REFERENCES

- [1] S. H. Low, “Convex relaxation of optimal power flow—part i: Formulations and equivalence,” *IEEE Transactions on Control of Network Systems*, vol. 1, no. 1, pp. 15–27, March 2014.
- [2] S. H. Low, “Convex relaxation of optimal power flow—part ii: Exactness,” *IEEE Transactions on Control of Network Systems*, vol. 1, no. 2, pp. 177–189, June 2014.
- [3] R. Madani, S. Sojoudi, and J. Lavaei, “Convex relaxation for optimal power flow problem: Mesh networks,” *IEEE Transactions on Power Systems*, vol. 30, no. 1, pp. 199–211, Jan 2015.
- [4] B. Kocuk, S. S. Dey, and X. A. Sun, “Strong socp relaxations for the optimal power flow problem,” *Operations Research*, vol. 64, no. 6, pp. 1177–1196, 2016.
- [5] K. W. Hedman, S. S. Oren, and R. P. O’Neill, “A review of transmission switching and network topology optimization,” in *2011 IEEE Power and Energy Society General Meeting*, July 2011, pp. 1–7.
- [6] K. W. Hedman, R. P. O’Neill, E. B. Fisher, and S. S. Oren, “Optimal transmission switching—sensitivity analysis and extensions,” *IEEE Transactions on Power Systems*, vol. 23, no. 3, pp. 1469–1479, Aug 2008.
- [7] B. Kocuk, S. S. Dey, and X. A. Sun, “New formulation and strong misocp relaxations for ac optimal transmission switching problem,” *IEEE Transactions on Power Systems*, vol. 32, no. 6, pp. 4161–4170, Nov 2017.

- [8] A. Gholami and X. A. Sun, “Towards resilient operation of multimicrogrids: An misocp-based frequency-constrained approach,” *IEEE Transactions on Control of Network Systems*, vol. 6, no. 3, pp. 925–936, Sep. 2019.
- [9] A. Monticelli, *State estimation in electric power systems: a generalized approach*. Springer Science & Business Media, 2012.
- [10] G. Wang, H. Zhu, G. B. Giannakis, and J. Sun, “Robust power system state estimation from rank-one measurements,” *IEEE Transactions on Control of Network Systems*, pp. 1–1, 2019.
- [11] Y. Lin and A. Abur, “Robust state estimation against measurement and network parameter errors,” *IEEE Transactions on Power Systems*, vol. 33, no. 5, pp. 4751–4759, Sep. 2018.
- [12] G. He, S. Dong, J. Qi, and Y. Wang, “Robust state estimator based on maximum normal measurement rate,” *IEEE Transactions on Power Systems*, vol. 26, no. 4, pp. 2058–2065, Nov 2011.
- [13] V. Kekatos and G. B. Giannakis, “Distributed robust power system state estimation,” *IEEE Transactions on Power Systems*, vol. 28, no. 2, pp. 1617–1626, May 2013.
- [14] M. Göl and A. Abur, “Lav based robust state estimation for systems measured by pmus,” *IEEE Transactions on Smart Grid*, vol. 5, no. 4, pp. 1808–1814, July 2014.
- [15] Y. Weng, R. Negi, C. Faloutsos, and M. D. Ilić, “Robust data-driven state estimation for smart grid,” *IEEE Transactions on Smart Grid*, vol. 8, no. 4, pp. 1956–1967, July 2017.
- [16] A. Gomez-Exposito and A. Abur, *Power System State Estimation: Theory and Implementation*. CRC press, 2004.

- [17] H. Zhu and G. B. Giannakis, “Estimating the state of ac power systems using semidefinite programming,” in *2011 North American Power Symposium*, Aug 2011, pp. 1–7.
- [18] Y. Weng, Q. Li, R. Negi, and M. Ilić, “Semidefinite programming for power system state estimation,” in *2012 IEEE Power and Energy Society General Meeting*, July 2012, pp. 1–8.
- [19] Y. Zhang, R. Madani, and J. Lavaei, “Conic relaxations for power system state estimation with line measurements,” *IEEE Transactions on Control of Network Systems*, vol. 5, no. 3, pp. 1193–1205, Sep. 2018.
- [20] R. Madani, J. Lavaei, R. Baldick, and A. Atamtürk, “Power system state estimation and bad data detection by means of conic relaxation,” in *Proceedings of the 50th Hawaii International Conference on System Sciences*, 2017.
- [21] R. Madani, M. Ashraphijuo, J. Lavaei, and R. Baldick, “Power system state estimation with a limited number of measurements,” in *2016 IEEE 55th Conference on Decision and Control (CDC)*, Dec 2016, pp. 672–679.
- [22] R. Madani, J. Lavaei, and R. Baldick, “Convexification of power flow equations in the presence of noisy measurements,” *IEEE Transactions on Automatic Control*, pp. 1–1, 2019.
- [23] A. Sabati, K. Basaran, R. Bayindir, S. Padmanaban, P. Siano, and Z. Leonowicz, “Investigating the effects of selecting different slack bus on power systems,” in *2017 IEEE International Conference on Environment and Electrical Engineering and 2017 IEEE Industrial and Commercial Power Systems Europe (EEEIC / I CPS Europe)*, June 2017, pp. 1–6.
- [24] D. P. Kothari, I. Nagrath *et al.*, *Modern Power System Analysis*. Tata McGraw-Hill Education, 2011.

- [25] J. J. Thomas and S. Grijalva, “Flexible security-constrained optimal power flow,” *IEEE Transactions on Power Systems*, vol. 30, no. 3, pp. 1195–1202, 2015.
- [26] M. Andreasson, D. V. Dimarogonas, H. Sandberg, and K. H. Johansson, “Distributed controllers for multiterminal hvdc transmission systems,” *IEEE Transactions on Control of Network Systems*, vol. 4, no. 3, pp. 564–574, Sep. 2017.
- [27] D. Van Hertem and M. Ghandhari, “Multi-terminal vsc hvdc for the european supergrid: Obstacles,” *Renewable and sustainable energy reviews*, vol. 14, no. 9, pp. 3156–3163, 2010.
- [28] A. Yazdani and R. Iravani, *Voltage-sourced converters in power systems*. Wiley Online Library, 2010, vol. 34.
- [29] N. Yousefpoor, S. Kim, and S. Bhattacharya, “Multi-terminal dc grid control under loss of terminal station,” in *2014 IEEE Energy Conversion Congress and Exposition (ECCE)*, Sept 2014, pp. 744–749.
- [30] J. Beerten, S. Cole, and R. Belmans, “Modeling of multi-terminal vsc hvdc systems with distributed dc voltage control,” *IEEE Transactions on Power Systems*, vol. 29, no. 1, pp. 34–42, Jan 2014.
- [31] K. Rouzbehi, A. Miranian, J. I. Candela, A. Luna, and P. Rodriguez, “A generalized voltage droop strategy for control of multiterminal dc grids,” *IEEE Transactions on Industry Applications*, vol. 51, no. 1, pp. 607–618, Jan 2015.
- [32] C. Gavriluta, J. I. Candela, J. Rocabert, A. Luna, and P. Rodriguez, “Adaptive droop for control of multiterminal dc bus integrating energy storage,” *IEEE Transactions on Power Delivery*, vol. 30, no. 1, pp. 16–24, Feb 2015.
- [33] S. Shin, P. Hart, T. Jahns, and V. M. Zavala, “A hierarchical optimization architecture for large-scale power networks,” *IEEE Transactions on Control of Network Systems*, vol. 6, no. 3, pp. 1004–1014, Sep. 2019.

- [34] Q. Nguyen, G. Todeschini, and S. Santoso, “Power flow in a multi-frequency hvac and hvdc system: Formulation, solution, and validation,” *IEEE Transactions on Power Systems*, vol. 34, no. 4, pp. 2487–2497, July 2019.
- [35] M. A. Abdelwahed and E. F. El-Saadany, “Power sharing control strategy of multiterminal VSC-HVDC transmission systems utilizing adaptive voltage droop,” *IEEE Transactions on Sustainable Energy*, vol. 8, no. 2, pp. 605–615, April 2017.
- [36] T. M. Haileselassie and K. Uhlen, “Impact of dc line voltage drops on power flow of mt dc using droop control,” *IEEE Transactions on Power Systems*, vol. 27, no. 3, pp. 1441–1449, Aug 2012.
- [37] L. Xiao, Z. Xu, T. An, and Z. Bian, “Improved analytical model for the study of steady state performance of droop-controlled VSC-MTDC systems,” *IEEE Transactions on Power Systems*, 2016.
- [38] A. Nikoobakht, J. Aghaei, T. Niknam, V. Vahidinasab, H. Farahmand, and M. Korpås, “Towards robust opf solution strategy for the future ac/dc grids: case of VSC-HVDC-connected offshore wind farms,” *IET Renewable Power Generation*, vol. 12, no. 6, pp. 691–701, 2018.
- [39] F. Sun, J. Ma, M. Yu, and W. Wei, “A robust optimal coordinated droop control method for multiple vscs in ac-dc distribution network,” *IEEE Transactions on Power Systems*, pp. 1–1, 2019.
- [40] B. Li, Q. Li, Y. Wang, W. Wen, B. Li, and L. Xu, “A novel method to determine droop coefficients of dc voltage control for VSC-MTDC system,” *IEEE Transactions on Power Delivery*, pp. 1–1, 2020.
- [41] C. Gavriluta, I. Candela, A. Luna, A. Gomez-Exposito, and P. Rodriguez, “Hierarchical control of hv-mt dc systems with droop-based primary and opf-based

- secondary,” *IEEE Transactions on Smart Grid*, vol. 6, no. 3, pp. 1502–1510, May 2015.
- [42] W. Feng, L. A. Tuan, L. B. Tjernberg, A. Mannikoff, and A. Bergman, “A new approach for benefit evaluation of multiterminal vsc-hvdc using a proposed mixed ac/dc optimal power flow,” *IEEE Transactions on Power Delivery*, vol. 29, no. 1, pp. 432–443, Feb 2014.
- [43] S. Bahrami, F. Therrien, V. W. S. Wong, and J. Jatskevich, “Semidefinite relaxation of optimal power flow for ac–dc grids,” *IEEE Transactions on Power Systems*, vol. 32, no. 1, pp. 289–304, Jan 2017.
- [44] M. Baradar, M. R. Hesamzadeh, and M. Ghandhari, “Second-order cone programming for optimal power flow in VSC-Type ac-dc grids,” *IEEE Transactions on Power Systems*, vol. 28, no. 4, pp. 4282–4291, Nov 2013.
- [45] H. Ergun, J. Dave, D. Van Hertem, and F. Geth, “Optimal power flow for ac–dc grids: Formulation, convex relaxation, linear approximation, and implementation,” *IEEE Transactions on Power Systems*, vol. 34, no. 4, pp. 2980–2990, July 2019.
- [46] J. Dave, H. Ergun, T. An, J. Lu, and D. Van Hertem, “Tnep of meshed hvdc grids: ‘ac’, ‘dc’ and convex formulations,” *IET Generation, Transmission Distribution*, vol. 13, no. 24, pp. 5523–5532, 2019.
- [47] T. Altun, R. Madani, A. P. Yadav, A. Nasir, and A. Davoudi, “Optimal re-configuration of dc networks,” *IEEE Transactions on Power Systems*, pp. 1–1, 2020.
- [48] K. W. Hedman, R. P. O’Neill, E. B. Fisher, and S. S. Oren, “Optimal transmission switching with contingency analysis,” *IEEE Transactions on Power Systems*, vol. 24, no. 3, pp. 1577–1586, Aug 2009.

- [49] S. Binato, M. V. F. Pereira, and S. Granville, “A new benders decomposition approach to solve power transmission network design problems,” *IEEE Transactions on Power Systems*, vol. 16, no. 2, pp. 235–240, 2001.
- [50] F. Zohrizadeh, M. Kheirandishfard, E. Q. Jnr, and R. Madani, “Penalized parabolic relaxation for optimal power flow problem,” in *2018 IEEE Conference on Decision and Control (CDC)*, Dec 2018, pp. 1616–1623.
- [51] R. Madani, M. Kheirandishfard, J. Lavaei, and A. Atamturk, “Penalized semidefinite programming for quadratically-constrained quadratic optimization,” 2020.
- [52] T. K. Vrana, Y. Yang, D. Jovcic, S. Dennetière, J. Jardini, and H. Saad, “The cigre b4 dc grid test system,” *Electra*, vol. 270, no. 1, pp. 10–19, 2013.
- [53] M. Grant and S. Boyd, “CVX: Matlab software for disciplined convex programming, version 2.1,” <http://cvxr.com/cvx>, Mar. 2014.
- [54] L. Gurobi Optimization, “Gurobi optimizer reference manual,” 2018. [Online]. Available: <http://www.gurobi.com>
- [55] A. Monticelli, “Electric power system state estimation,” *Proceedings of the IEEE*, vol. 88, no. 2, pp. 262–282, Feb 2000.
- [56] E. Caro, A. J. Conejo, and A. Abur, “Breaker status identification,” *IEEE Transactions on Power Systems*, vol. 25, no. 2, pp. 694–702, May 2010.
- [57] G. N. Korres and P. J. Katsikas, “Identification of circuit breaker statuses in wls state estimator,” *IEEE Transactions on Power Systems*, vol. 17, no. 3, pp. 818–825, Aug 2002.
- [58] O. Alsac, N. Vempati, B. Stott, and A. Monticelli, “Generalized state estimation,” *IEEE Transactions on Power Systems*, vol. 13, no. 3, pp. 1069–1075, Aug 1998.

- [59] V. Kekatos and G. B. Giannakis, “Joint power system state estimation and breaker status identification,” in *2012 North American Power Symposium (NAPS)*, Sep. 2012, pp. 1–6.
- [60] Y. Yuan, O. Ardakanian, S. Low, and C. Tomlin, “On the inverse power flow problem,” *arXiv preprint arXiv:1610.06631*, 2016.
- [61] Y. Wu, M. Kezunovic, and T. Kostic, “Cost minimization in power system measurement placement,” in *2006 International Conference on Power System Technology*, Oct 2006, pp. 1–6.
- [62] A. Monticelli and F. F. Wu, “Network observability: Identification of observable islands and measurement placement,” *IEEE Transactions on Power Apparatus and Systems*, vol. PAS-104, no. 5, pp. 1035–1041, May 1985.
- [63] N. G. Bretas, “Network observability: theory and algorithms based on triangular factorisation and path graph concepts,” *IEE Proceedings - Generation, Transmission and Distribution*, vol. 143, no. 1, pp. 123–128, Jan 1996.
- [64] B. Gou and A. Abur, “A direct numerical method for observability analysis,” *IEEE Transactions on Power Systems*, vol. 15, no. 2, pp. 625–630, May 2000.
- [65] B. Gou, “Jacobian matrix-based observability analysis for state estimation,” *IEEE Transactions on Power Systems*, vol. 21, no. 1, pp. 348–356, Feb 2006.
- [66] H. R. de Oliveira Rocha, J. C. S. de Souza, and M. B. Do Coutto Filho, “Planning high quality metering systems for state estimation through a constructive heuristic,” *International Journal of Electrical Power & Energy Systems*, vol. 52, pp. 34–41, 2013.
- [67] Z. Wu, X. Du, W. Gu, Y. Liu, P. Ling, J. Liu, and C. Fang, “Optimal pmu placement considering load loss and relaying in distribution networks,” *IEEE Access*, vol. 6, pp. 33 645–33 653, 2018.

- [68] N. M. Manousakis and G. N. Korres, “An advanced measurement placement method for power system observability using semidefinite programming,” *IEEE Systems Journal*, vol. 12, no. 3, pp. 2601–2609, Sep. 2018.
- [69] S. Bhela, V. Kekatos, and S. Veeramachaneni, “Enhancing observability in distribution grids using smart meter data,” *IEEE Transactions on Smart Grid*, vol. 9, no. 6, pp. 5953–5961, Nov 2018.
- [70] K. A. Clements, “The impact of pseudo-measurements on state estimator accuracy,” in *2011 IEEE Power and Energy Society General Meeting*, July 2011, pp. 1–4.
- [71] K. Dehghanpour, Z. Wang, J. Wang, Y. Yuan, and F. Bu, “A survey on state estimation techniques and challenges in smart distribution systems,” *IEEE Transactions on Smart Grid*, vol. 10, no. 2, pp. 2312–2322, March 2019.
- [72] A. J. Schmitt, A. Bernstein, and Y. Zhang, “Matrix completion for low-observability voltage estimation,” *arXiv preprint arXiv:1801.09799*, 2018.
- [73] J. Comden, A. Bernstein, and Z. Liu, “Sample complexity of power system state estimation using matrix completion,” *arXiv preprint arXiv:1905.01789*, 2019.
- [74] Y. Sharon, A. M. Annaswamy, A. L. Motto, and A. Chakraborty, “Topology identification in distribution network with limited measurements,” in *2012 IEEE PES Innovative Smart Grid Technologies (ISGT)*, Jan 2012, pp. 1–6.
- [75] L. Zhao, W. Song, L. Tong, Y. Wu, and J. Yang, “Topology identification in smart grid with limited measurements via convex optimization,” in *2014 IEEE Innovative Smart Grid Technologies - Asia (ISGT ASIA)*, May 2014, pp. 803–808.
- [76] A. Primadianto and C. Lu, “A review on distribution system state estimation,” *IEEE Transactions on Power Systems*, vol. 32, no. 5, pp. 3875–3883, Sep. 2017.

- [77] J. Zhao, A. Gomez-Exposito, M. Netto, L. Mili, A. Abur, V. Terzija, I. Kamwa, B. C. Pal, A. K. Singh, J. Qi, Z. Huang, and A. P. S. Meliopoulos, “Power system dynamic state estimation: Motivations, definitions, methodologies and future work,” *IEEE Transactions on Power Systems*, pp. 1–1, 2019.
- [78] G. Fiore, A. Iovine, E. De Santis, and M. D. Di Benedetto, “Secure state estimation for dc microgrids control,” in *2017 13th IEEE Conference on Automation Science and Engineering (CASE)*, Aug 2017, pp. 1610–1615.
- [79] W. Doorsamy and W. A. Cronje, “State estimation on stand-alone dc microgrids through distributed intelligence,” in *2015 International Conference on Renewable Energy Research and Applications (ICRERA)*, Nov 2015, pp. 227–231.
- [80] M. Angjelichinoski, . Stefanović, P. Popovski, A. Scaglione, and F. Blaabjerg, “Topology identification for multiple-bus dc microgrids via primary control perturbations,” in *2017 IEEE Second International Conference on DC Microgrids (ICDCM)*, June 2017, pp. 202–206.
- [81] K. Gharani Khajeh, E. Bashar, A. Mahboub Rad, and G. B. Gharehpetian, “Integrated model considering effects of zero injection buses and conventional measurements on optimal pmu placement,” *IEEE Transactions on Smart Grid*, vol. 8, no. 2, pp. 1006–1013, March 2017.
- [82] DC in the home. (2013). [Online]. Available: https://standards.ieee.org/content/dam/ieee-standards/standards/web/governance/iccom/IC13-005-02_DC_in_the_Home.pdf
- [83] ETSI EN 300 132-3-1. (2011). [Online]. Available: https://www.etsi.org/deliver/etsi_en/300100_300199/3001320301/02.01.01_40/en_3001320301v020101o.pdf

- [84] EMerge Alliance Standards. (2008). [Online]. Available: <http://www.emergealliance.org/Standards/OurStandards.aspx>
- [85] IEC—Standardization management board—SG4 LVDC distribution systems up to 1500V DC. (2009). [Online]. Available: https://www.iec.ch/dyn/www/f?p=103:85:0:::FSP_ORG_ID,FSP_LANG_ID:6019,25
- [86] P. Nuutinen, T. Kaipia, P. Peltoniemi, A. Lana, A. Pinomaa, A. Mattsson, P. Silventoinen, J. Partanen, J. Lohjala, and M. Matikainen, “Research site for low-voltage direct current distribution in a utility network—structure, functions, and operation,” *IEEE Transactions on Smart Grid*, vol. 5, no. 5, pp. 2574–2582, Sep. 2014.
- [87] B. Marah, Y. R. Bhavanam, G. A. Taylor, M. K. Darwish, and A. O. Ekwue, “A practical application of low voltage dc distribution network within buildings,” in *2017 52nd International Universities Power Engineering Conference (UPEC)*, Aug 2017, pp. 1–6.
- [88] M. ApS, *The MOSEK optimization toolbox for MATLAB manual. Version 8.1.*, 2017. [Online]. Available: <http://docs.mosek.com/8.1/toolbox/index.html>
- [89] P. W. Sauer and M. A. Pai, *Power system dynamics and stability*. Prentice hall Upper Saddle River, NJ, 1998, vol. 101.
- [90] University of Washington, Dept. of Electrical Engineering. (1999) Power systems test case archive. [Online]. Available: <http://www.ee.washington.edu/research/pstca/>
- [91] O. Alsac and B. Stott, “Optimal load flow with steady-state security,” *IEEE Transactions on Power Apparatus and Systems*, vol. PAS-93, no. 3, pp. 745–751, May 1974.
- [92] Ping Yan, “Modified distributed slack bus load flow algorithm for determining economic dispatch in deregulated power systems,” in *2001 IEEE Power Engi-*

- neering Society Winter Meeting. Conference Proceedings (Cat. No.01CH37194)*, vol. 3, Jan 2001, pp. 1226–1231 vol.3.
- [93] A. Zobian and M. D. Ilic, “Unbundling of transmission and ancillary services. i. technical issues,” *IEEE Transactions on Power Systems*, vol. 12, no. 2, pp. 539–548, May 1997.
- [94] F. Mumtaz, M. H. Syed, M. A. Hosani, and H. H. Zeineldin, “A novel approach to solve power flow for islanded microgrids using modified newton raphson with droop control of dg,” *IEEE Transactions on Sustainable Energy*, vol. 7, no. 2, pp. 493–503, April 2016.
- [95] D. Choi, J. Park, and S. H. Lee, “Virtual multi-slack droop control of stand-alone microgrid with high renewable penetration based on power sensitivity analysis,” *IEEE Transactions on Power Systems*, vol. 33, no. 3, pp. 3408–3417, May 2018.
- [96] A. G. Exposito, J. L. M. Ramos, and J. R. Santos, “Slack bus selection to minimize the system power imbalance in load-flow studies,” *IEEE Transactions on Power Systems*, vol. 19, no. 2, pp. 987–995, May 2004.
- [97] X. Guoyu, F. D. Galiana, and S. Low, “Decoupled economic dispatch using the participation factors load flow,” *IEEE Power Engineering Review*, vol. PER-5, no. 6, pp. 43–44, June 1985.
- [98] J. Meisel, “System incremental cost calculations using the participation factor load-flow formulation,” *IEEE Transactions on Power Systems*, vol. 8, no. 1, pp. 357–363, Feb 1993.
- [99] G. S. Jang, D. Hur, J.-K. Park, and S. H. Lee, “A modified power flow analysis to remove a slack bus with a sense of economic load dispatch,” *Electric power systems research*, vol. 73, no. 2, pp. 137–142, 2005.

- [100] J. Zhao, Chao Zhou, and Gang Chen, “A novel bus-type extended continuation power flow considering remote voltage control,” in *2013 IEEE Power Energy Society General Meeting*, 2013, pp. 1–5.
- [101] Y. Lei, R. Wang, T. Li, Q. Tang, Y. Wang, and J. Li, “Modeling pv/pq switching in security constrained optimal power flow,” in *2019 IEEE Innovative Smart Grid Technologies-Asia (ISGT Asia)*. IEEE, 2019, pp. 84–88.
- [102] X. Wu and A. J. Conejo, “Security-constrained acopf: Incorporating worst contingencies and discrete controllers,” *IEEE Transactions on Power Systems*, pp. 1–1, 2019.
- [103] N. Cai and A. R. Khatib, “A universal power flow algorithm for industrial systems and microgrids - active power,” *IEEE Transactions on Power Systems*, pp. 1–1, 2019.
- [104] X. Wu, A. J. Conejo, and N. Amjady, “Robust security constrained acopf via conic programming: Identifying the worst contingencies,” *IEEE Transactions on Power Systems*, vol. 33, no. 6, pp. 5884–5891, 2018.
- [105] Y. Wen, C. Guo, D. S. Kirschen, and S. Dong, “Enhanced security-constrained opf with distributed battery energy storage,” *IEEE Transactions on Power Systems*, vol. 30, no. 1, pp. 98–108, 2015.
- [106] Y. Dvorkin, P. Henneaux, D. S. Kirschen, and H. Pandžić, “Optimizing primary response in preventive security-constrained optimal power flow,” *IEEE Systems Journal*, vol. 12, no. 1, pp. 414–423, 2018.
- [107] D. T. Phan and X. A. Sun, “Minimal impact corrective actions in security-constrained optimal power flow via sparsity regularization,” *IEEE Transactions on Power Systems*, vol. 30, no. 4, pp. 1947–1956, 2015.

- [108] R. Madani, M. Ashraphijuo, and J. Lavaei, “Promises of conic relaxation for contingency-constrained optimal power flow problem,” *IEEE Transactions on Power Systems*, vol. 31, no. 2, pp. 1297–1307, 2016.
- [109] Y. Kataoka, “A smooth power flow model of electric power system with generator reactive power limits taken into consideration,” in *2005 IEEE International Symposium on Circuits and Systems*. IEEE, 2005, pp. 5286–5289.
- [110] J. Zhao, H.-D. Chiang, P. Ju, and H. Li, “On pv-pq bus type switching logic in power flow computation,” in *Power Systems Computation Conference (PSCC), Glasgow, Scotland, 2008*.
- [111] A. Agarwal, A. Pandey, M. Jereminov, and L. Pileggi, “Continuously differentiable analytical models for implicit control within power flow,” 2018.
- [112] R. D. Zimmerman, C. E. Murillo-Sanchez, and R. J. Thomas, “Matpower: Steady-state operations, planning, and analysis tools for power systems research and education,” *IEEE Transactions on Power Systems*, vol. 26, no. 1, pp. 12–19, Feb 2011.

BIOGRAPHICAL STATEMENT

Tuncay Altun earned the B.Sc. and M.Sc. degrees in Electrical Engineering from the Yıldız Technical University, Istanbul, Turkey, in 2011 and 2014, respectively. He is receiving his Ph.D. degree from the University of Texas at Arlington, Arlington, TX, USA in July 2020. His research interests include control and optimization for applications of power systems, microgrids, HVDC transmission, and renewable/sustainable energy systems.